Analytical Modelling and Design Optimisation of the Eddy Current Slip Coupler

by

Abram Stephanus Erasmus

Thesis presented in partial fulfilment of the requirements for the degree of Project Report presented in fulfilment of the requirements for the degree of a Masters in Engineering at the University of Stellenbosch in the Faculty of Engineering at Stellenbosch University

Department of Electric and Electronic Engineering,
University of Stellenbosch,
Private Bag X1, Matieland 7602, South Africa.

Supervisor: Prof. M.J. Kamper

March 2017

Declaration

By submitting this thesis electronically, I declare that the entirety of the work contained therein is my own, original work, that I am the sole author thereof (save to the extent explicitly otherwise stated), that reproduction and publication thereof by Stellenbosch University will not infringe any third party rights and that I have not previously in its entirety or in part submitted it for obtaining any qualification.

Date: ..... March 2017.....

Abstract

Analytical Modelling and Design Optimisation of the Eddy Current Slip Coupler

A.S. Erasmus

Department of Electric and Electronic Engineering,
University of Stellenbosch,
Private Bag X1, Matieland 7602, South Africa.

Thesis: BEng (E&E)

November 2016

In this study a novel analytical torque calculation method is proposed and used in conjunction with existing design optimisation algorithms to design and manufacture a double sided radial axis eddy current coupler. The eddy current coupler is a rotating damper that is placed between two mechanical systems, it filters out high frequency torque and protects system components from over-torque.

The analytical torque calculation method called the Computationally Efficient Finite Element Analysis (CE-FEA) method is a hybrid method that consists of a static FEA and analytical calculations which sets it apart form Maxwell's equations, magnetic equivalent circuits and transient FEA. The CE-FEA has been extensively tested in this study and has been found to be accurate within 5 % of the 3D FEA. The benefit of using the CE-FEA besides its accuracy, is its speed. It is able to provide a result in a fraction of the time a 3D FEA takes.

The CE-FEA is then used in conjunction with multi objective design optimisation algorithms to find an optimal coupler design. Two types of optimisation algorithms are evaluated and compared, a gradient (MMFD) and a population (NSAGA-II) based method. From the results of the population based method a pareto front is produced which is then investigated by adding a variable based colour gradient map. This provides the designer better insight into the effects different variables have on the size, cost, weight and performance of the machine.

Further, the optimal eddy current coupler design is chosen and manufactured and tested in a laboratory environment in order to verify the entire design process. The built coupler measurements didn't initially match that of the simulations. This was found to be due to a low grade of aluminium that was used during the manufacturing of the conductor. The resistivity of the conductor was adjusted in the simulations to match that of a lower grade. With this adjustment the measured and simulated results matched, verifying the design process.

Finally, two eddy current coupler case studies are conducted. The first is a validation of the design process but for a single sided eddy current yaw damper for use in wind turbine drivetrains. The second is a brief comparison between the eddy current coupler and an existing Slip Permanent Magnet Coupler (SPMC).

Opsomming

Analitiese Modellering en Ontwerp Optimering van die Warrelstroom koppeling

("Analytical Modelling and Design Optimisation of the Eddy Current Slip Coupler")

A.S. Erasmus

Departement Elektries Elektroniese Ingenieurswese,
Universiteit van Stellenbosch,
Privaatsak X1, Matieland 7602, Suid Afrika.

Tesis: BIng (E&E)

November 2016

Hierdie studie stel voor 'n nuwe analitiese draaimoment berekening metode wat gebruik word saam met huidige ontwerp optimering algoritmes om 'n tweesydige radiale as werwelstroom koppeling te ontwerp en te vervaardig. Die werwelstroom koppeling is 'n roterende demper wat geplaas word tussen twee meganiese stelsels en filtreer hoë frekwensie draaimoment en dien as stelsel beveiliging teen hoë draaimoment impulse.

Die analitiese draaimoment berekening methode genoem die Berekening Effektiewe Eindige Element Analise (BE-EEA) is 'n hibriede metode is. Dit bestaan uit 'n statiese eindige element analise en 'n analitiese berekening wat dit afsonderlik plaas van Maxwell se vergelyking, magnetiese ekwivalente stroombaan analise en oorgangs eindige element analise. Die BE-EEA is omvattend getoets in hierdie studie en daar is gevind dat dit akkuraat is binne 5 % van 3D EEA. Die voordeel van die BE-FEA buiten die akuratheid, is die spoed. Dit is in staat om 'n resultaat te lewer 'n fraksie van die tyd wat 'n 3D EEA sou neem.

Die BE-EEA word verder gebruik in 'n veelvuldige doelwit ontwerp optimering algoritme om 'n optimale koppeling ontwerp te vind. Twee tipe optimering algoritmes word geëvalueer en vergelyk, 'n gradiënt (MMFD) en 'n populasie (NSGA-II) gebaseerde methode. Vanaf die resultate van die populasie algoritme word 'n 'pareto' front gelewer. Dit word dan verder ontleed deur 'n

kleur gradiënt by te voeg wat afhanklik is van die intree veranderlikes. Hierdie verskaf aan die ontwerper meer insig hoe die intree veranderlikes 'n invloed het op die massa, koste, grote en prestasie van die uittree koppeling se ontwerp.

Verder word die optimale werwelstroom koppeling ontwerp gekies, vervaardig en getoets in 'n laboratorium om die ontwerp proses te bevestig. Die koppeling wat gebou is het aanvanklik nie met die simulasie resultate ooreengestem nie. Dit is gevind dat dit as gevolg van 'n lae graad aluminium wat gebruik is vir vervaardiging van die geleier. Die resistiviteit van die geleier is toe in die simulasies aangepas om ooreen te stem met die geleier wat vervaardig is. Met hierdie aanpassing stem die resultate wat gemeet is ooreen met die simulasies, wat dus die ontwerp proses bevestig.

Laaste is twee werwelstroom koppeling gevalle studies gedoen. Die eerste is weer 'n bevestiging van die ontwerp proses maar vir 'n enkel sydige werwelstroom gier demper wat gebruik is in wind turbine dryf aste. Die tweede gevalle studie is 'n vergelyking tussen die werwelstroom koppeling en 'n reeds bestaande slip permanente magneet koppeling.

Author's note

The larger part of the content in this thesis contains the work of two articles presented at the IEEE Electrical Convergence Conference and Exposition (ECCE) in 2015 in Montreal, Canada and in 2016 in Milwaukee, USA. One article is submitted for journal review for the IEEE Industrial Applications Society (IAS) and the other will be submitted after the submission of this thesis.

A. S. Erasmus and M. J. Kamper, "Analysis for design optimisation of double PM-rotor radial flux eddy current couplers," 2015 IEEE Energy Conversion Congress and Exposition (ECCE), Montreal, QC, 2015.

A. S. Erasmus and M. J. Kamper, "Multi-objective Design Optimisation and Pareto Front Visualisation of Radial-flux Eddy Current Coupling for a Wind Generator Drivetrain," 2016 IEEE Energy Conversion Congress and Exposition (ECCE), Milwaukee, WI, 2016.

I would like to specially thank Professor Maarten Kamper for his profound trust, support and guidance the past three years. It is rare that you meet someone that is willing to give you an opportunity to succeed. The lessons I have learnt from him reaches beyond engineering, from constructing logical flow of concepts to treating other people with kindness and respect. He is still one of the few true academics around, someone who is more of a mentor than a supervisor.

Stephan Erasmus

Acknowledgements

I would like to express my sincere gratitude to the following people and organisations:

- Professor Kamper for his guidance in carving out a clear and logical route through the mountain of research and publications.

- Kenan Cloete for his help with CAD drawings and test bench set-up.

- Andre Swart for always taking the time to help me with a test set-up and giving me advice on machine construction.

- Murray Jumat for his kindness and willingness to provide me with all the testing equipment I need.

- Petro Petzer for his passion and energy to help with the technical and practical side of things even though there is a back log of pending projects and tasks.

- Petrus Pieterse, Howard and Denise for the help and support.

Contents

List of Figures

List of Tables

Nomenclature

Abbreviations

Al	Aluminium
CNC	Computer Numeric Control
Cu	Copper
EMF	Electromotive Force
FE	Finite Element
FEA	Finite Element Analysis
IG	Induction Generator
MEC	Magnetic Equivalent Circuit
MMFD	Modified Method of Feasible Direction
NdFeB	Neodynium Ferite Boron
NSGA-II	Non-dominated Sorting Genetic Algorithm
PM	Permanent magnet
PMG	Permanent magnet generator
SEMFEM	Stellenbosch EmLab Finite Element Method
SG	Synchronous generator
SPMC	Slip Permanent Magnet Coupler
SS-PMG	Slip synchronous permanent magnet generator
THD	Total Harmonic Distortion

Variables

α	Overhang dimension coefficient	[ ]
α_t	Temperature coefficient of resistance for a conductor	[ ]
β	Dimension coefficient	[ ]
B	Radial flux density	[T]
B_{ni}	Amplitude of the n^{th} Fourier harmonic radial flux density	[ ]
δ	Skin depth	[mm]
d_c	Centre diameter of the cylinder conductor	[mm]
ϵ	Electromotive force	[E]

F_1	Mass Objective	[kg]
F_2	Cost Objective	[perunit]
f_{slip}	Slip frequency	[Hz]
h_c	Conductor thickness	[mm]
h_{ci}	Radial thickness of the conductor of single layer	[mm]
h_m	Magnet thickness	[mm]
h_{y1}	Yoke thickness	[mm]
i	Number of radial layers	[ ]
K_c	Conductor cost factor	[ ]
K_e	Russell's end-effect factor	[ ]
λ	Overhang coefficient	[ ]
l_{oh}	Axial overhang length	[mm]
l_{pm}	Active axial length	[mm]
N	Number of turns	[ ]
n_s	Rated rotational speed	[rpm]
m_{cond}	Conductor mass	[kg]
m_{pm}	Magnet mass	[kg]
m_{Fe}	Steel mass	[kg]
μ	Permeability of conductor material	[H/m]
ω_e	Electrical angular velocity	[rad/s]
Φ_B	Magnetic flux in a single loop	[H]
p	Number of poles	[ ]
r_c	Conductor radius	[mm]
r_{ci}	Average conductor layer radius	[mm]
ρ	Conductor resistivity	[$\Omega \cdot$ m]
ρ_{ref}	Conductor resistivity at room temperature	[$\Omega \cdot$ m]
ρ	Resistivity of the conductor element	[$\Omega \cdot$ m]
s	Slip percentage	[%]
T	Temperature	[°C]
T_{ref}	Reference temperature	[°C]
$\tau_{2D(FEt)}$	Torque from 2D transient FE solution	[Nm]
$\tau_{3D(FEt)}$	Torque from 3D transient FE solution	[Nm]
τ_r	Radial Torque	[Nm]
θ	Electrical position	[rad]
θ_p	Magnet pitch	[rad]

Chapter 1

Introduction

With climate change becoming a pressing issue global economies push for cleaner, more efficient and sustainable methods of power generation. On one side researchers are find alternative solutions for a sustainable future by changing the way power is generated. On another, finding ways to improve and minimise the impact that existing power systems, usage and practices have on the planet.

Electrical machines have always been a fundamental part of how electricity is generated, large scale coal stations have been utilizing rotating machines for decades to convert mechanical energy into electrical energy. With recent developments concerning climate change, governmental and intergovernmental policies are pushing for sustainable solutions with regards to energy supply. Wind farms and hydro dams have shown to be effective alternatives to coal and oil power plants being implemented worldwide at a fast pace. Similar to coal power stations, wind and hydro also utilize rotating electrical machines to generate electricity.

When generating large amounts of electricity, power quality and mechanical safety become important factors to consider when implementing new systems. These systems, and especially the generators, operate under high torque loads and the require some sort of mechanical safety or braking mechanism. Torque slip couplers are popular additions to a system that serve as a protection against torque overloads and spikes, ensuring longer operational times of the generator. In addition, it also improves the power quality when used in direct drive wind energy turbines.

1.1 Overview of permanent magnet torque couplers

A Permanent Magnet (PM) coupler is a machine that is usually placed on the shaft between two rotating mechanical systems [3]. These couplers operate using strong magnetic fields, and are governed by the laws of electromagnetism and electromagnetic induction. Slip couplers were originally made from bulky and heavy electromagnets which made it difficult to implement without using slip rings and power supplies. The first PM materials like Ferrite magnets weren't strong enough to be used in coupler, but with recent developments in stronger and cheaper rare-earth magnet materials like NdFeB, new applications and topologies have emerged.

The use of permanent magnets in slip couplers have the advantage of having smaller radial and axial dimensions resulting in a coupler with lower mass. They also contribute to bigger air gaps for easier manufacturing and a higher torque per mass ratio. Currently some of the most popular and most recent types of slip couplers include: Synchronous, Multiphase and Eddy Current [4] [5] [6].

1.1.1 Synchronous torque couplers

Synchronous type magnetic torque couplers as shown in Fig. 1.1 consist of two rotors, each fitted with permanent magnets rotating at the same speed. The torque transferred between the rotor is dependant on the relative displacement angle between the two rotors. The magnetisation of the magnets should be constant over time and rotational space. This is a difficult requirement to meet because it requires very coercive magnets [3]. A significant drawback of using synchronous magnetic couplers is the attractive forces between the two rotors, requiring thick iron yokes for structural support [7] [8].

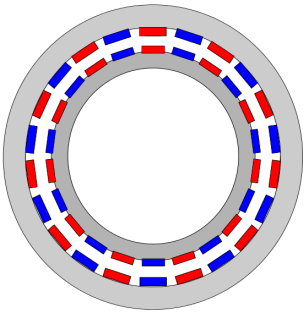

Figure 1.1. Cross section of radial axis PM synchronous torque coupler.

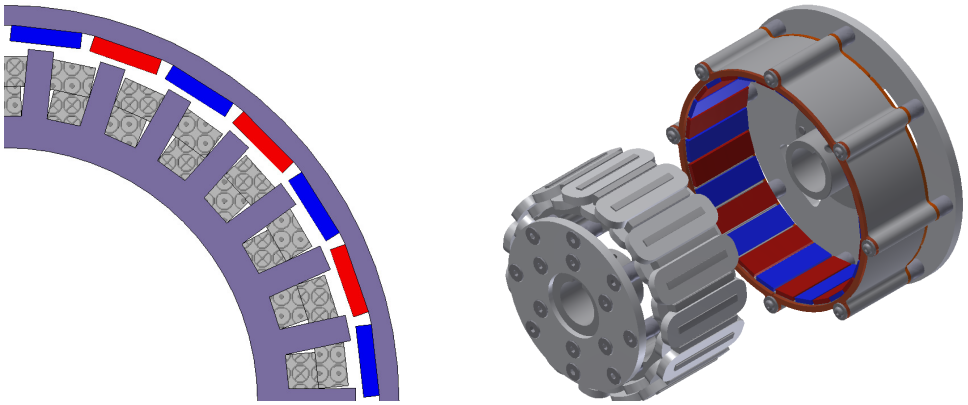

Cross section model. 3D model.

Figure 1.2. Radial axis SPMC torque coupler.

1.1.2 Multiphase torque couplers

The multiphase slip permanent magnet coupler is a recent development in slip coupler technology, introduced in [4]. This Slip Permanent Magnet Coupler (SPMC) shown in Fig. 1.2 consists of two rotors, but unlike the synchronous coupler, the multiphase coupler transfers torque when there is a difference in speed between the two rotors.

The coupler is similar to an induction machine with permanent magnets on the outer rotor that induces a current on the secondary rotor. The secondary rotor consists of 30 individually shorted coils and generates torque when current is induced. Current is induced when the magnets on the primary rotor rotates at a different speed, the slip speed, than the secondary rotor. The amount of torque that is transferred is directly dependent on the slip speed between the two rotors.

This coupler uses significantly less magnet material that the synchronous type, and has proved to be an effective torque coupler [9]. The drawback of this type of coupler is the high amount radial attraction forces between the magnets and the yokes which makes assembly difficult.

1.1.3 Eddy current torque couplers

Eddy current torque couplers have existed since the 1960's and have been popular in industrial settings as brakes and damping mechanisms [10], [11]. Much like the first synchronous couplers, these couplers were originally fitted with field windings that produced the magnetic field.

The field windings are now replaced with permanent magnets which had a big effect on the renewed research interest of these couplers. Like the other

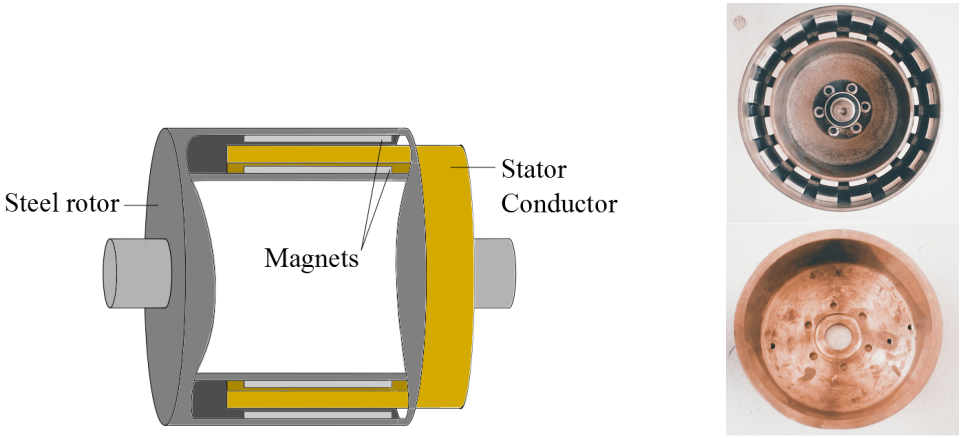

Cross section model. Prototype coupler.

Figure 1.3. Radial axis PM eddy current torque coupler.

couplers mentioned, the eddy current coupler has two rotors as shown in Fig 1.3. The primary rotor consist of permanent magnets that produce the magnetic field, very similar to that of the multiphase coupler. The secondary rotor is simply a solid conductor and generates torque when currents are induced. Currents are induced in a similar way as the multiphase coupler when there is a slip difference between the primary and secondary rotor.

The eddy current coupler is discussed in further detail in Chapter 2

1.2 Slip couplers in industrial applications

As previously stated, torque couplers are used to protect a generator from torque overloads. It is placed between two mechanical systems as shown in Fig. 1.4, and transfers torque without any mechanical contact. The torque coupler increases the lifetime of generators and motors placed in the system.

There exists a possibility that eddy current and multiphase couplers can increase the efficiency of a mechanical system with a high frequency variable torque load. This hasn't been verified by any research publications.

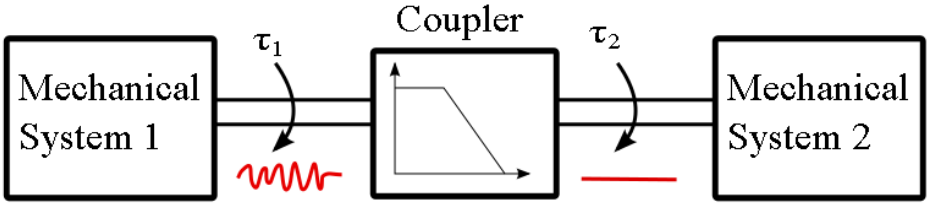

Figure 1.4. Torque coupler in mechanical system.

1.3 The use of slip couplers in a wind turbine drivetrain

Slip couplers also act as mechanical dampers, as found by Potgieter in [12], and shown in Fig. 1.5. The transient damping properties of the slip (IG) section of the Slip Synchronous Permanent Magnet Generator (SS-PMG) allows the direct grid connection at the SG section of the generator, shown in Fig 1.5 below. The advantage of the slip rotor is the reduction of power electronic converters required for grid connection. The generator thus has longer operational times and requires less maintenance.

In recent research developments, the slip section of the SS-PMG is separated from the synchronous generator (SG), in order to allow the addition of a gearbox into the wind turbine drive train as shown in Fig 1.6. This allows higher SG operational speeds, resulting in smaller and lighter generators.

1.4 Permanent magnet torque coupler design

The design procedure of PM torque couplers include the use of Finite Element Analysis (FEA) software to model and analyse the electromagnetic properties of the machine. In order to obtain an optimal model, the FEA is run multiple times in a design optimization environment which makes use of machine learning methods. The results from the optimization show how the machine variables interact and provides an optimal solution that can be utilized in the final design of the coupler to be manufactured.

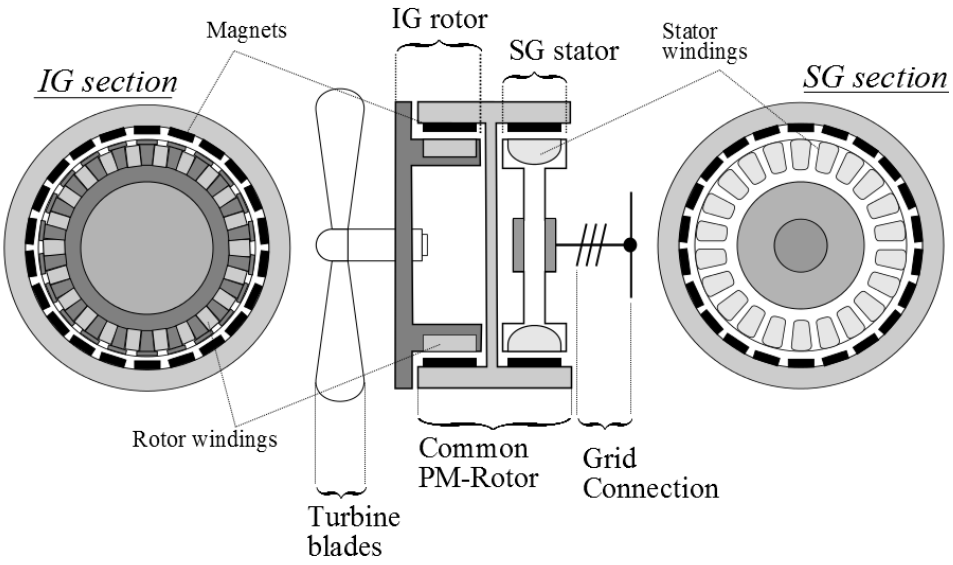

Figure 1.5. Slip synchronous permanent magnet generator.

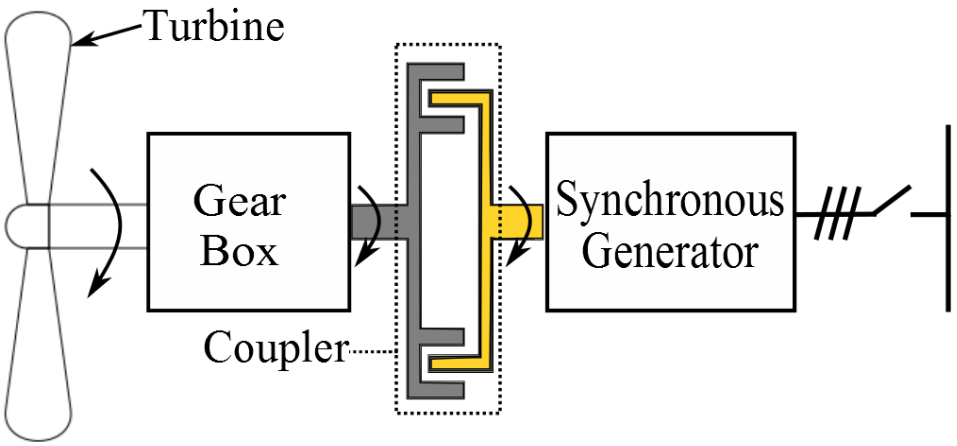

Figure 1.6. Coupler connected in a wind turbine drive train.

1.5 Problem statement

Modelling of eddy current induction isn't simple, and not all FEA simulations can evaluate it accurately and can take a long time to obtain a result. However, using 3D FEA is an accurate way of obtaining a result but is computationally and time intensive. Design optimization techniques have been well developed and prove to work on machine design applications, but using 3D FEA in design optimisation algorithms makes it even more demanding in terms of time and computing power.

1.6 Research objectives

In this study the design, manufacturing and analysis of radial axis PM eddy current coupler is investigated and is limited to the following research objectives:

- To develop a hybrid analytical/mathematical model for the eddy current coupler that can be solved to obtain a torque result. This model is to be scripted in a programming environment to obtain the equivalent of 3D transient FEA solution, but much faster than commercial FEA packages.
- To evaluate the accuracy of the analytical/mathematical model under various variable extremities.
- The evaluation of gradient and population based design optimization techniques with the above model used as a primary study.
- To obtain an optimal solution using design optimization strategies and tools.
- The manufacturing of a working eddy current coupler prototype based on the design parameters given by the design optimisation.

- Evaluating a single sided coupler topology using the same method as double sided topology.
- Comparison of the eddy current coupler with other coupler topologies like the multiphase torque coupler.

1.7 Research scope

The following are included in the scope of this study:

- Development of hybrid analytical model of the eddy current coupler.
- Use the analytical model to calculate the torque induced in the coupler.
- Implementation of Russell's end effect factor to calculate the 3D torque.
- Evaluation of 2D and 3D analytical method accuracy for various coupler dimensions using Python, SEMFEM and JMAG.
- Investigation of two multi-objective design optimization techniques.
- Integration of SEMFEM hybrid analytical model into design optimization software.
- Finding the optimal design of the coupler using design optimization techniques.
- Manufacturing and assembly of the optimal design prototype.
- Testing optimal prototype on test bench.
- Evaluating performance of the Eddy current coupler.
- Evaluating the analytical method and design optimisation on a single sided eddy current coupler topology to be used as a yaw damper in a wind turbine system.
- Comparison of the eddy current coupler to an existing multiphase coupler that operate at the same rated conditions.

1.8 Thesis layout

The thesis covers the following topics in each chapter:

- Chapter 2 covers the fundamental operation of a radial axis permanent magnet eddy current coupler.

- Chapter 3 covers the hybrid analytical modelling and torque calculation methodology of the eddy current coupler.
- Chapter 4 focuses on the coupler design optimization and methodology.
- Chapter 5 covers the assembly and construction of the coupler.
- Chapter 6 focuses on the practical verification and testing of the coupler, and also on the efficiency of the coupler.
- Chapter 7 consists of two case studies. The first is an eddy current yaw damper and the second is the comparison of the eddy current and multiphase coupler.
- Chapter 8 sums up the project and provides recommendations for future work.
- Appendix A has figures of CAD models of all the different components of the coupler.

Chapter 2

Eddy current coupler concept

This chapter is a study of the literature specifically on the eddy current coupler. The first section elaborates on the fundamental working of the eddy current coupler, then a research summary of the three core aspects of this project are discussed to specify the scientific research direction of the project.

2.1 Overview

The eddy current coupler works on the eddy current principle, where circular electrical currents are induced within a conductor by a nearby changing magnetic field. The eddy currents are produced due to Faraday's law of induction and flow in a closed circular loop perpendicular to the magnetic field inside the conductor. With Faraday's law of induction together with Lenz's law as:

$$\epsilon = -N\frac{d\Phi_B}{dt} \tag{2.1.1}$$

where N is the number of turns of wire (or loops), and Φ_B the magnetic flux in a single loop. From this it is clear that the magnitude of the electromotive force (EMF), ϵ, is proportional to the rate of change of the flux and the strength of the magnetic field. The negative sign in the equation refers to the Lenz's law that states:

If an induced current flows, its direction is always such that it opposes the change which produced it.

Thus, the eddy currents induce an opposing magnetic field in the conductor that opposes the magnetic field created by the source as seen in Fig 2.1. In electrical motors and generators, eddy currents aren't desirable and machine designers aim to reduce these currents as much as possible. This is not the case for the eddy current coupler.

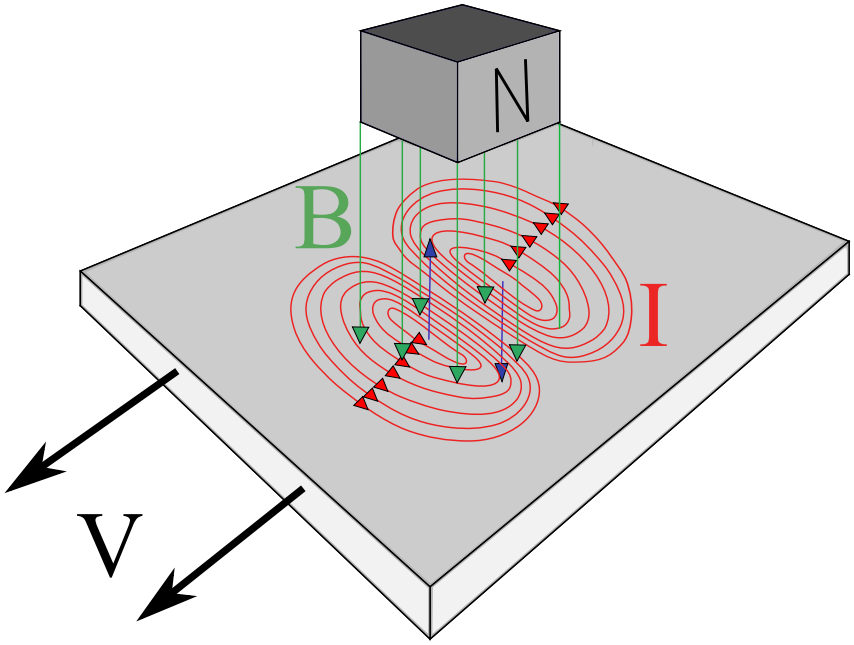

Figure 2.1. Eddy current effect as explained in terms of Lenz and Faraday's laws.

With an eddy current coupler the aim is to create as much eddy currents as possible. A force is generated between the conductor and the source from (2.1), allowing the conductor to follow the movement of the source. This force results in the torque transfer between two rotating mechanical systems without them being mechanically connected.

For the coupler to transfer torque there needs to be a speed difference between the two mechanical systems, the slip speed. This speed difference allows torque transfer and also the coupler's capability to function as a mechanical low pass filter as shown in Fig 2.2, filtering out torque spikes and high frequency torque ripple. The properties and applications of the low pass filter functionality has limited publications. A recent study with regard to a slip coupler low pass filter capability shows that the slip coupler can be modelled as a gain based on its torque-slip curve. Furthermore, the study revealed that the slip coupler can filter out frequencies higher than 6 Hz [13].

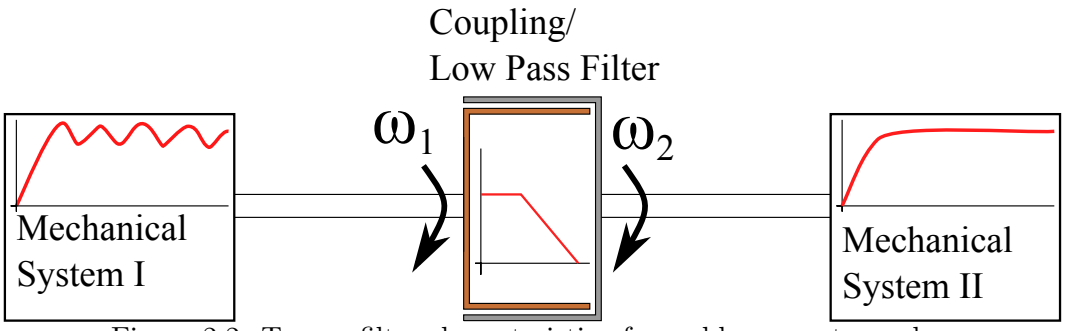

Figure 2.2. Torque filter characteristic of an eddy current coupler.

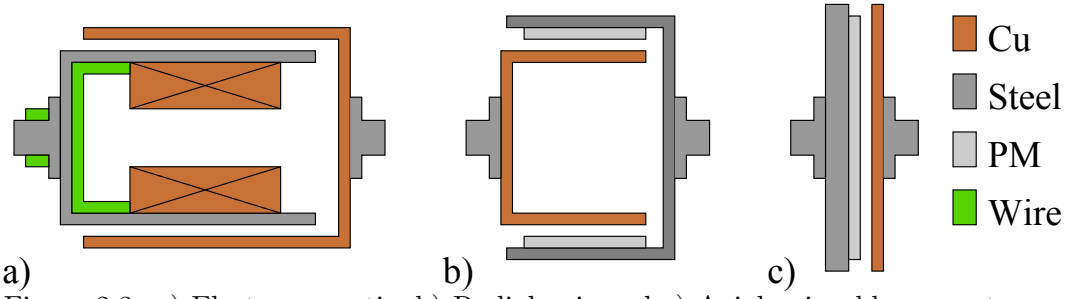

Figure 2.3. a) Electromagnetic, b) Radial axis and c) Axial axis eddy current couplers.

2.1.1 Developments in eddy current coupler technology and topologies

Early versions of the eddy current coupler only consisted of electromagnets to provide a magnetic field as shown in Fig. 2.3 a) [10]. These couplers were large in size to be effective and were used primarily as brakes in high speed railway systems.

With the increased availability of stronger permanent magnets, the mass of these machines have been considerably reduced and two main coupler topologies exist, namely radial and axial axis shown in Fig. 2.3. Axial axis couplers have proven to be an effective method of torque transfer between two shafts and extensive research has been done on this topology [7] [14] [15] [16] [17]. This topology is also popular in industry and is sold as a 'Fixed speed coupler'. The radial axis topology has also been a popular topic among researchers since the popularity of permanent magnets in 2010 and various publications explore the analysis, modelling and design of these couplers [2] [18]. Within these two topologies, four magnet-conductor configuration types exits and is shown in Fig. 2.4.

The conductor is typically made from a material with low electrical resistivity like copper or aluminium. When it comes to permanent magnets, research

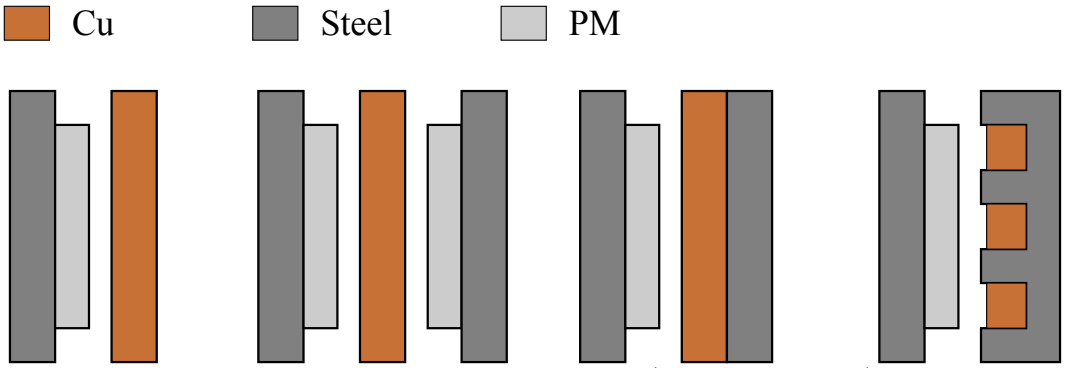

Figure 2.4. Eddy current coupler configurations. a) Single sided. b) Double sided. c) Single sided with conductor yoke. d) Toothed slip coupler.

papers indicate that Neodymium Boron Iron (NdFeB) is the most popular choice due to its high magnetic flux density.

2.1.2 Eddy current coupler uses

As previously mentioned, the coupler functions as a filter for torque ripple and spikes. This is especially useful in industrial applications where loads aren't constant (water, rocks etc.) and need to be transported. Water pumps, conveyor belts and cooling systems all operate under this high frequency torque ripple. The motors and gearboxes that are used in these systems thus have shorter life spans and require regular maintenance and bearing replacement.Due to the eddy current coupler's ability to filter out high torque frequencies, making it an ideal machine to protect motors and gearboxes. The following case study of a coupler used in industry was published on-line:

> *"The City of Eugene, Oregon wastewater treatment facility was experiencing premature wear in the bearings of the gearbox connecting their motor to their double flight, Archimedean screw pump. Because they were using a belt drive to transfer torque between a 200 hp motor and the gearbox turning a 90 inch (2.29 m) diameter, 63 (19.2 m) long screw, they were experiencing premature wear in the systems bearings. The lateral forces of the belt drive on the gearbox shaft created an unbalanced load leading to the need for increased maintenance activities."* [19]

After the coupler was installed in the system, there was less wear on the bearings of the system, little vibration between system components, and much less maintenance was required after installation. The other benefit that the coupler had was a 35 % increase in energy savings, with a payback period shorter than 4 months [19] .

As mentioned in the introduction, the other application for these couplers are in wind energy drivetrains [4] [20]. Because the wind changes rapidly, the generator experiences a lot of torque and speed fluctuations. The eddy current coupler can be inserted on the drivetrain to filter out the torque fluctuations caused by the wind, protecting the generator and/or gearbox depending on the topology. Similar to the motors in industrial applications. This improves the power quality and total harmonic distortion which is important for grid compliance of wind turbines.

The physical size of the coupler depends on where the coupler is placed on a drivetrain. With reference to Fig. 1.6, if the coupler is placed on the low speed side of the gearbox, the gearbox and motor is protected but the coupler will be larger. If the coupler is placed at the high speed side of the gearbox, the

coupler will be small but the gearbox won't be protected.

2.2 Eddy current coupler analytical analysis methods

When evaluating the accumulated research publications on eddy current couplers, the analytical analysis is by far the most difficult and the most focussed on. Many researchers attempt to obtain an accurate mathematical or 'analytical' model for the flow of the eddy currents in the conductor so that the torque can be determined. As mentioned earlier in the chapter, the eddy currents are dependent on the movement of a magnetic flux source. Thus, a lot of research articles makes use of Maxwell's laws of electromagnetic induction. Another way to attempt and solve the problem is by using a magnetic equivalent circuit (MEC) model. Both these methods are popular in antenna design and electromagnetic engineering. The reason for the popularity of using Maxwell and MEC methods is the time advantage over numerical solvers. Analytical models can be solved in seconds whereas a 3D FEA can take a significantly longer time.

Another reason for the amount of analytical methods published, is because the methods aren't ever 100 % accurate and researchers try to find different methods to solve the problem. Researchers report on 2 - 10 % error in most cases. No method is perfect, but it is important to consider and compare all methods of analytical calculation.

2.2.1 Maxwell equation method

Maxwell's equations are some of the fundamental tools to solve magnetic field problems. Maxwell was able to define mathematically the field effects that Faraday only could observe. With regard to the magnetic field in eddy current couplers, Lesobre [21], Lubin [7] and Choi [22] used Maxwell's equations to solve dynamic models of an eddy current brake and coupler. Using Maxwell's diffusion equation, Dai successfully modelled an adjustable speed coupler [23] as well as an axial flux PM coupler with a slotted conductor topology [15]. In his findings he states that the analytical calculations neglected saturation effects as well as back iron conductivity and eddy currents.

The neglect of saturation effects can be corrected by using a numerical (FEA) solution, but that then defeats the point of a fast analytical solution. Not only does Maxwell's equations neglect saturation effects, but it doesn't take into account homogeneous permeability regions.

2.2.2 Magnetic equivalent circuit method

The magnetic equivalent circuit method's name speaks for itself, it models a part of an eddy current coupler as an electrical circuit. This circuit has resistance, current and voltage and can be solved using Faraday and Ampere laws. In [1] Mohammadi explains the process as:

> *"The block diagram depicted in* [Fig. 2.5] *illustrates how the proposed model is established. The magnetic flux density due to PMs is first determined via the implemented MEC. The induced current in the* [Conductor] *due to the relative speed is then calculated with Faradays law. Afterward, the reaction field developed by the induced currents on the original field is taken into account through Amperes law. Finally, the developed torque is obtained by Lorentz law."*

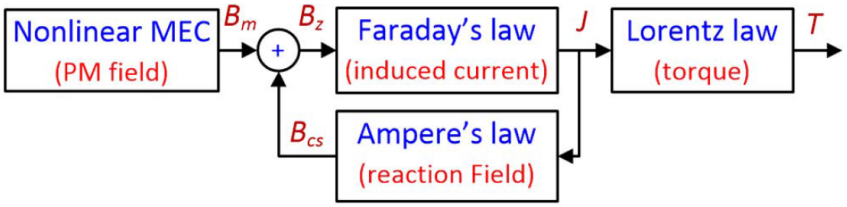

Figure 2.5. Flow diagram of MEC process as published in [1].

Another example of a MEC being used in a radial axis eddy current coupler can be found in [18] and [24]. Although MEC is simple and fast to solve, it is usually not very accurate.

2.2.3 Other analytical methods

There are a few methods that use electromagnetic field theory formulas, but aren't directly Maxwell's formulas. These include the variable separation method which is a differential equation method used in [25] and [26], and an unnamed analytical method used in [27] which takes saturation effects into account.

2.3 Eddy current coupler design optimization

Design optimization is a large field of research and is applied in many engineering fields where optimal design parameters needs to be found. In this study, time only allows for an overview of the design optimization research that exists.

In terms of eddy current coupler design optimization, a number of articles have been published. In [18], [28], [29] and [30] the problem is said to require

a multi-objective based optimization solution, and successfully utilises a genetic algorithm to find the optimal parameters. The use of a computationally efficient FEA in a design optimisation environment has been done by [31], but was done for PM AC machines. This implementation hasn't been done for radial axis eddy current couplers.

Taking the broader field of design optimization of electrical machines into account, research covers various optimization methods and algorithms.'*A Review of Recent Developments in Electrical Machine Design Optimization Methods with a Permanent Magnet Synchronous Motor Benchmark*' [32] is perhaps the largest comprehensive literature study done on electrical machine design optimization. What it didn't cover and what many researchers ignore, is gradient based design optimization [33]. This is discussed in more detail in Chapter 4.

2.4 Eddy current coupler dynamic response characteristics

This is the point where the research is spread very thin and only two articles have shown the dynamic characteristics of an eddy current coupler. Lubin [16] shows the dynamic response of the coupler at various air gap sizes. Tonoli [34] is (to the author's knowledge) the only one that described the low pass filter characteristics of an eddy current coupler in detail.

Summary

This chapter gives an overview of the fundamental working of an eddy current coupling and the various analysis methods used to solve the induced current. An overview is given of analytical methods like Maxwell's equations and the MEC and the research that has been done on their use in eddy current couplers. Research on design optimisation with regards to machine design is discussed.

Chapter 3

Analytical modelling and torque calculation methodology

> *"The word model is used as a noun, adjective and verb, and in each instance it has a slightly different connotation. As a noun "model" is a representation in the sense in which an architect constructs a small-scale model of a building or a physicist a large-scale model of an atom. As a an adjective "model" implies a degree of perfection or idealisation, as in reference to a model home, a model student or a model husband. As a verb "to model" means to demonstrate, to reveal, to show what a thing is like."* - Russell L. Ackhoff (1962) Scientific method: optimising applied research decisions p. 108.

Research on deriving analytical expressions of a permanent magnet (PM) axial-axis eddy current couplers have been published. This includes amongst others those of [7] and [35], where functional analytical expressions for an axial axis eddy current coupler are derived.

The focus of this chapter is on modelling and obtaining an *alternative* semi-analytical method of calculating the torque of a radial axis eddy current coupler. The proposed computationally efficient analytical method includes a 2D finite element analysis (FEA) static solution, which distinguishes the method fundamentally from than that of MEC and Maxwell equation methods. It takes into account the saturation of the rotor yokes, the effect of flux density harmonics and the skin effect.

Studies conducted on finding an analytical expression for an eddy current coupler are mainly split between using Maxwell's electromagnetic formulas or an MEC to find the magnetic flux density in the air gap. Maxwell's equations are more widely used and implemented in: [15], [23], [27], [21], [25] and [16] on both radial and axial axis couplers. The MEC technique is used in eddy

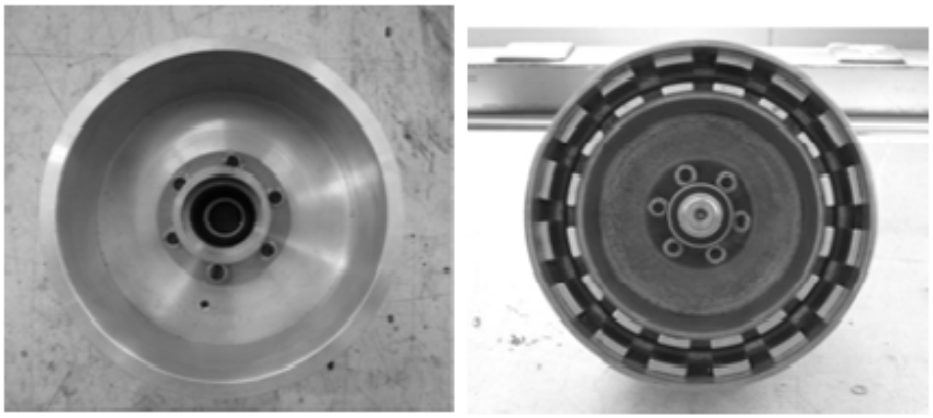

Figure 3.1. Built prototype by [2], forming the basis of analytical model.

current coupler analysis mostly by [1], [35], and [36].

The use of 3D transient FEA is shown to be necessary for an accurate calculation of the torque of the coupler as [18]. Unfortunately 3D transient FEA is computationally expensive. A method whereby a 3D torque solution is obtained from a 2D calculated torque was developed by Russell [37]. The 2D torque result is multiplied by a correction factor proportional to the size and overhang of the model, to obtain a 3D torque result. Using computational 3D finite element (FE) analysis, Russell's approach has been validated as an effective method in [38], [39], [40] and [41].

The study of [2] on the design of double PM-rotor radial flux eddy current couplers has shown to deliver well designed prototypes, however the methodology used for the coupler design is found to be too complex and time consuming for further optimisation purposes.

A computationally efficient FEA (CE-FEA) method is investigated for the accurate calculation of the torque of PM-rotor eddy current couplers at low slip values:
- First a 2D analytical expression for the torque of the coupler is derived and evaluated against 2D transient FEA.
- The 2D result is then used together with Russell's coefficient to calculate the

Table 3.1. Cross section dimensions of prototype coupler.

Poles (p)	16	l_{pm}	35 mm
Base Speed	375 r/min	l_{oh}	8.5 mm
θ_m	13.34^o	α	0.4857
θ_p	22.5^o	β	0.23
l_g	10 mm	h_m	5 mm
h_y	4 mm	h_c	8 mm
h_m	5 mm	r_c	76 mm

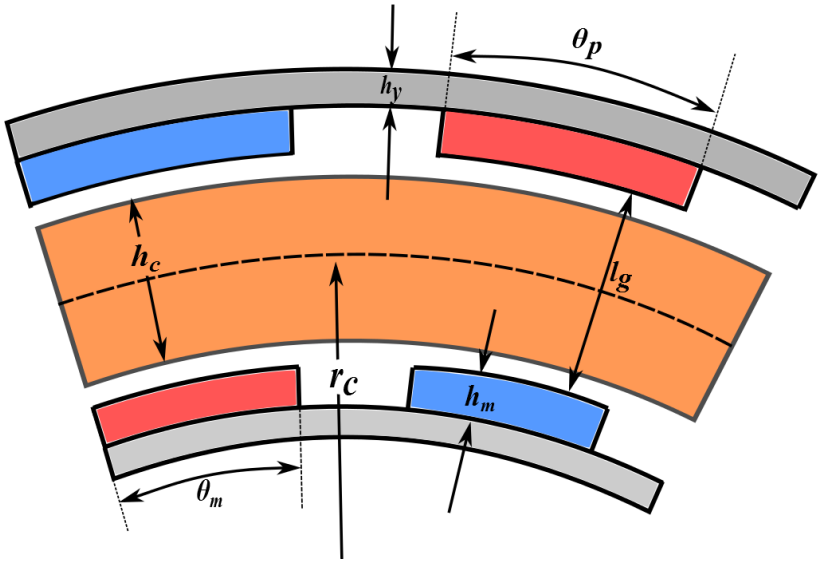

Figure 3.2. Radial cross section of the radial axis eddy current coupler.

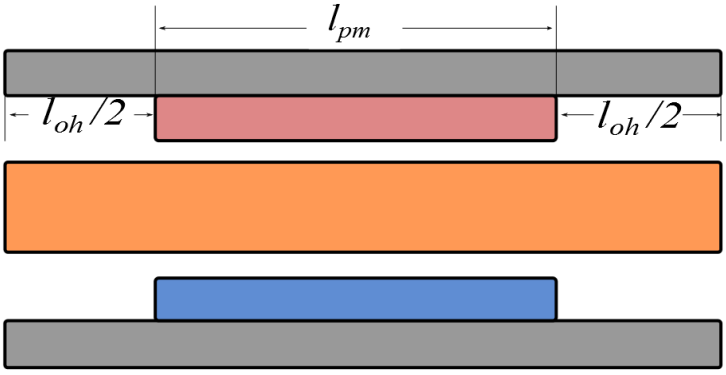

Figure 3.3. Axial cross section of the radial axis eddy current coupler.

3D torque of the coupler taking end effects into account.
- The calculated results are verified by transient 3D FEA calculations and simulations.

The torque calculation methodology uses the prototype coupler of Fig. 3.1 as a reference. The design specifications of the prototype coupler are given in Table I, with explanation of the dimensions given in Figs. 3.2 and 3.3.

3.1 3D torque calculation methodology

When designing the coupler, 3D transient FEA calculates the torque which is very close to practical measurements. In this way the torque of the coupler can be calculated using

$$\tau = \tau_{3D(FEt)} \tag{3.1.1}$$

where $\tau_{3D(FEt)}$ is the 3D transient FE solution of the torque. Although accurate, 3D transient FE simulations are computationally expensive, and hence completely impractical when used in conjunction with optimisation algorithms in the design of the coupler. The 2D transient FE solution ($\tau_{2D(FEt)}$) on the other hand is much faster, but does not deliver correct torque results, as shown in Fig. 3.4.

In [37] Russell and Norsworthy published a study on eddy currents and wall losses in screen-rotor induction motors, and uses a method of deducing 3D torque calculations from 2D results and taking end-effects into account. In this way the torque of the coupler is calculated as

$$\tau = K_e \tau_{2D(FEt)}, \tag{3.1.2}$$

where $\tau_{2D(FEt)}$ is the 2D transient FE solution of the torque and K_e is the so called Russell's end-effect factor in [37]. This end-effect factor is expressed by

$$K_e = 1 - \frac{\tanh(p\beta)}{(p\beta)(1+\lambda)}, \tag{3.1.3}$$

where p is the number of poles and $\beta = l_{pm}/d_c$ with l_{pm} the active axial length of the PM rotors and d_c the centre diameter of the cylinder conductor. In (3.1.3) λ is the overhang coefficient defined by

$$\lambda = \tanh(p\beta)\tanh(p\alpha\beta), \tag{3.1.4}$$

where $\alpha = l_{oh}/l_{pm}$ and l_{oh} the axial overhang length of the cylinder conductor as in Fig. 3.3. The variation of K_e as a function of α is shown in Fig. 3.5, with β a parameter.

In a first evaluation of the accuracy of (3.1.2) the 2D transient FE solution shown in Fig. 3.4 is multiplied by the end factor of the prototype coupler. With $\alpha = 0.4857$ of the prototype coupler, K_e is calculated as $K_e = 0.735$. Using this factor the calculated torque of the coupler according to (3.1.2) is as shown in Fig. 3.4. This shows that an accuracy of within 5 % is obtained, which is a first indication that (3.1.2) can be used instead of (3.1.1) to calculate the torque of the eddy current coupler. Note that in Fig. 3.4 a slip percentage region of only up to 10 % is considered in this study at a base speed of 375 r/min as given in Table I. This implies a slip frequency region of 0 - 5 Hz, which is the typical slip frequency region where eddy current couplers operate continuously and where they are optimally designed.

There are, however, two problems with regard to the calculation of the torque by (3.1.2). The first is that the 2D transient FE solution is still too expensive in terms of computational time when used in the design optimisation of the coupler. A much faster analytical-based calculation method is required that

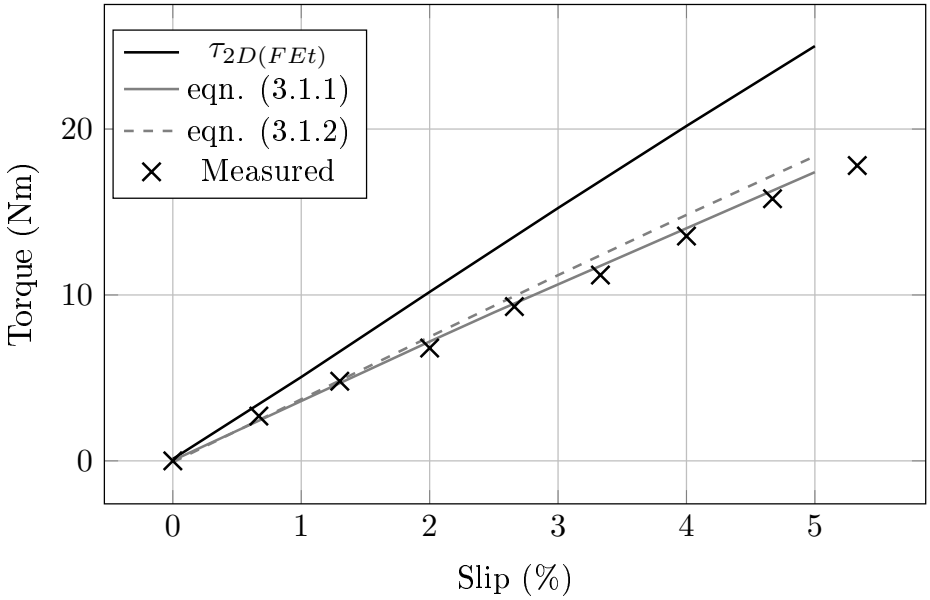

Figure 3.4. 3D FEA (3.1.1), semi-analytical (3.1.2) and measured results of torque versus slip of the prototype coupler.

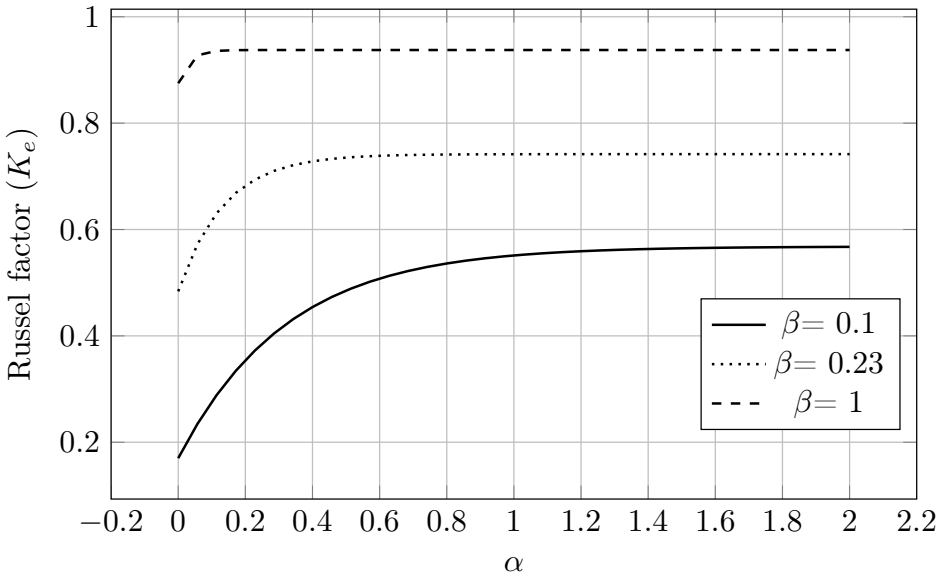

Figure 3.5. Russell's end-effect factor as a function of α with β a parameter.

is proposed and evaluated later in this chapter. The second problem is the accuracy of the Russell factor K_e for extreme design dimensions of the coupler. This is very important when (3.1.2) is used in the design optimisation of the coupler. In sections V and VI the accuracy of K_e is evaluated in detail against 3D transient FE solutions for radial-flux couplers.

3.2 2D torque calculation method

This section contains the derivation of an analytical expression for the 2D torque of the radial-flux coupler, followed by a computationally efficient FEA approach to solve the analytical torque expression.

3.2.1 Analytical 2D torque expression

In the proposed analytical calculation of the 2D torque of the eddy current coupler the solid cylinder conductor is divided into a number of radial layers i, each with an average conductor layer radius r_{ci}, as shown in Fig. 3.7. Assuming that under low slip frequency the conductor layers are only resistive, and using the Lorentz force law as in [37] and [42], an expression for the 2D torque can be derived. Modelling the torque calculated by the current flowing in a conductor element of the cylindrical conductor of the eddy current coupler at electrical position θ as shown in Fig. 3.6. The expression for the torque of the element of Fig. 3.6 in the i^{th} conductor layer is

$$\tau_{\theta i} = \frac{4}{p^2} \frac{r_{ci}^3 h_{ci} l_{pm}}{\rho} \omega_e B_i^2 \mathrm{d}\theta, \tag{3.2.1}$$

where r_{ci} is the middle radius, h_{ci} the height (thickness), l_{pm} the axial length and ρ the resistivity of the conductor element. Furthermore in (3.2.1) B_i is the radial flux density value and ω_e is the relative electrical angular velocity (or angular slip frequency) between the conductor and the flux density wave. By integrating (3.2.1) over one electrical pole pitch of π radians and multiplying by p poles the torque of the coupler is given by

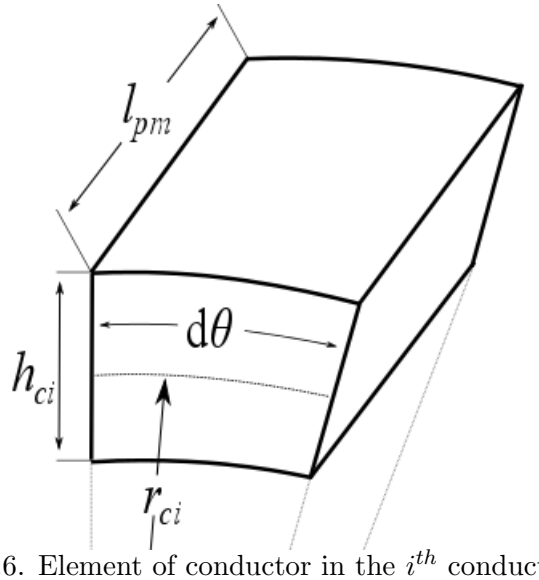

Figure 3.6. Element of conductor in the i^{th} conductor layer.

$$\tau_{ri} = \frac{4}{p}\frac{r_{ci}^3 h_{ci} l_{pm}}{\rho}\omega_e \int_0^{\pi} B_i^2 \mathrm{d}\theta \tag{3.2.2}$$

With $B_i(\theta+\pi) = -B_i(\theta)$ and $B_i(-\theta) = -B_i(\theta)$ there are respectively no even Fourier harmonics and no cosine terms in the series, hence B_i of (3.2.2) can be expressed as a function of θ as

$$B_i(\theta) = B_{1i}\sin(\theta) + B_{3i}\sin(3\theta) + B_{5i}\sin(5\theta)... \tag{3.2.3}$$

Replacing B_i in (3.2.2) by (3.2.3) and knowing that for the n^{th} harmonic order that

$$\int_0^{\pi} B_{ni}^2 \sin(n\theta)^2 \mathrm{d}\theta = B_{ni}^2 \frac{\pi}{2} \tag{3.2.4}$$

the torque of (3.2.2) can be expressed as

$$\tau_{ri} = \frac{2\pi}{p}\frac{r_{ci}^3 h_{ci} l_{pm}}{\rho}\omega_e [B_{1i}^2 + B_{3i}^2 + B_{5i}^2 + ...] \tag{3.2.5}$$

In (3.2.5) ω_e is the fundamental slip angular frequency. The importance of the layers is that the radial flux density harmonic content in the layer that is close to the magnets can substantially differ from that in the layers in the middle of the conductor. For thicker conductors the number of layers are increased to ensure accurate information of the radial flux density distribution in the conductor. With k layers ($k = 4$ in Fig. 3.7) the 2D torque is calculated from (3.2.5) simply as

$$\tau_r = \sum_{i=1}^{k} \tau_{ri}. \tag{3.2.6}$$

To take the end-effects into account as in (3.1.2) the torque of the eddy current coupler is calculated analytically by

$$\tau = K_e \tau_r \tag{3.2.7}$$

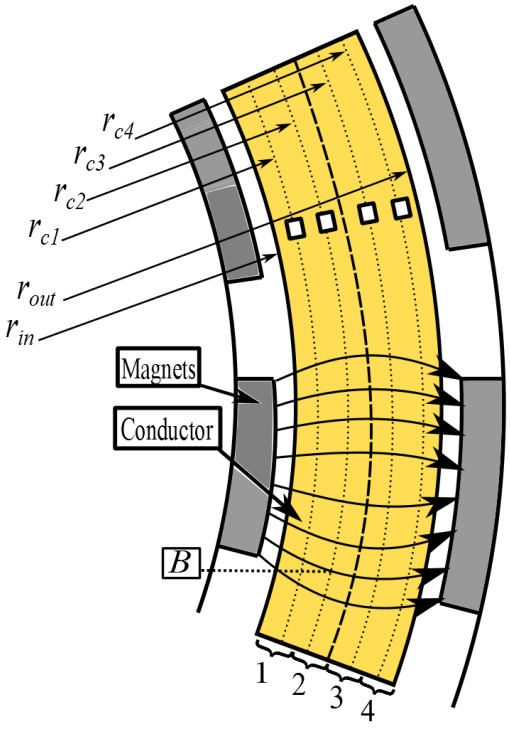

Figure 3.7. Cross section of eddy current coupler showing conductor layers.

3.2.2 Semi-analytical 2D torque calculation

The radial flux density harmonics of (3.2.5) are affected amongst others by armature reaction, rotor yoke saturation and curvature effects. Also the curved inner and outer magnets and magnet material characteristics must be accurately represented in the solution of the flux density harmonics.

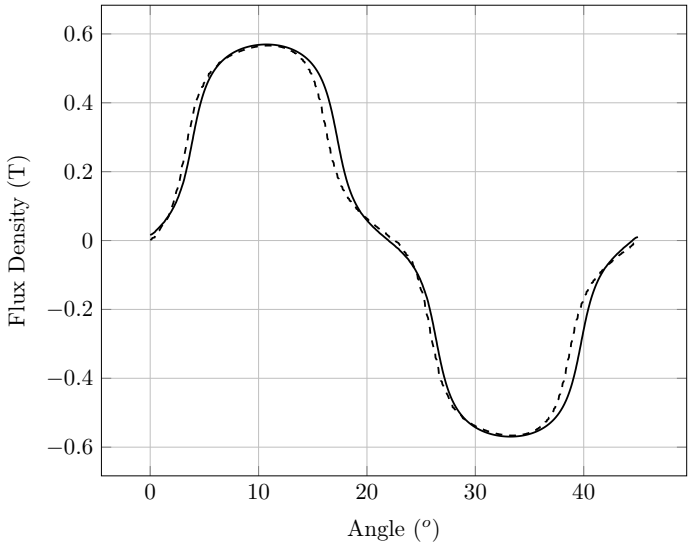

Figure 3.8. Radial flux density waveform of the eddy current coupler with (dotted line) and without(solid line) armature reaction.

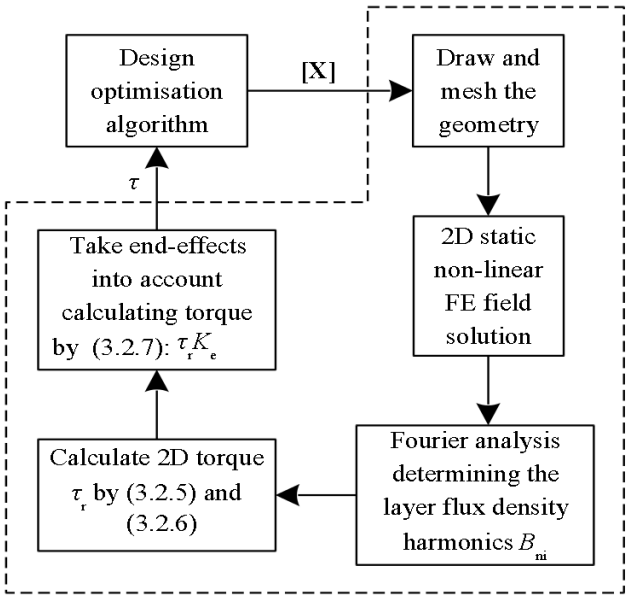

Figure 3.9. Torque calculation process in design optimisation of the eddy current coupler.

To consider the effect of armature reaction, Fig. 3.8 shows the waveforms of the radial flux density in a conductor layer with and without armature reaction; the armature reaction waveform is obtained from 3D transient FEA. This shows that the armature reaction effect is small. It was also found that taking this effect into account made very little difference in the torque calculation of (3.2.5). Hence, the armature reaction effect on the flux density harmonics is ignored in this calculation method. Making this assumption only valid for low slip frequencies. Higher slip frequencies may increase the armature effect and affect the analytic results, but since the focus is on high efficiency low slip speed it doesn't form part of this study.

With armature reaction ignored it is possible to obtain all the radial flux density harmonic information of all the layers from only one 2D static non-linear FE solution and also by considering only one pole section of the coupler. Such a solution takes into account saturation, curvature-effects and the magnet-material characteristics. The radial flux density harmonics of (3.2.5) of each layer can be obtained by Fourier analysis of the layer radial flux density waveform available from the 2D static FE solution. Note that in this study only the lower flux density harmonic orders of $n = 1, 3, 5, 7$ are considered.

In Fig. 3.9 the torque calculation method as described above is summarized. Also shown is how this calculation fits in a design optimisation process. The optimisation algorithm send the design dimensions and slip frequency of the coupler to the machine analysis software (marked by dotted lines) asking to calculate the torque. The machine analysis software draws and meshes the ge-

ometry and completes a 2D static non-linear FE solution of the given machine structure. From this the Fourier radial flux density harmonics of the layers are determined, followed by the calculation of the torque according to (3.2.5) - (3.2.7) and the feedback of the calculated torque, τ, to the optimisation algorithm.

3.3 2D semi-analytical method results

It is important in design optimisation to confirm the accuracy of the proposed 2D semi-analytical torque calculation of (3.2.5) and (3.2.6) against 2D transient FEA torque calculation, $\tau_{2D(FEt)}$, for extreme variations of machine design dimensions. In this section the effect of varying the conductor thickness, magnet thickness and magnet pitch on the accuracy of (3.2.5) and (3.2.6) is investigated.

3.3.1 Conductor thickness

Three conductor thickness of the prototype coupler are considered in the analyses as shown by the cross sections in Fig. 3.10 and 3.11. The torque versus percentage slip results of the different calculations are compared in Fig. 3.12. It is clear that the results of the semi-analytical calculation method are very accurate for conductor thicknesses up to $h_c = 8$ mm and slip speeds up to 5 Hz as shown in Fig. 3.12(a). However, when the conductor size is increased to $h_c = 48$ mm, the 2D transient FE torque of the coupler at high slip speeds is significantly lower than that predicted by (3.2.5) and (3.2.6), as shown in Fig. 3.12(b). A more detailed investigation into this calculation error is shown

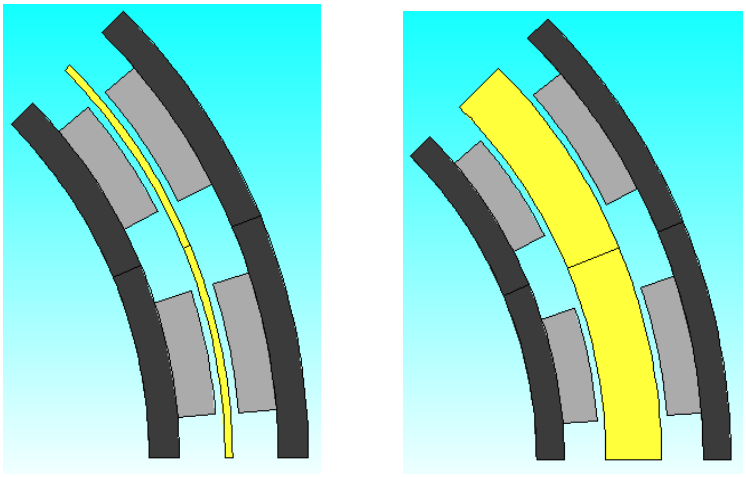

Figure 3.10. Radial-flux eddy current coupler with conductor thickness of (a) $h_c = 1$ mm and (b) $h_c = 8$ mm.

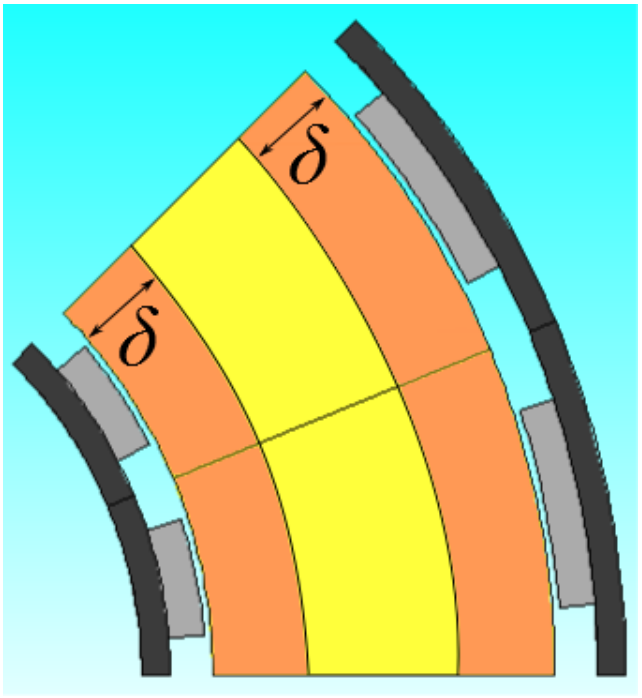

Figure 3.11. Radial-flux eddy current coupler with conductor thickness of $h_c = 48$ mm and δ the skin depth.

in Fig. 3.13(a), where the percentage error is plotted versus slip speed with conductor thickness a parameter. From this it is clear that the percentage error in the calculation increases with slip speed and conductor thickness.

The phenomenon in Fig. 3.13(a) can be explained by the skin effect, which is the tendency of the induced current to flow at higher frequencies only within the skin depth (δ) at the inner and outer surfaces of the cylindrical conductor as illustrated in Figs. 3.11 and 3.14. This skin depth is calculated as

$$\delta = \sqrt{\frac{2\rho}{\omega_e \mu}}, \tag{3.3.1}$$

where ρ is the resistivity of the conductor, μ the permeability of the conductor, and ω_e the slip frequency. From (3.3.1), with an increase in slip frequency the skin depth of the induced current flow in the conductor decreases, causing the amount of induced eddy currents and hence torque to reduce, as shown by the results of the 2D transient FE analysis in Fig. 3.12(b).
To compensate for this in (3.2.5) the skin depth δ is first calculated at the considered fundamental slip frequency by (3.3.1). If $2\delta < h_c$, then only the layers i that are within the skin depths of the conductor, that is where $r_{in} < r_{ci} < (r_{in} + \delta)$ and $(r_{out} - \delta) < r_{ci} < r_{out}$, are considered in (3.2.5). With skin effect taken into account in this way, the accuracy of the 2D semi-analytical torque calculation of (3.2.5) and (3.2.6) improves to be within 1 % of the 2D transient FE torque calculation for all conductor thicknesses as shown in Fig.

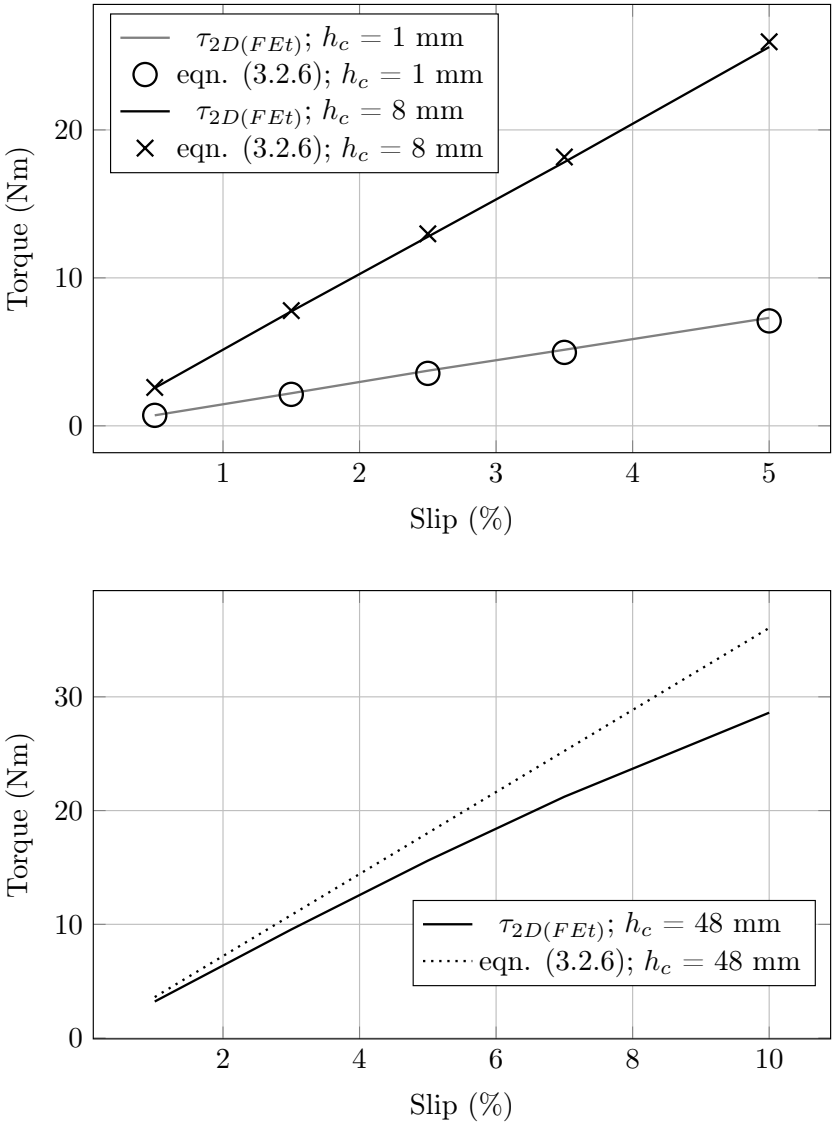

Figure 3.12. 2D analytical and 2D transient FEA calculated torque versus slip of the eddy current coupler with (a) $h_c = 1$ mm and $h_c = 8$ mm conductors and (b) $h_c = 48$ mm conductor.

3.13(b). It must be noted that to be strictly correct the skin depths have to be calculated for each harmonic slip frequency $\omega_{en} = n\omega_e$ and then used accordingly to determine the active layers for that harmonic and from that the harmonic torque. This is not used as it was found that it makes very little difference in the calculated torque. The reason for the latter is that with relatively thick conductors the radial flux density distribution in the conductor is quite sinusoidal with a low harmonic content.

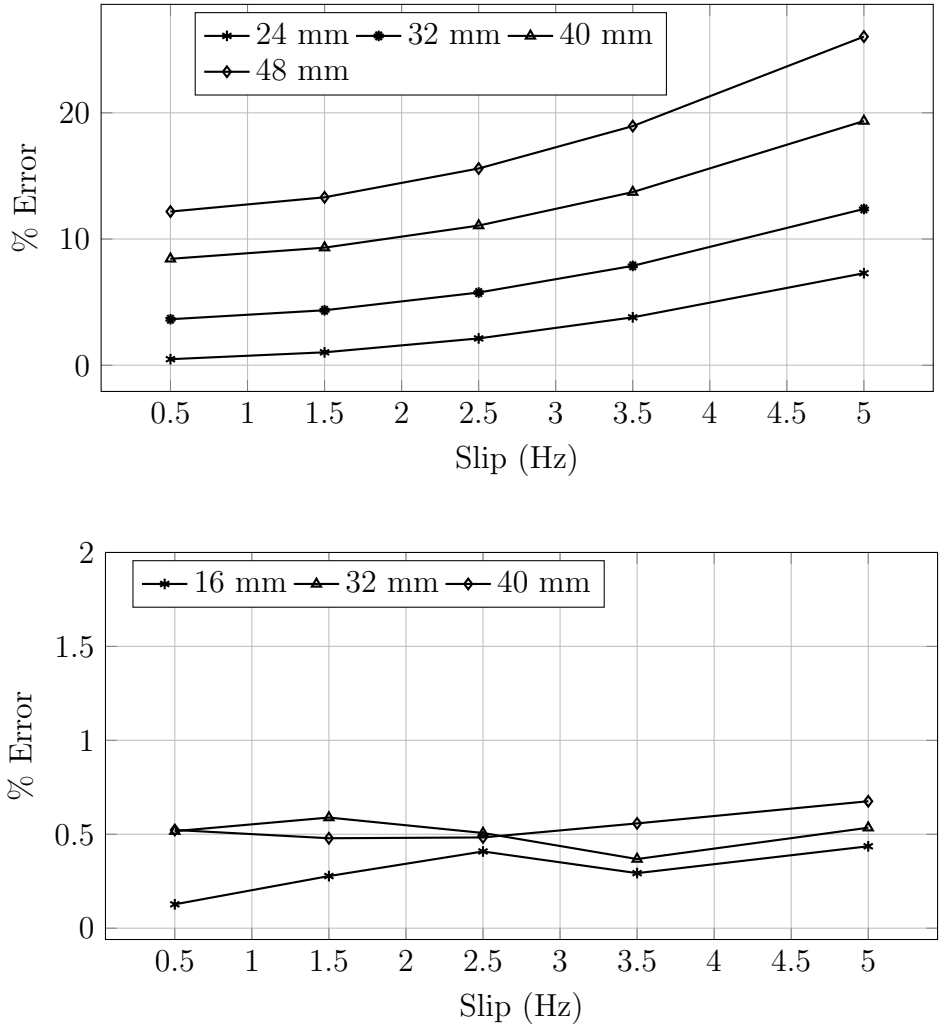

Figure 3.13. Percentage error of the 2D semi-analytical torque calculation with conductor thickness a parameter, with skin effect (a) not taken into account and (b) taken into account.

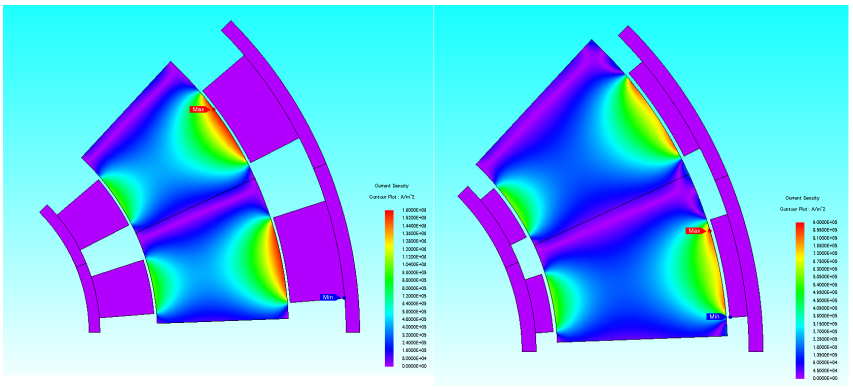

Figure 3.14. Visible skin effect where the current density is high only near the inner and outer surfaces of the conductor.

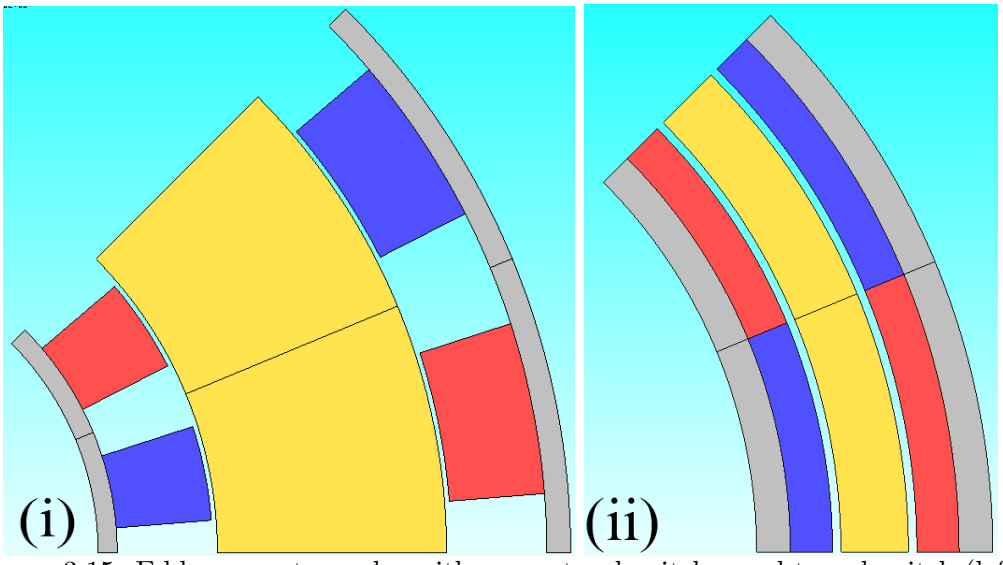

Figure 3.15. Eddy current coupler with magnet pole pitch equal to pole pitch (left) and thick magnets (right).

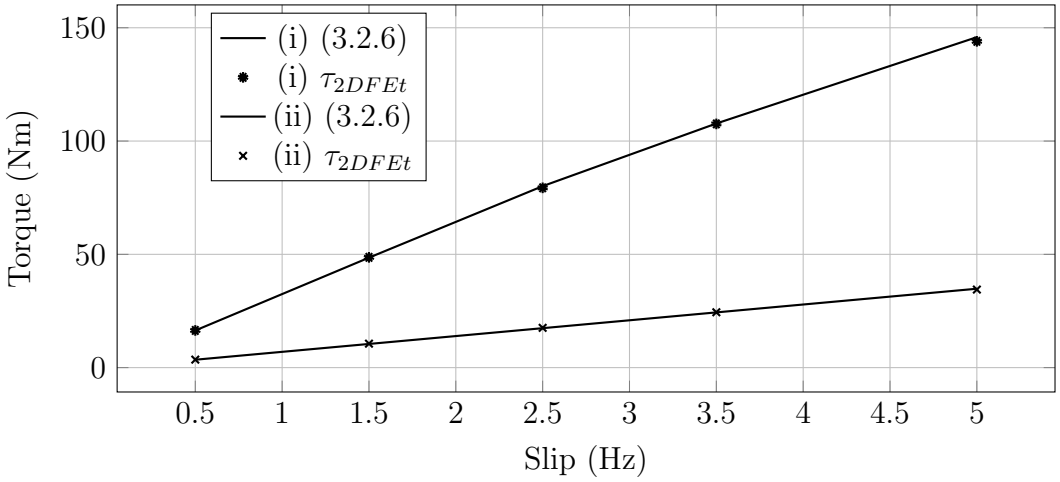

Figure 3.16. 2D semi-analytical and transient FEA torque versus slip of the eddy current couplers (i) and (ii) of Fig. 3.15

3.3.2 Magnet thickness and pitch variation

Two further variations in the dimensions of the prototype eddy current coupler are investigated. In Fig. 3.15(i) the magnet thickness is increased and in Fig. 3.15(ii) the magnet pitch is set equal to the pole pitch. The skin effect is shown in Fig. 3.14 for the thick conductor where the current density remains near the surfaces of the conductor even when the magnet thickness is increased. Taking skin effect now into account in (3.2.5) and (3.2.6) as described above, the comparisons of torque versus slip of the two calculation methods for both cases of Fig. 3.15 are shown in Fig. 3.16. This clearly shows the accuracy of the proposed 2D semi-analytical method.

3.4 Accuracy of the end-effect coefficient

In [16] the accuracy of an analytical equation using K_e of (3.1.3) to take end-effects into account is evaluated for axial-flux eddy current couplers with different pole pairs and different conductor dimensions. In this evaluation errors not larger than 17 % were found at a relatively high slip frequency of 12.5 Hz.

In this section the accuracy of K_e is evaluated for radial-flux eddy current couplers with extreme cylindrical conductor dimensions. The accuracy of K_e is evaluated by comparing the torque calculation of (3.1.2) with the 3D transient FEA calculation as expressed by (3.1.1). From (3.1.3) it can be seen that K_e is a function of the number of poles and of α and β as shown in Fig. 3.5. In this

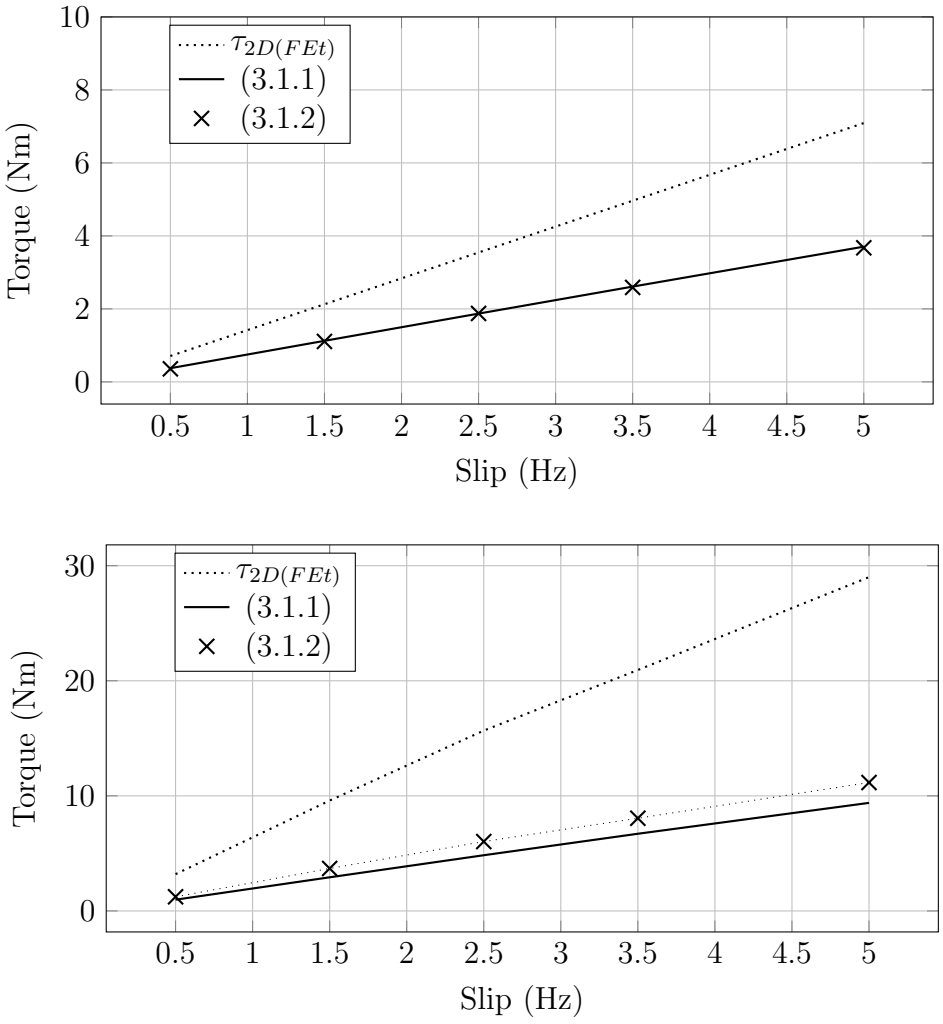

Figure 3.17. Accuracy of torque versus slip calculation using Russell's end-effect factor [(3.1.2)], by comparing it with 3D transient FEA of (3.1.1) for (a) $h_c = 1.0$ mm $[\alpha = 0; \beta = 0.241]$ and (b) $h_c = 48$ mm $[\alpha = 0; \beta = 0.182]$.

study the number of poles are kept constant at $p = 16$ as for the prototype, and α and β are varied to the extreme.

In a first comparison the torque versus slip is calculated for thin ($h_c = 1$ mm) and very thick ($h_c = 48$ mm) conductors with $\alpha = 0$ and $\beta = 0.241$ (thin conductor) and $\beta = 0.182$ (thick conductor). The results of this calculation as shown in Fig. 3.17 show excellent comparison with $\beta = 0.241$, but with about a 16% error when $\beta = 0.182$.

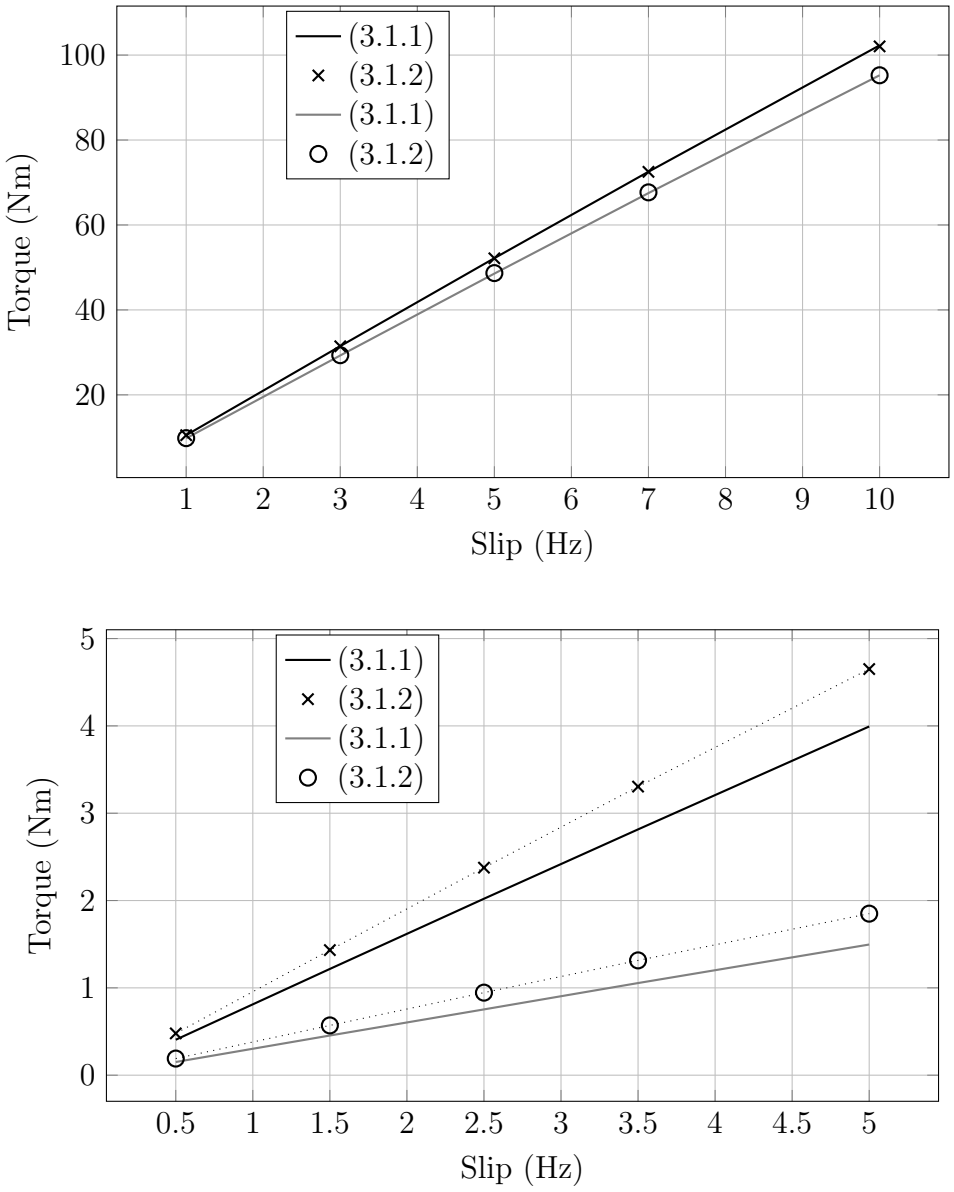

Figure 3.18. Comparison of calculated torque versus slip using 3D transient FEA [(3.1.1)] and Russell's end-effect factor [(3.1.2)] with α a parameter and (a) $\beta = 1$, (b) $\beta = 0.1$.

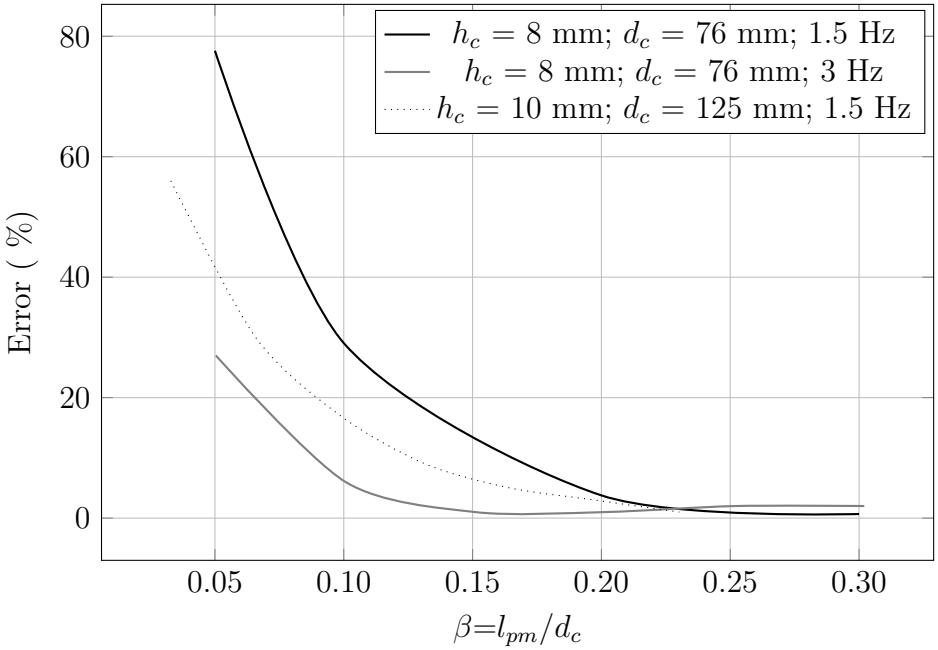

Figure 3.19. Percentage calculation error versus $\beta = l_{pm}/d_c$ with h_c, d_c and frequency parameters.

In Fig. 3.18 the calculated torque versus slip results are shown for $\alpha = 0$ and $\alpha = 1$ and with $\beta = 0.1$ and $\beta = 1.0$. Note that Fig. 3.4 shows the results for the prototype with $\beta = 0.23$. There is a very good agreement between the results of (3.1.1) and (3.1.2), except for the cases where β becomes small (i.e. axially short, radially large couplers), as in Figs. 3.17(b) and 3.18(b).

To investigate the error in the calculation in more detail when β becomes small, the eddy current coupler of Fig. 3.10(b) was simulated at slip frequencies of 1.5 Hz and 3 Hz for small to large values of β. This simulation study was also repeated for a larger in diameter coupler. The results of the percentage error found in the calculation compared to 3D FEA results are shown in Fig. 3.19. It is clear that with $\beta < 0.2$ the accuracy of the end-effect coefficient K_e of (3.1.3) drops, with errors in the calculated torque according to (3.1.2) larger than 10 %.

3.5 Practical results and method validation

The measurement set-up for the practical tests is shown in Fig. 3.20(a) where the torque and slip frequency of the coupler are measured. Four rotors of various conducting materials and overhang as shown in Fig. 3.20(b) were tested; the design detail of the conductor rotors is summarized in Table 3.2. For the torque calculations of the coupler with the different conductors, (3.1.1) and (3.2.7) were used. The torque calculations were done at the same conductor

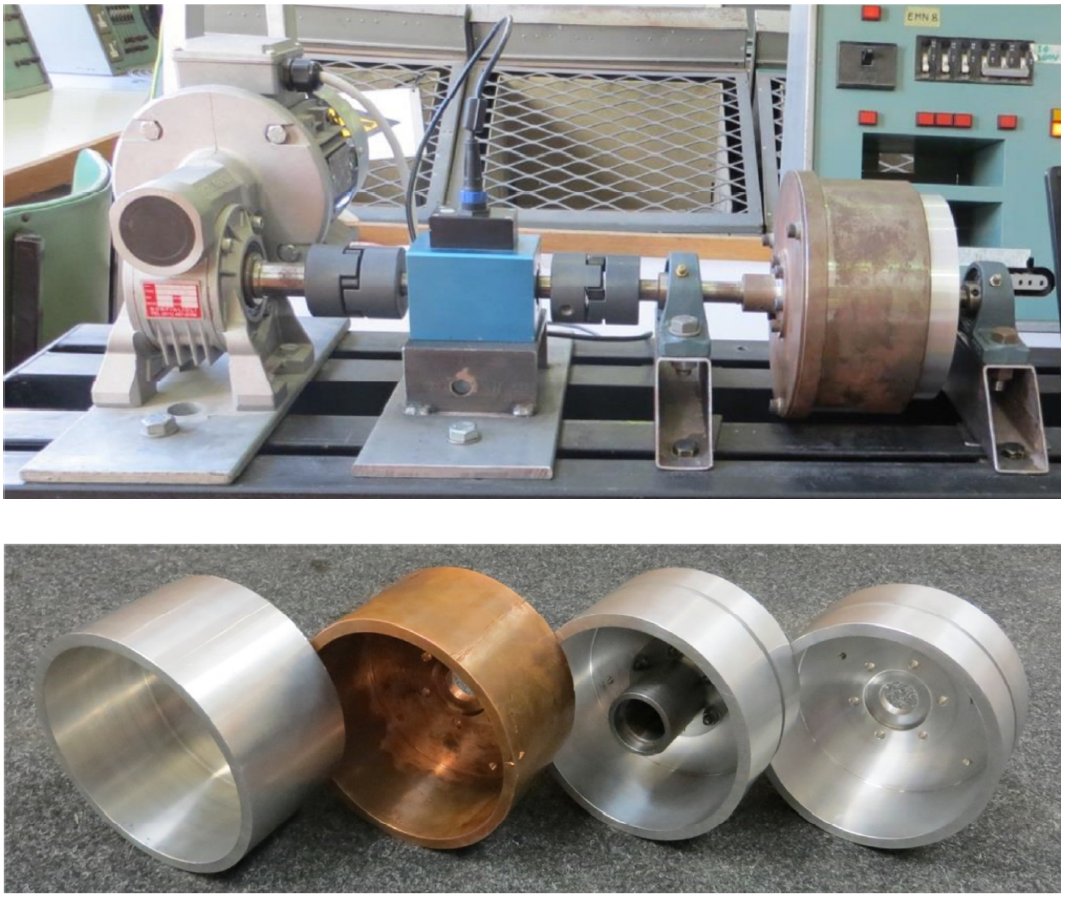

Figure 3.20. Eddy current coupler prototype (a) practical laboratory test set up and (b) four conductor types explained in Table II.

temperatures as were measured. The built models were run and tested under rated conditions to verify the temperature range of the coupler. A temperature of 60 ^{o}C was measured after 60 minutes of operation time.

The calculated and measured results of the coupler with the four conductors are shown in Figs. 3.21 and 3.22. From this it is clear that the calculated results according to (3.1.1) and (3.2.7) correlate well with each other and also compare well with the measured results. Furthermore, the huge effect of copper conductor material above aluminium on the torque performance of the coupler is clear from Fig. 3.21; the torque almost doubles with copper material due to the much lower resistivity of copper. Finally, the effect of conductor overhang on the torque performance of the coupler is shown in Fig. 3.22, where the overhang conductor generates a larger torque as also predicted by the Russell factor.

Table 3.2. Conductor properties.

Conductor	1	2	3	4
Material	Cu	Al	Al	Al
h_c	8 mm	8 mm	8 mm	8 mm
l_{oh}	Max	Max	Equal	Zero
T at 2 Hz	6.8 Nm	3.35 Nm	3.4 Nm	2.6 Nm
α	0.243	0.243	0.143	0

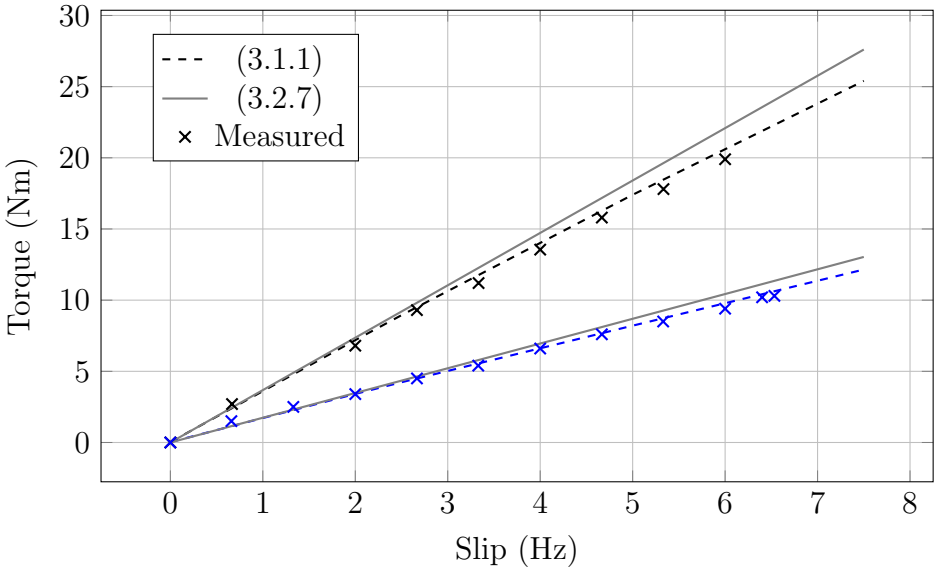

Figure 3.21. Torque versus slip frequency of copper (black) and aluminium (blue) conductors 1 and 2 of Table II..

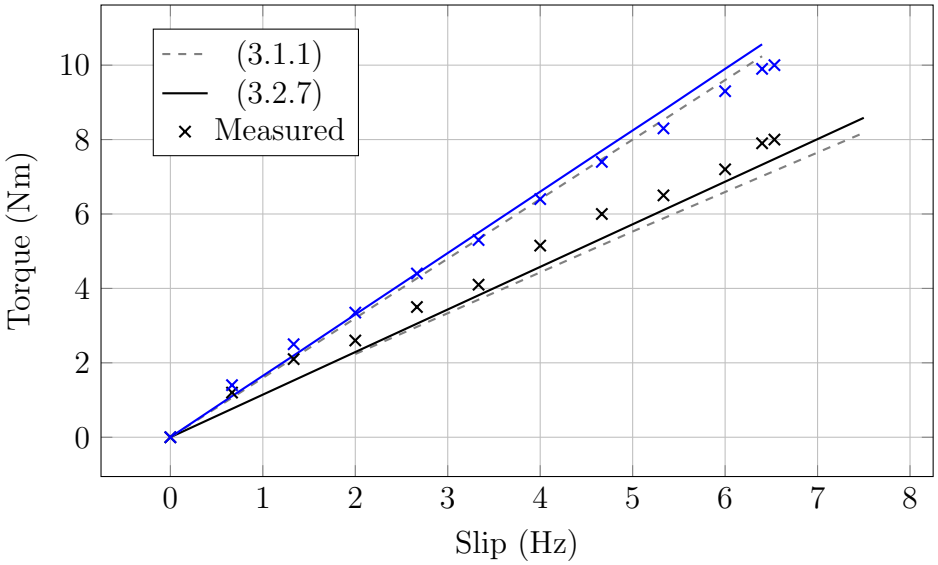

Figure 3.22. Torque versus slip frequency of the equal (blue) and zero (black) overhang aluminium conductors 3 and 4 of Table II.

3.6 Temperature effects

Currents induced in the conductor cause a temperature increase of the coupler. To include this effect in the model, the new resistivity of the conductor is

estimated using the Temperature Coefficient of Resistance

$$\rho_{new} = \rho_{ref}[1 + (\alpha_t)(T - T_{ref})], \tag{3.6.1}$$

where ρ_{new} is the conductor resistivity at temperature T, ρ_{ref} is the conductor resistivity at room temperature, α_t the temperature coefficient of resistance for a conductor, T the conductor temperature and T_{ref} the reference temperature. To account for the effect of temperature on the torque rating of the coupler, (3.6.1) is used along with the torque and skin effect calculations. The built model was run and tested under rated conditions to verify the temperature range of the coupler.

Measurements with a infra-red camera, the temperature was measured to be between 60 ^{o}C and 70 ^{o}C. Figure 3.23 shows the internal temperature of the coupler to be 60 ^{o} Celsius.

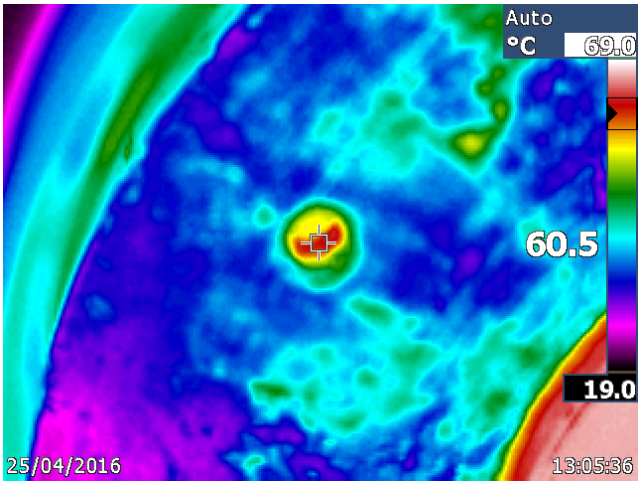

Figure 3.23. Internal temperature measurement of the conductor of the coupler.

3.6.1 Summary

In this section the analytical approach to solving the torque developed in the coupler is explained and discussed. Results from the simulations indicate that the 2D CE FEA method is faster than a 2D transient FEA method. Furthermore, the method was evaluated for extreme dimensions of the machine revealing the importance of including the skin effect into the calculation process. The 2D CE FEA is validated with 3D transient FEA and the results show that the proposed method is accurate.

This chapter also evaluates the Russell end effect factor and its accuracy. It was shown that the end effect factor is inaccurate when β is smaller than 0.2

but larger β values provide an accurate result.

The Russell end effect factor is evaluated in terms of zero and equal overhang conductors. It is shown that the 3D end effect factor is accurate for zero and equal conductor overhangs. These results suggest that there is an optimum overhang where torque per conductor material cost becomes a maximum.

It is shown that the proposed semi-analytical method predicts the torque of the coupler very accurately compared to measured results for various conductor materials and conductor overhangs. In these calculations and measurements, amongst others, the almost doubling effect on the torque performance of the coupler with copper material above aluminium material is shown.

Chapter 4

Design methodology

As shown in the previous chapter, a fast and accurate method of obtaining a torque result is possible by using the proposed computationally efficient FEA (CE-FEA). Thus, thousands of solutions can be generated within a few hours. This opens an area for investigation into computationally intensive optimisation algorithms that would take a fraction of the time compared to using a standard 3D FEA.

In this chapter methods to solving a multi-objective, constrained design optimisation problem are investigated. Population (NSGA-II) [43] and gradient (MMFD) [33] based design optimisation methods are evaluated in terms of speed of finding a solution and optimised result and the accuracy of that result. The final solutions are compared to a 3D FEA to determine their accuracy. It is also for consideration what kind of conductor is optimal in terms of active mass and cost of the eddy current coupler.

The focus of this chapter is to obtain an optimal design using a 3D CE-FEA in a design optimisation environment and to investigate the optimal design in terms of materials and machine constraints. The second part is an analysis of the effect of the input variables on the results by using a novel colour-gradient distribution. The final part of the chapter is a 3D FEA validation of the results.

4.1 Design specifications and constraints

It is important to simplify the design specifications so that the design algorithm has the least amount of variables and constraints as discussed in [44]. This is an important step in reducing the convergence time of the algorithms that are utilized.

The coupler is to be used in a wind turbine drive train with a turbine rota-

tional speed of 150 r/min, attached to a gearbox with a 3.9 ratio, providing a coupler rotational speed of 600 r/min. It should operate at an efficiency of 97 %, and function as a low pass filter. The outer diameter and the stack length of the coupler is constrained to not be more than 30 cm and 65 mm respectively. Furthermore, the coupler is required to transfer 35 Nm torque from one rotor to the other, over an air gap of 1 mm. The air gap should not be smaller than 1 mm, due to misalignments between the shafts of the two mechanical systems and also allowing for manufacturing tolerances.

If the machine has 32 poles (p), it can operate at a slip frequency (f_{slip}) of up to 4.5 Hz. This is calculated using $p = \frac{120 f_{slip}}{s n_s}$.

The pole number is an important variable in the optimisation process as well as how effective the coupler functions as a low pass filter. Taking the poles as $p = 32$ the slip frequency is 4.5 Hz, which is a typical eddy current coupler frequency. If the pole number is increased to $p = 64$, the coupler operates at a slip frequency of 9.0 Hz. The optimisation includes pole numbers ranging from 20 to 90 poles and thus an eddy current frequency ranging from 3 Hz to 9 Hz.

The comparison between using a copper or aluminium conductor as a rotor is important. Because aluminium has a higher resistivity than copper, it won't be able to transfer as much torque per volume. Even though aluminium has higher resistivity than copper, its advantage is cost per kilogram and has a lower mass density. These material properties are summarized in Table 4.1.

Table 4.1. Design Specifications of the coupler.

Power rating	2.2 kW
Torque	35 Nm
Speed	600 r/min
Efficiency η	97 %
Slip %	3 %
Slip Speed	18.56 r/min
f_{slip}	4.5 Hz
Air gap	1 mm

Table 4.2. Design Constraints for the coupler.

Conductor 1: Copper
Conductor 2: Aluminium
Magnet 1: NdFeB N52
Outer Diameter: $r_c < 300mm$
Beta: $\beta > 0.2$

4.2 Design optimisation

To find the optimal design for the eddy current coupler, two design optimisation algorithms are evaluated against the constraints in Table 4.2. The following chapter consists of an analysis of these two algorithms for finding an optimal solution for the design of the eddy current coupler. Among them is the gradient based Modified Method of Feasible Directions (MMFD) and the population based Non-dominated Sorting Genetic Algorithm (NSGA-II), the latter being a popular multi objective optimisation method.

The MMFD is a non-linear, gradient based algorithm that utilises the method of feasible directions to determine a search direction. The MMFD algorithm is fast and doesn't require a lot of core resources, but the method needs some supervision in order to obtain the best solution. Gradient based design algorithms aren't as popular as their genetic and evolutionary counterparts, but it outperforms most algorithms in terms of its speed. A significant drawback of the MMFD algorithm is its inability to handle dynamic design constraints. For example: When looking for an optimum with pole numbers included in the analysis, the MMFD solutions diverge when compared to optimising without the pole number.

The population based NSGA-II is an elitist genetic algorithm that is an improvement on its predecessor NSGA-I. Its use of elitism makes the algorithm's non dominated sorting a lot simpler, resulting in a faster genetic algorithm. The NSGA-II searches for the optimal solution in a large pool of simulation results, making it a lot slower than the MMFD, but the result obtained is considered optimal. Much like the MMFD, the NSGA-II looks for a solution in a specific direction, but unlike the MMFD that only takes a single/linear route, the NSGA looks at multiple solution possibilities and generates a pareto curve. Because this algorithm analyses the full spectrum of design constraints, it can obtain an optimum when a dynamic variable is present.

The optimisation process is dependant on a CE-FEA, and works in conjunction with the design algorithm as shown in the flow diagram of Fig. 4.1. The input and output parameters passed to and from the CE-FEA are listed in Table 4.3. Return parameters include torque, mass and cost. The multi-objective problem has two objective functions. These objectives are output variables that are either minimised or maximised. With many iterations of different input variable values, the algorithms 'find' the optimum set of input values that meets all objectives. One of these objectives for the eddy current coupler is to minimise the mass, resulting in a lightweight design. This is especially an interesting variable to consider when comparing different conductor topologies. The other is the cost objective function that is mostly influenced by the price and mass of the NdFeB magnets. A cost function is adapted from [45], as well

Table 4.3. Design Input and Output Parameters

Input [**X**]	Boundary Cu (Al)	Per Unit Multiplier
r_c	$0.5 < r_c < 1.6(2.0)$	0.1
h_c	$0.1 < h_c < 1.0$	0.01
h_{y1}	$0.05 < h_{y1} < 1.0$	0.02
h_{y2}	$0.05 < h_{y2} < 1.0$	0.02
h_m	$0.1 < h_m < 1.0$	0.01
$poles$	$0.0 < h_m < 1.0$	$60 + 20$
θ_p	$0.128 < \theta_p < 1.0$	$2\pi/p$
l_{pm}	$0.95(1.3) < l_{pm} < 1.5$	0.06
l_{oh}	$0.0 < l_{oh} < 1.5$	0.01
Output [**Y**]		
Torque	$34 < \tau_r < 36$	
Cost	$0 < Cost < 5000$	

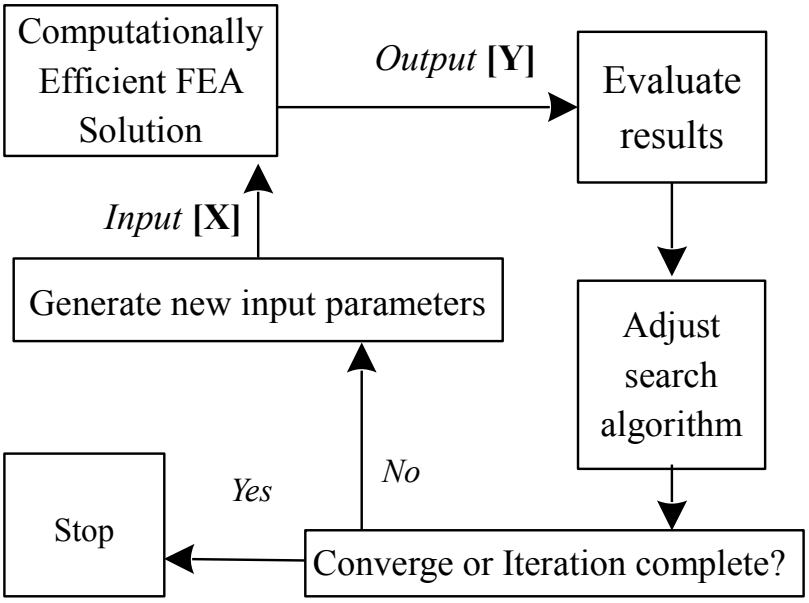

Figure 4.1. Design optimisation flow diagram.

as independent material market research to verify and adjust to local prices. The active mass objective function is the sum of all the parts used in torque transfer.
The objective functions,

$$F_1[\mathbf{X}] = m_{pm} + m_{Fe} + m_{cond} \tag{4.2.1}$$

$$F_2[\mathbf{X}] = (100m_{pm} + m_{Fe} + K_c m_{cond}) \tag{4.2.2}$$

are minimised, where as m_{cond} and factor K_c is subject to the conductor material as in,

$$K_c = \begin{cases} 20 & \text{if } m_{cond} \text{ is Copper} \\ 9.5 & \text{if } m_{cond} \text{ is Aluminium} \end{cases}, \tag{4.2.3}$$

$$m_{pm}[h_m, l_{pm}, m_p, r_c, h_c, agap, h_m] \tag{4.2.4}$$
$$m_{Fe}[h_{y1}, lpm, r_c, h_c, agap, h_m, h_{y2}] \tag{4.2.5}$$
$$m_{cond}[h_c, l_{pm}, r_c] \tag{4.2.6}$$

where m_{pm}, m_{Fe}, m_{cond} are the masses in kilograms of the magnet material, steel laminations and conductor respectively. The cost and mass functions are both subject to the volume of the material and are subject to the machine parameter sets in 4.2.4 - 4.2.6.

4.3 Results

A computationally efficient 3D FEA can now be used in conjunction with design optimisation methods to find the optimal design pareto front. The variables and constraints have all been normalised and range between the values as shown in Table 4.3. A set of optimisations were executed in order to obtain the optimal design parameters for copper and aluminium conductor couplers. The time difference between the two methods discussed below is shown in Table 4.4.

4.3.1 Modified method of feasible direction

As stated earlier, the MMFD requires some form of supervision and guidance of the designer in order to obtain a good result. To obtain one solution it took the optimiser 15-20 minutes to reach convergence. Upon investigation into the constraint ranges the optimiser considered, it was found that some cases were in fact initially overlooked. It is thus a requirement to restart the MMFD at different initial values and repeating the optimisation procedure. By repeating this process 8-10 times, each time selecting new initial variables, the optimiser gave a satisfactory result. This method proved to be fast (2-3 hours) but required a lot of insight and understanding of the effect of each variable and constraint has on the output of the machine. The results of the MMFD is shown in Table 4.5 and shown in Fig. 4.2.

Table 4.4. Performance of the CE-FEA and design optimisation algorithms.

3.2.7	0.5 sec
3.1.1	3 hours
MMFD	2 hours
NSGA-II	36 hours

4.3.2 Non-dominated sorting genetic algorithm method

The NSGA-II aims to map all the possible solutions that are within the set boundaries and constraints, and selects an optimal solution from the generated pareto front. The pareto front that is generated shows the effect of opposing constraints on the output parameters. The downside of this method, is that it takes a long time (± 2 days) and a lot of simulations (± 20 000) in order to find the optimal solution. The advantage is that it provides a result that is optimal in more ways than the MMFD, because it evaluates almost every case in order to achieve its objectives. The eddy current couplers with aluminium and copper conductors are shown in Fig. 4.2 from the optimal result that is given in Table 4.5. The pareto fronts generated by the algorithm is shown in Figs 4.3-4.4, and it shows how the algorithm adjusts the variables in order to obtain the lowest cost and active mass and shows that as cost decrease, the active mass increase and vice versa.

Table 4.5. Design optimisation results

Input [**X**]	MMFD Cu	NSGA Cu	MMFD Al	NSGA Al
r_c	135 mm	139 mm	159 mm	160 mm
h_c	5.4 mm	8 mm	5.2 mm	6.8 mm
h_{y1}	1 mm	1 mm	1.2 mm	1.1 mm
h_{y2}	1 mm	1 mm	1.25 mm	1 mm
h_m	1.8 mm	1.8 mm	1.9 mm	1.8 mm
θ_p	6.3^o	7^o	5.8^o	6.3^o
l_{pm}	60 mm	54 mm	60 mm	60 mm
l_{oh}	10 mm	18 mm	13 mm	9.5 mm
Output [**Y**]				
F_1 (4.2.1)	3.13 kg	2.875 kg	3.47 kg	3.24 kg
m_{pm}	0.77 kg	0.82 kg	0.896 kg	0.949 kg
F_2 (4.2.2)	0.884	0.903	0.900	0.945

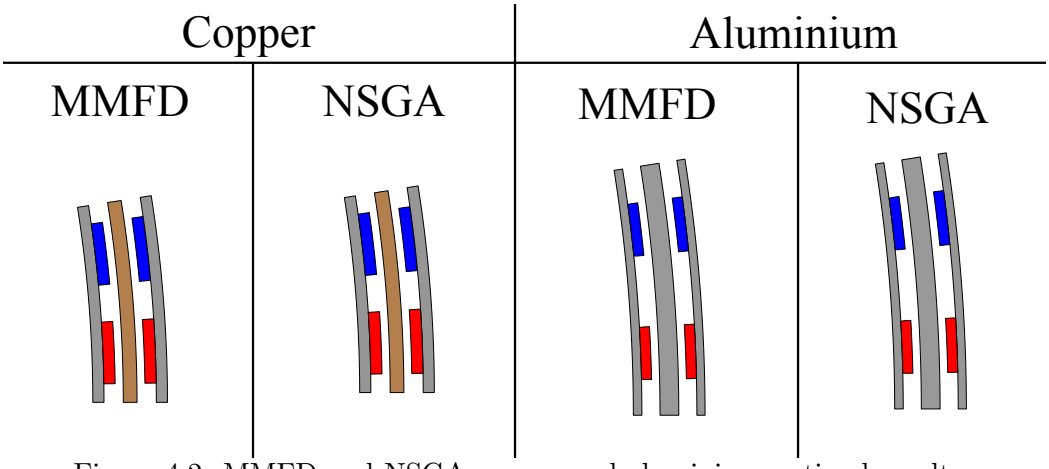

Figure 4.2. MMFD and NSGA copper and aluminium optimal result.

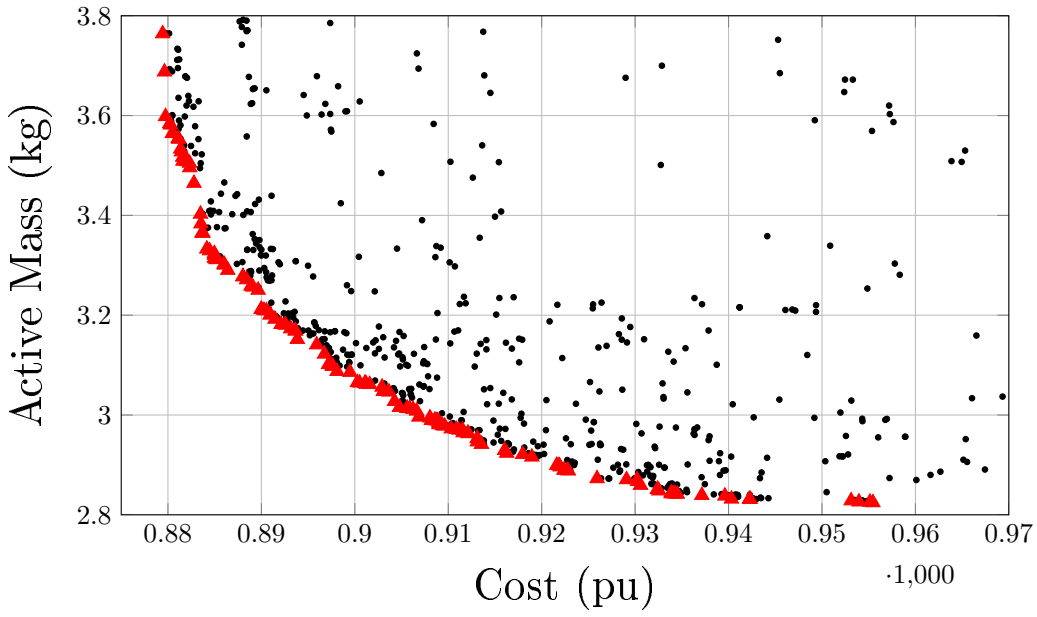

Figure 4.3. NSGA-II pareto front for an eddy current coupler with a copper conductor.

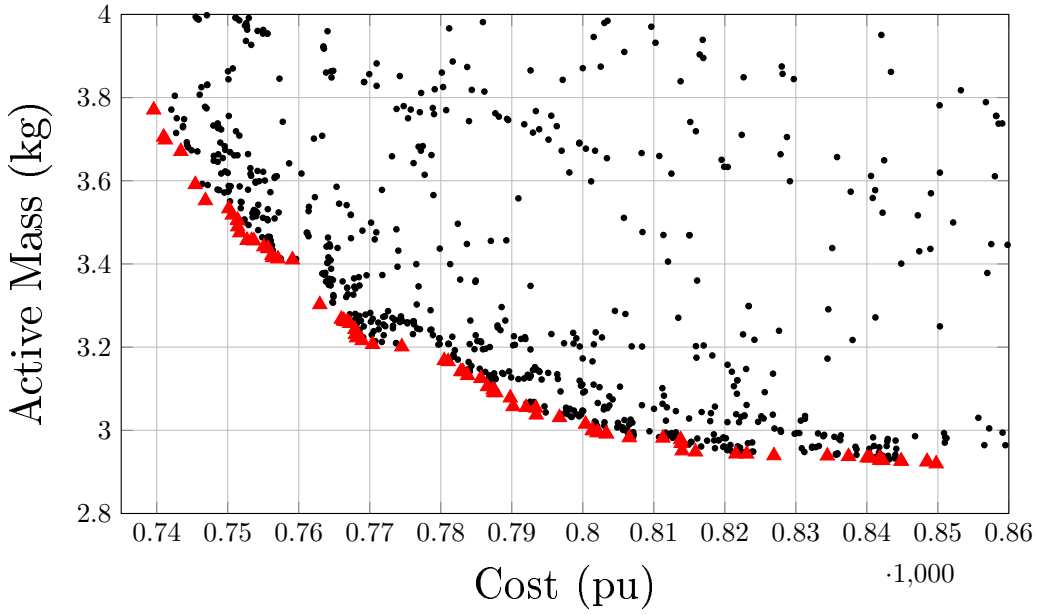

Figure 4.4. NSGA-II pareto front for an eddy current coupler with an aluminium conductor.

4.3.3 Pareto Front Parameter Visualization

The pareto graphs are the output of genetic algorithms in design optimisation. The pareto front guides the designer to make design choices based on where the final output is situated on the pareto curve as shown in Fig. 4.5. The algorithm also decides on an optimum and usually makes a decision based on all the parameters/variables that influence the output. A pareto curve has

various regions and based on the design choices, the designer can choose in what region the design should be.

The pareto graphs are visualised on a simple two dimensional scatter plot but are limited to showing only the outputs of the design algorithm. The effects that the constraints and variables have on the pareto curve are not obvious. There are methods that help with pareto visualisation and one of these methods are interactive decision maps [46]. In this paper a different method of pareto front visualisation is presented with the eddy current coupler used as the basis of this analysis. The colour-gradient pareto curve serves as a way to determine in which way the variables affect the output results of the design algorithm, and where it chooses the optimum. This is done by applying a colour-gradient layer over the pareto curve. This colour-gradient is a distribution map ranging between two colours (in this case from blue to red). Each point on the pareto curve is weighted with a colour based on its numerical value. If all the points are then sorted from smallest to largest a colour-gradient is present on the pareto curve that provides a more direct way to determine the effect of variables on the output. In this study the cost versus active mass pareto curve is considered for the copper eddy current coupler, which were the two optimisation objectives. The pareto curve consists of five regions: two optimum regions, the pareto front, the feasible region and the utopia region, as shown in Fig. 4.5. The pareto curves in Figs. 4.6-4.9 are evaluated with respect to these regions. Within these regions the colour-gradients can take on four different distribution types: the standard, cluster, scatter or frontier distribution.

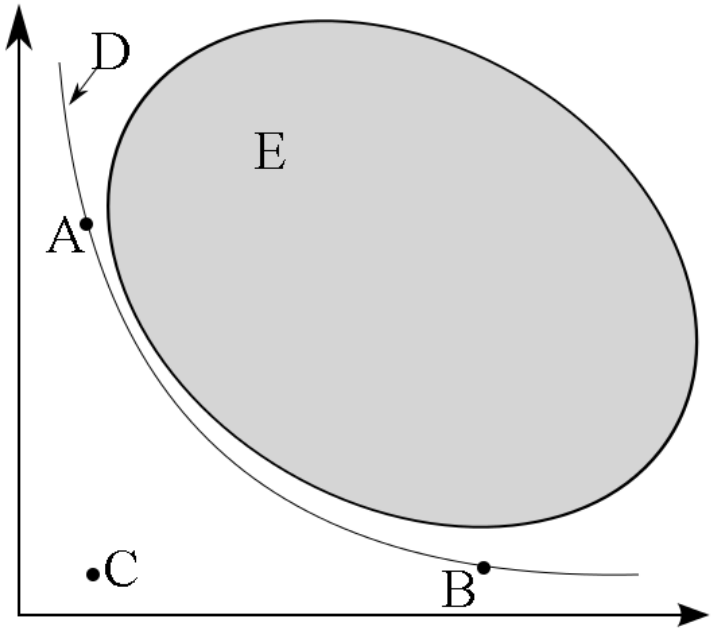

Figure 4.5. The pareto curve. A & B - optimum regions, C - utopia region, D - pareto front and E - feasible region.

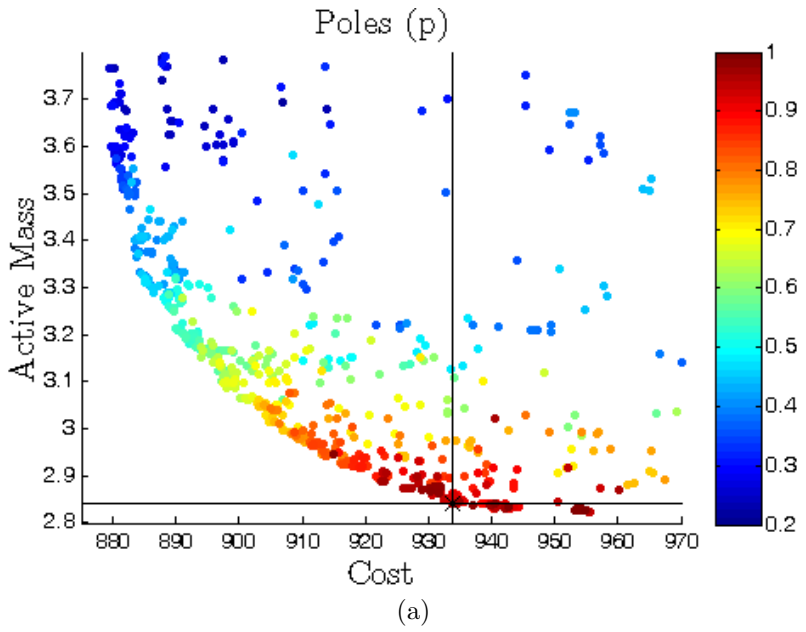

(a)

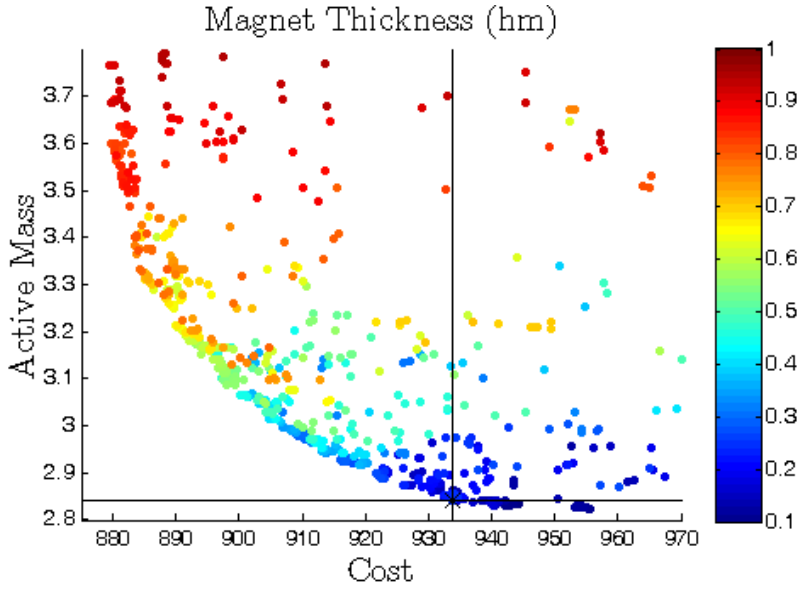

(b)

Figure 4.6. Pareto front colour-gradient distribution (red- maximum; blue-minimum) of the (a) poles and (b) magnet thickness.

The *standard colour-gradient* distribution is shown in Fig. 4.6. This distribution shows a clear and constant colour colour-gradient from the one pareto maximum to the other. The effect of the input variable on such a distribution are usually obvious and understood before running the simulation. Consider the yoke and magnet thickness: it is clear that with an increase in yoke thickness there will be an increase in mass. The same is true for magnet thickness, as it gets thicker the cost increases. Pole numbers also revealed to be a stan-

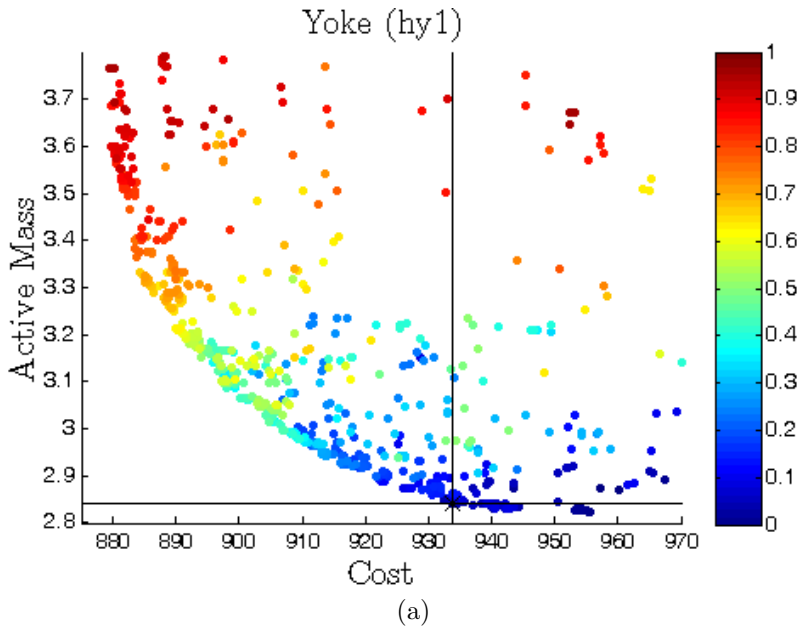

(a)

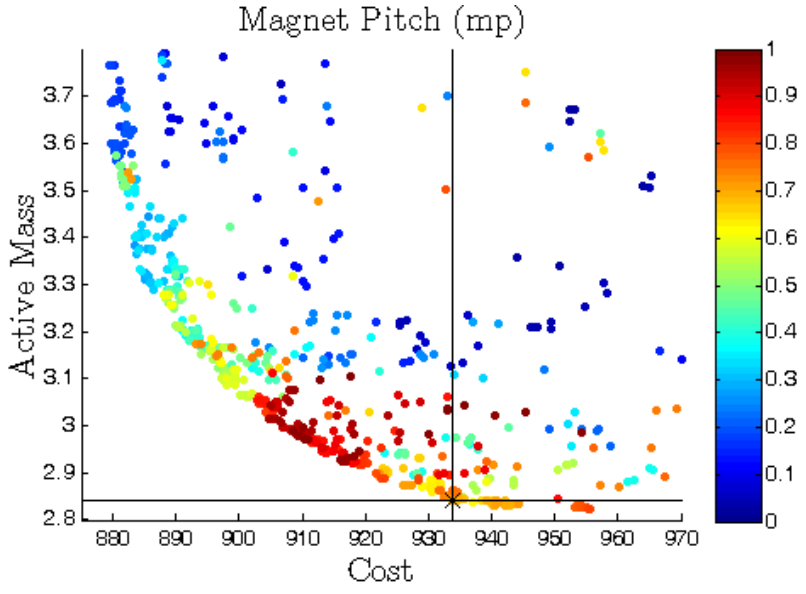

(b)

Figure 4.7. Pareto front colour-gradient distribution (red- maximum; blue-minimum) of the (a) yoke thickness and (b) magnet pitch.

dard distribution and that an increase in pole number results in an increase in cost, but a reduction in mass.

Consider now the magnet pitch and conductor thickness pareto distributions in Fig. 4.7. Both figures show a uniform change in distribution along the pareto frontier region but show distinct maximum/minimum clusters between the two optimum regions. In Fig 4.7 shows that an increase of magnet pitch increases the cost and in Fig 4.7 it shows that with an increase in conductor

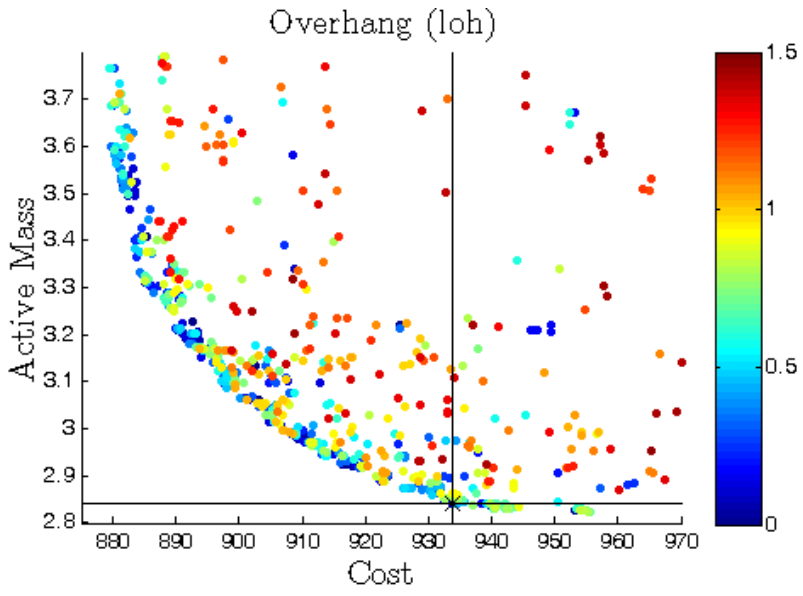

(a)

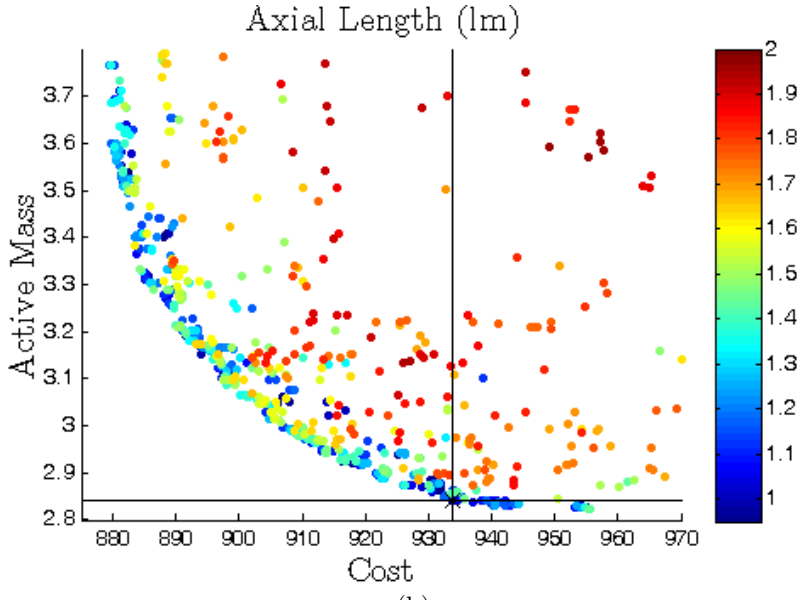

(b)

Figure 4.8. Pareto front colour-gradient distribution (red- maximum; blue-minimum) of the (a)conductor overhang and (b) axial length.

thickness the mass of the coupler also increases. However there are clusters of solutions that are a maximum/minimum, but aren't situated on the optimum regions A and B of Fig. 4.5. These curves are defined as *cluster colour-gradient* pareto curves.

The *frontier colour-gradient* distribution as shown in Figs. 4.8 and 4.9 (a) has a colour-gradient shift from the pareto front region in the direction of the feasible region. The axial length and overhang curves show that the maxi-

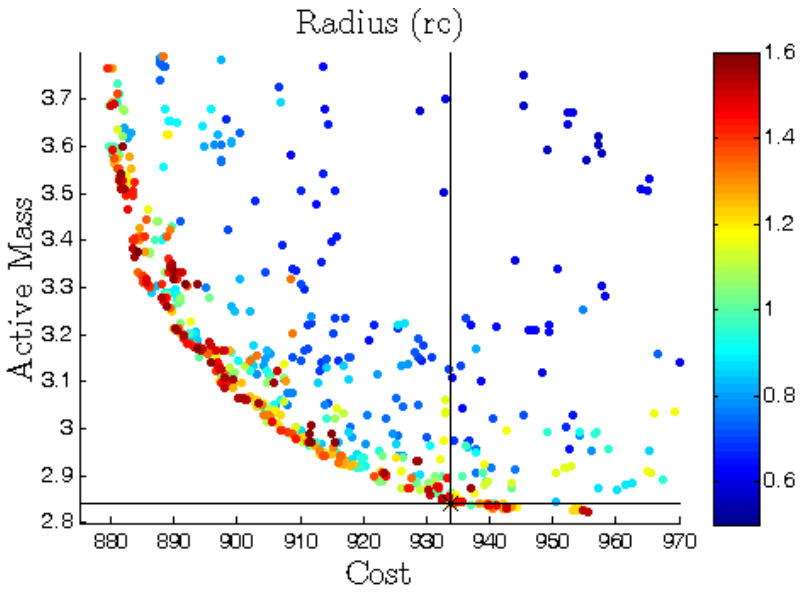

(a)

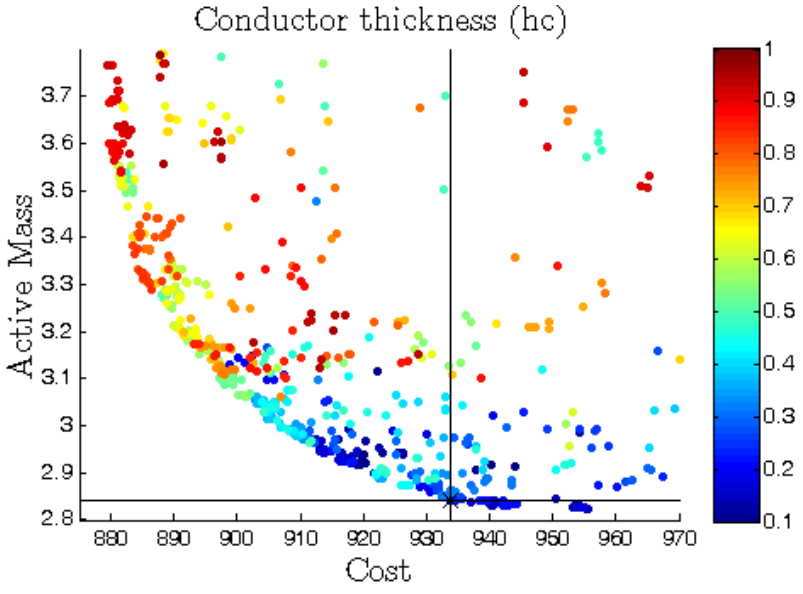

(b)

Figure 4.9. Pareto front colour-gradient distribution (red- maximum; blue-minimum) of the (a) radius and (b) conductor thickness.

mum of these parameters reside in the feasible region whereas the minimums are located on the frontier. This means that any point on the pareto front is considered a minimum for these parameters. This is similar for the conductor radius with the maximum on the frontier. This colour gradient shows that the variables have reached a maximum or a minimum by variation of the variables. This distribution suggests that in a next iteration of the experiment the parameters can be selected as fixed constraints.

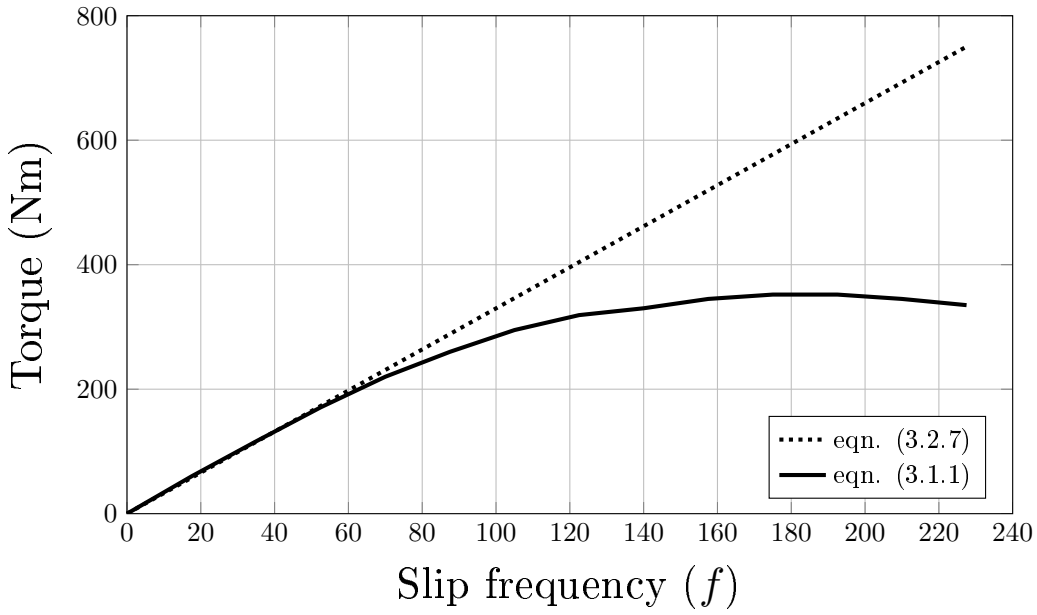

Figure 4.10. CE-FEA and 3D FEA Torque vs Slip Frequency.

The scatter colour-gradient distribution is a combination of a cluster, a frontier and a standard colour-gradient, as shown by the conductor thickness in Fig. 4.9(b). The scatter distribution is difficult to analyse as its effect on the design objectives is very dependent on the other input parameters.

4.3.4 3D FEA result validation

To verify that the optimal result given by the process shown in Fig. 4.1 is a functional and working model, it is necessary to do a 3D transient FEA to ensure an accurate and realistic portrayal of the output torque of the coupling. The eddy current coupling with copper and aluminium as a conductor is tested in this study. The optimal parameters given by the NSGA optimisation are used and the results are shown in Fig 4.10, from this the 3D FEA 3.1.1 is accurate within 3 % of the CE-FEA 3.2.7 torque at low slip frequency. This result also correlates with the results of the previous chapter. However, at higher slip frequencies temperatures affect the performance of the eddy current coupling and a non-linear relationship between torque and slip occurs. As shown in Fig. 4.10 at a slip frequency of over 60 Hz (s = 0.1) the 3D FEA and CE-FEA results begin to diverge.

4.4 Summary

In this chapter the design optimisation of a 2.2 kW, double rotor, radial axis eddy current coupling is described. Using a computationally efficient finite element analysis in conjunction with gradient (MMFD) and population (NSGA) based design optimisation algorithms to obtain an optimal coupling design.

The two optimisation algorithms are evaluated in terms of speed and accuracy. The comparison between copper and aluminium conductor materials revealed that the aluminium is the preferred material in terms of mass and cost. A novel gradient-based colour distribution method with regard to the input parameters of the genetic optimisation algorithm's pareto curve is proposed.

Chapter 5

Final coupler design and construction

After the analysis and design optimisation has been verified, the next step is to build a *functional* eddy current coupler prototype. Designing for manufacture of a prototype is different from the ideal simulated space in electromagnetic FEA software. Real life applications usually involves not only an understanding of how the machine functions but also how the machine is going to provide that function. This requires a more multi disciplinary engineering knowledge, especially from a mechanical engineering perspective.

5.1 Optimal and practical machine

With the knowledge and insight obtained from the results of the previous chapter the design algorithm is run a final time to determine how the built coupler dimensions. Doing a NSGA-II as well as a MMFD, under the variable constraints listed in Table 5.1, the optimal design is given in Table 5.2. The pareto front of the cost and active mass of this design is shown in Fig. 5.1.

Table 5.1. Design constraints

r_c	0.5 - 1.3	l_m	1.1 - 1.5
h_c	0.1 - 1.0	l_{oh}	0.0 - 2.0
h_{y1}	0.1 - 1.0	Poles	0.0 - 1.0
h_{y2}	0.1 - 1.0	Conductor	Aluminium
h_m	0.2 - 1.0	Magnet	NdFeB
θ_p	0.128 - 1.0	Air Gap	1mm

Table 5.2. Optimal design vs practical design

	Optimal	Practical
r_c	129.9 mm	125 mm
h_c	5 mm	5.5 mm
h_{y1}	2.75 mm	4 mm
h_{y2}	2.74 mm	4 mm
h_m	2.8 mm	3.5 mm
θ_p	7.75^o	7.75^o
l_m	57.5 mm	60 mm
l_{oh}	10 mm	10 mm
Poles	32	32

The optimal design is now established but it might not be mechanically feasible to build this optimal machine. Minor changes were made to the machine dimensions to simplify the manufacturing process. The essential part of this design is to keep the torque transfer at the rated efficiency the same as the optimal. The following values were adjusted as follow and are listed in Table 5.1: The diameter of the optimal machine was too large and needed to be a little smaller. The new value was chosen to be 125 mm instead of 129 mm. These were made thicker due to mechanical structure concerns; to ensure that the magnets do not pull the yokes toward each other resulting in displacement. The magnets were made thicker due to concerns that they will break when glued onto the yokes. Magnets are known to be brittle and with these strong attraction forces they can shatter if not handled carefully. The axial length was adjusted to compensate for the slight drop in torque due to the diameter decrease.

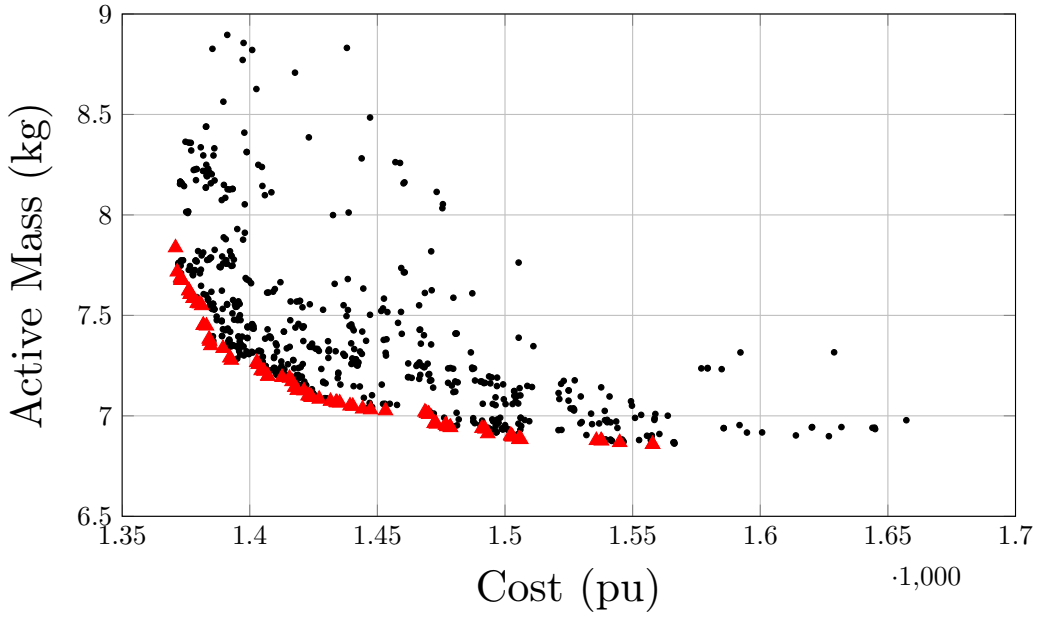

Figure 5.1. Pareto curve of the optimal design.

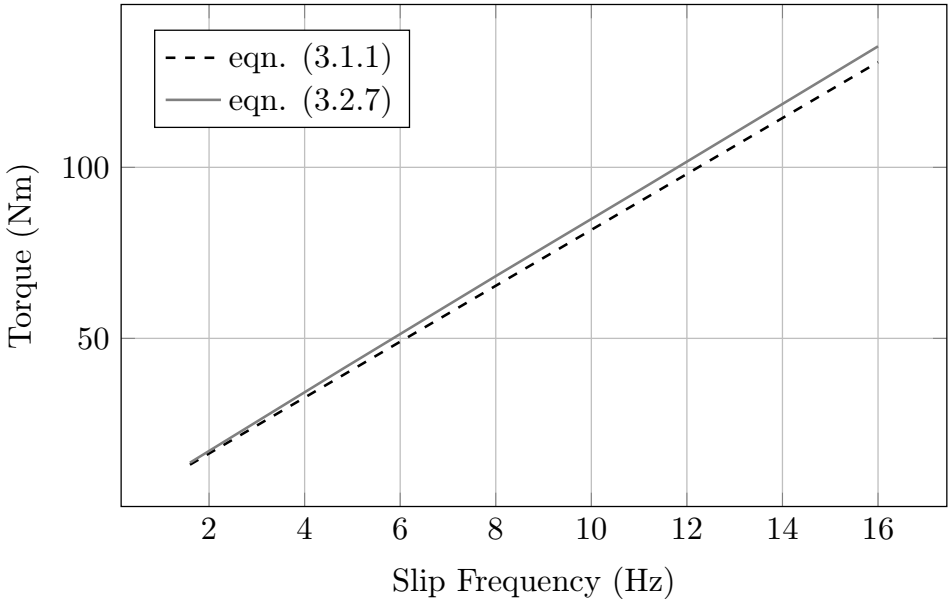

Figure 5.2. 3D CE-FEA results of the optimal and practical coupler.

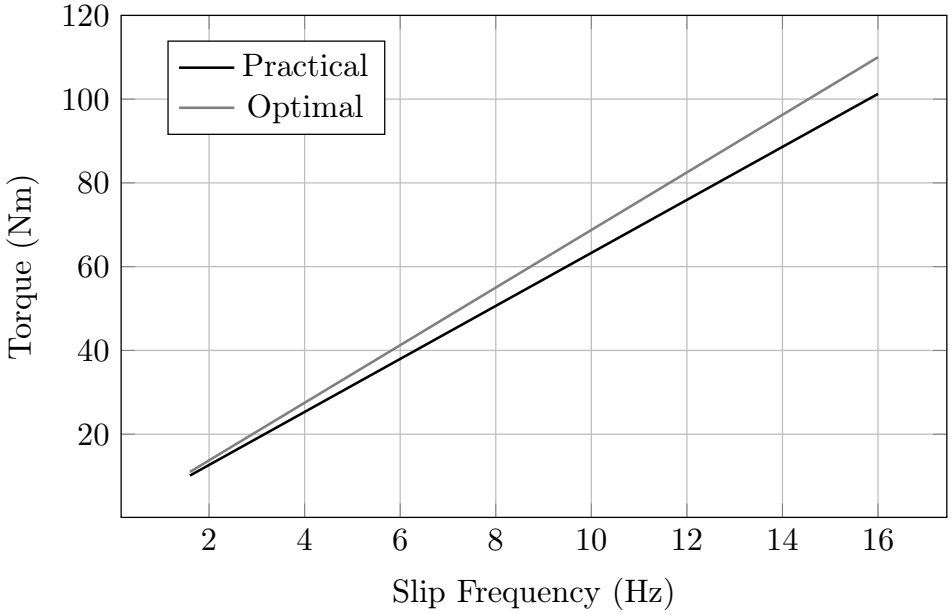

Figure 5.3. 3D CE-FEA results of the optimal and practical coupler.

To verify that the adjusted model still meets the torque and efficiency requirements, the optimal and practical designs are compared and shown in Table 5.2. Finally, the practical design is verified against a 3D FEA simulation and shown in Fig. 5.3 to verify that the whole process is correct.

5.2 Coupler manufacturing

Now that the final design has been decided upon, it is drawn in CAD software and shown in Fig. 5.4 and the built model in Fig. 5.5 . This section covers the design considerations made during the manufacturing process. Detailed sketches and photos are shown in Appendix A.

5.2.1 Permanent magnet rotor

The PM rotor consists of two primary components, the NdFeB magnets and the iron yoke. The secondary components include the backplate and the fasteners and are shown in Fig. 5.6.

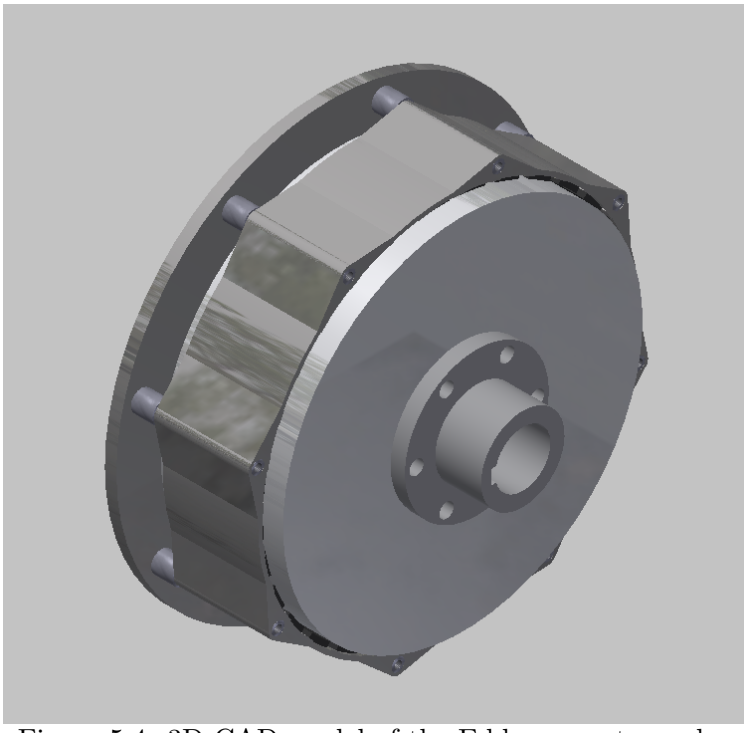

Figure 5.4. 3D CAD model of the Eddy current coupler

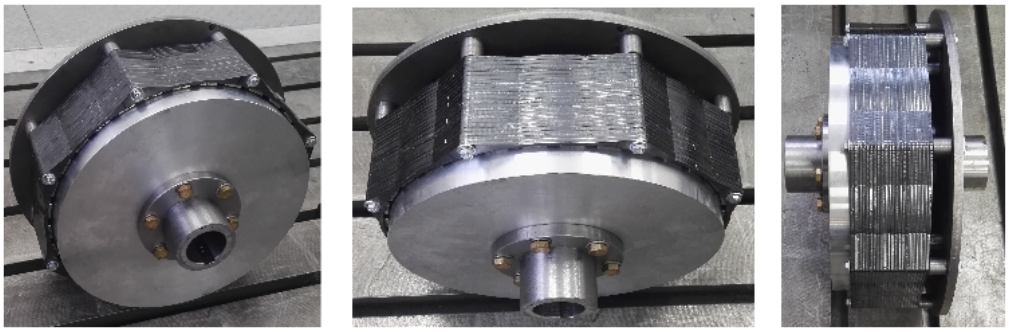

Figure 5.5. Built eddy current coupler prototype.

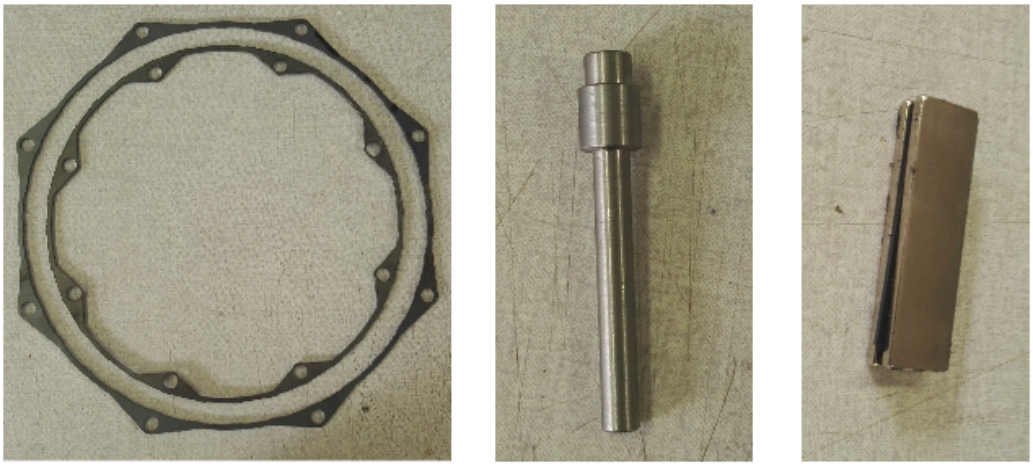

Figure 5.6. Yoke laminations, support peg and NdFeB magnet.

Due to the large attraction forces it is necessary to ensure that the yokes are thick enough so that the magnets don't warp them. It is known that the structural integrity of a cylinder would likely be sufficient, but it is good practice to verify. Using Autodesk Inventor, a rudimentary strength test is implemented and it shows no significant deflection of the yokes.

Magnets are to be glued onto the yokes but to keep them from moving due to attraction forces, the yokes are designed with guides cut into the steel. Although these guides are useful for assembly, it creates problems for yoke construction. The yokes need to be either Computer Numeric Control (CNC) machined as a solid conductor component or needs to be laser cut lamination parts. The machining process wasn't considered cost effective and steel laminations were used. They are stacked onto support pegs as shown in Fig. 5.7.

After the laminations are stacked the magnets are glued on using epoxy glue

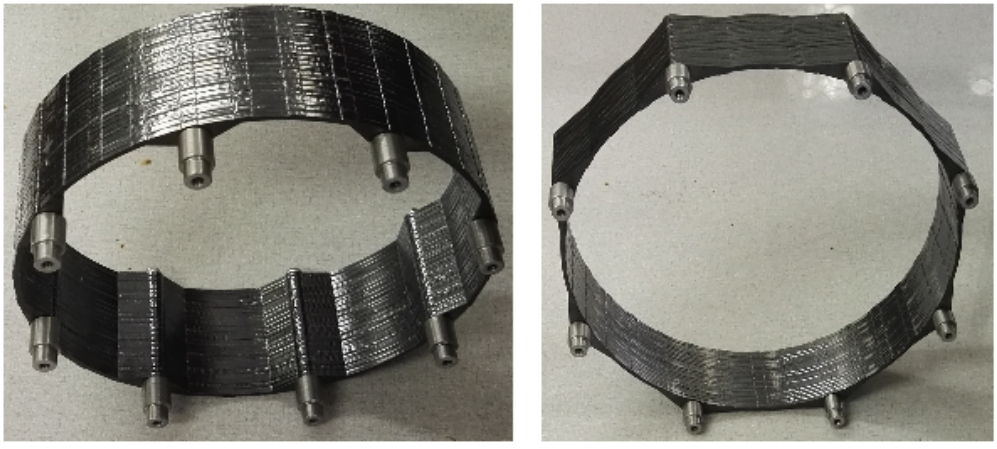

Figure 5.7. Yoke laminations stacked onto support pegs.

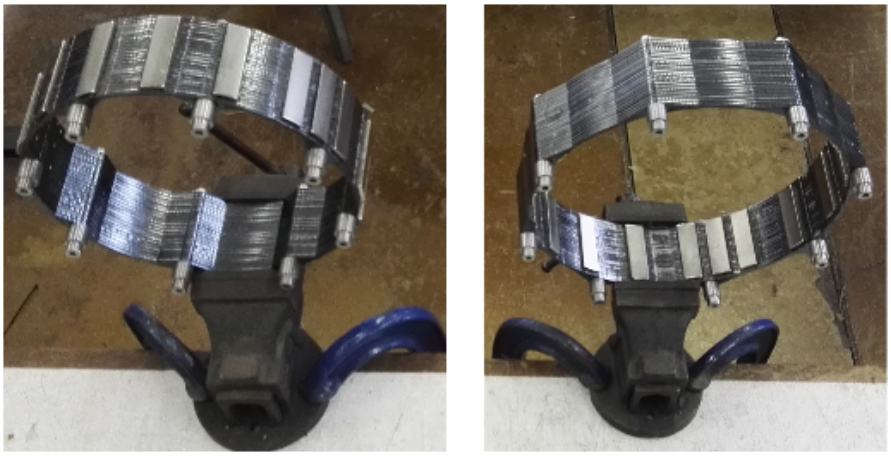

Figure 5.8. Yoke laminations with magnets being glued on.

with a high temperature operation capability. All the north-south magnets are glued first, and then the south-north as shown in Fig. 5.8. Once both yokes have all the magnets mounted, they are then bolted onto the backplate.

5.2.2 Conductor rotor

The conductor rotor is easily constructed from machining out the shape from a block of aluminium and is shown in Fig. 5.9. Other methods of conductor manufacturing were considered, but machining was the most cost effective for prototyping. When manufacturing on a large scale, impact extrusion or casting might be better options to consider.

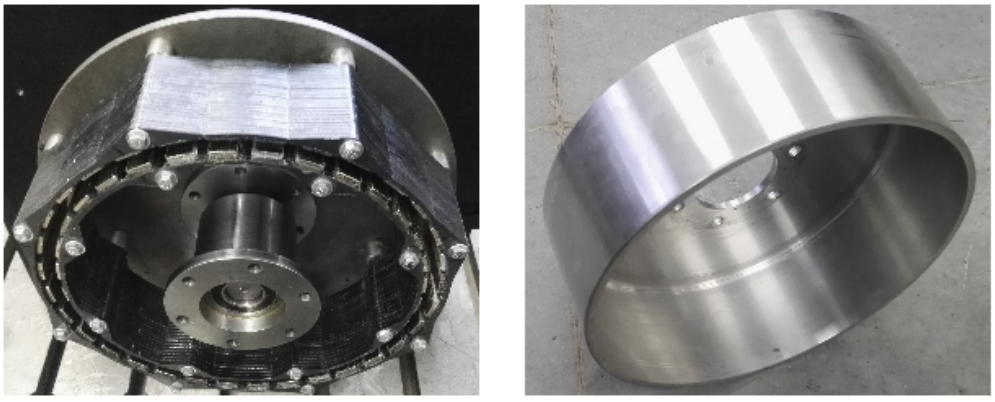

Figure 5.9. Built eddy current coupler prototype.

5.2.3 Alignment bearing

Although the coupler disconnects two mechanical systems a bearing is necessary to align the conductor and the PM rotor. All the torque is still transferred by the magnets and conductor and none through the alignment bearing connection. Fig. 5.9 shows the bearing fitted to the PM rotor as well as the conductor before it is fitted onto the bearing. The final assembly of all the components of the slip coupler is shown in Fig. 5.5.

5.3 Summary

This chapter shows the manufacturing and assembly of the eddy current coupler from an optimal design tested in the laboratory. The optimal machine dimensions were slightly adjusted to simplify manufacturing and assembly to ensure the structural integrity of the coupler. There weren't any complications during the manufacturing of the coupler and the practical dimensions are the same as that of the built one.

Chapter 6

Practical verification of design

With all the parts manufactured and the coupler assembled, it is fixed onto a test bench. Measurements are taken to observe how it compares with the results of the design optimisation results. Two primary tests are executed: a torque vs speed measurement as well as a temperature measurement.

6.1 Torque tests

As shown in Chapter 3 and 4, the analysis and design is focused on the evaluation of the torque with respect to the slip frequency. The measurements are compared to 3.1.1 and 3.2.7 and shown in Fig. 6.1.

The results in Fig 6.1 show that the coupler doesn't perform as well as the

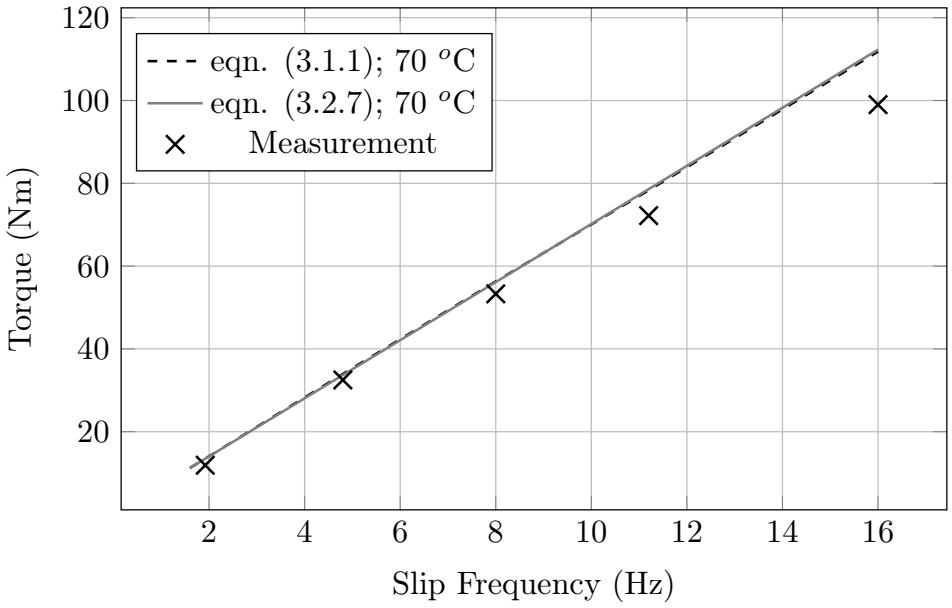

Figure 6.1. Torque and slip frequency of 3.1.1 and 3.2.7 at 70 ^{o}C compared to measured results of coupler.

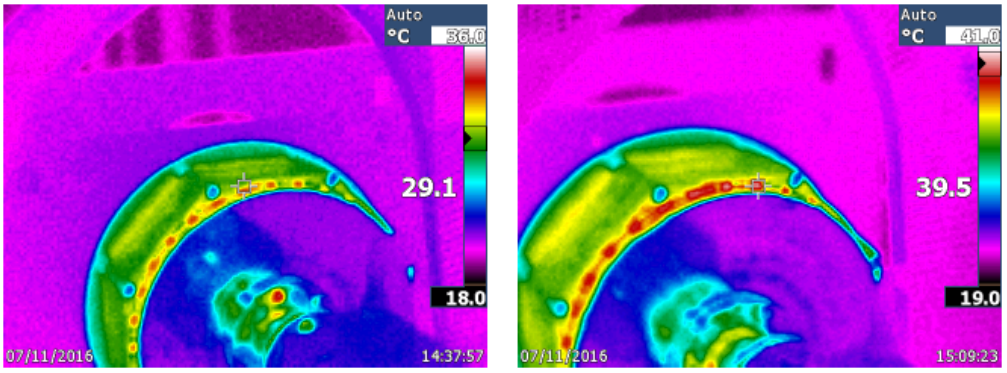

Figure 6.2. Temperature Measurements.

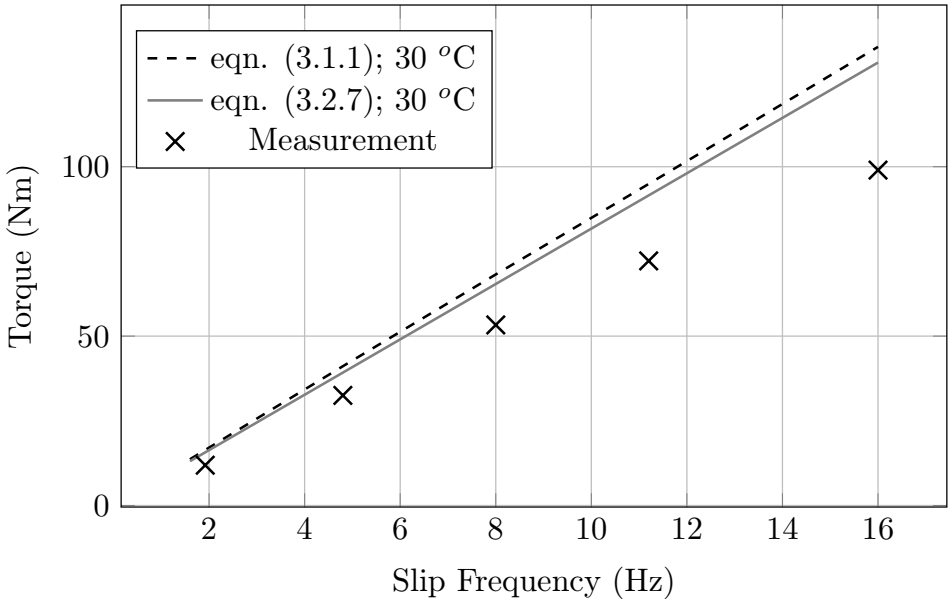

Figure 6.3. Torque and slip frequency of (3.1.1) and (3.2.7) at 30 ^{o}C compared to measured results of coupler.

FEA (3.1.1) and (3.2.7) results predict. Although the error between them are small, the important thing to note is the temperature difference. During the coupler tests a temperature measurement showed to be ± 30 ^{o}C as shown in Fig. 6.2. If the FEA (3.1.1) and (3.2.7) are adjusted to 30 ^{o}C, the error between the built coupler and the simulated result is very high as shown in Fig. 6.3.

Further investigation into the conductor material revealed why the machine was under-performing. Due to supply, the aluminium grade used was lower than the grade used in the simulation. The aluminium that was used had more alloys which made it stronger, but it increased the electrical resistivity of the conductor. This was due to a communication error during manufacturing. The new electrical resistivity values were adjusted in the FEA of (3.1.1) and

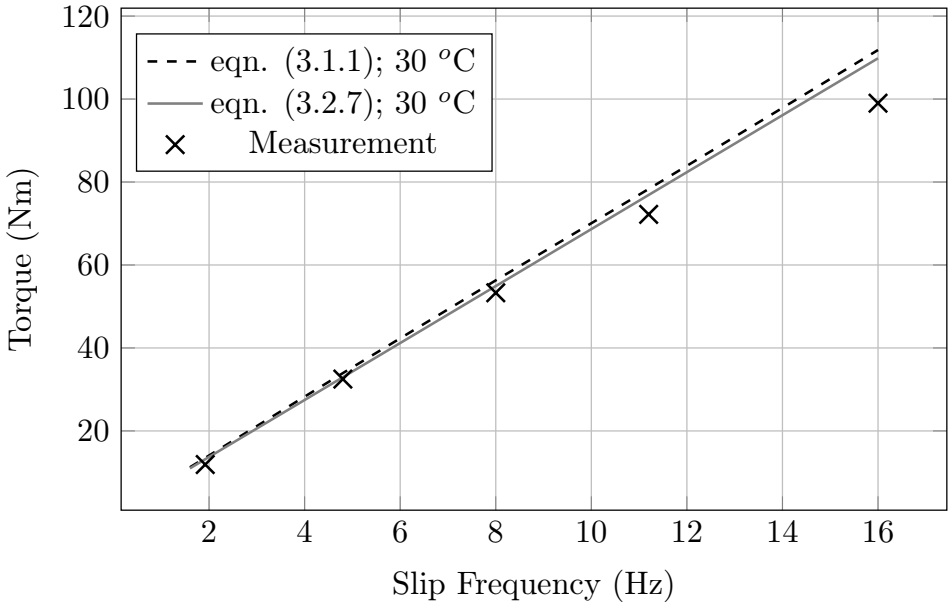

Figure 6.4. Torque and slip frequency of (3.1.1) and (3.2.7) at 30 ^{o}C with lower aluminium grade compared to measured results of coupler.

(3.2.7) and the results are shown in Fig. 6.4. This shows a significant decrease of the error between the simulation and the measurements. The difference in electrical resistivity caused the poor performance of the coupler and will be significantly better if the conductor is of a higher grade.

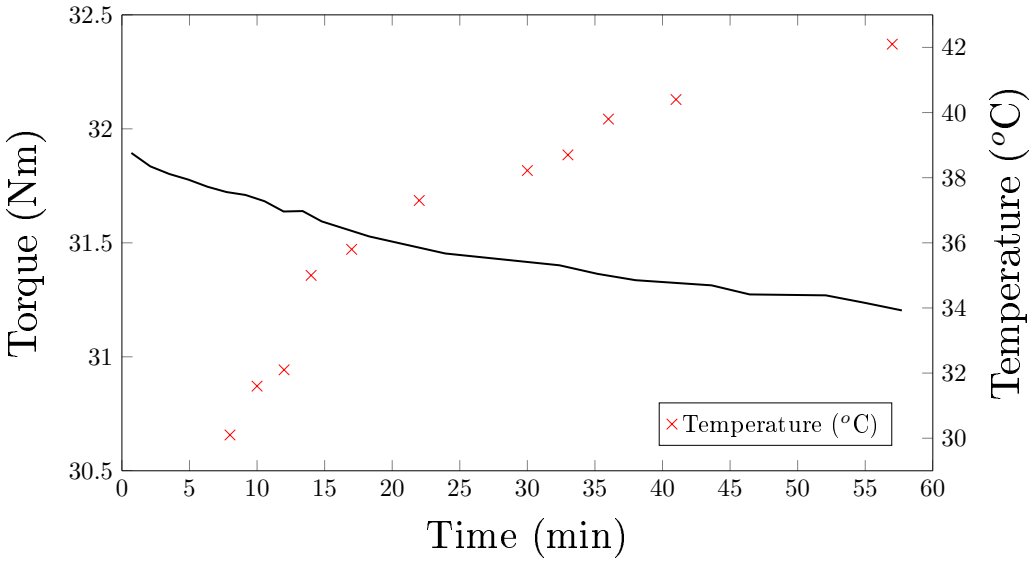

Figure 6.5. 60 minute measurement of the coupler torque (black) and temperature (red) at a fixed speed.

6.2 Temperature tests

The temperature was initially measured to be 30 ^{o}C as shown in Fig. 6.2. Due to the continuous functionality of the coupler, it is necessary to take a temperature measurement for a longer time period to see how well the coupler retains heat. A torque measurement of 60 minutes was taken to observe the decline of torque transfer as the temperature increased, and is shown in Fig. 6.5. The change in temperature has an effect on the coupler performance, and the torque saturates with the temperature at 31 Nm and 42 ^{o}C respectively.

Chapter 7

Eddy current coupler case studies

In this chapter two case studies of an eddy current coupler is investigated. The first study is on the analysis of a single PM rotor eddy current coupler for a wind turbine yaw damper. The second is a brief comparison of two similar slip couplers, their drawbacks and advantages.

7.1 Design of a single PM rotor yaw damper

This case study is part of a larger study by CJJ Labuschagne in [47], where the damper was built and tested. The analytical design and design optimisation is compiled in this section as a verification of the analytical design process from Chapter 3 and the optimisation from Chapter 4, on other eddy current coupler topologies.

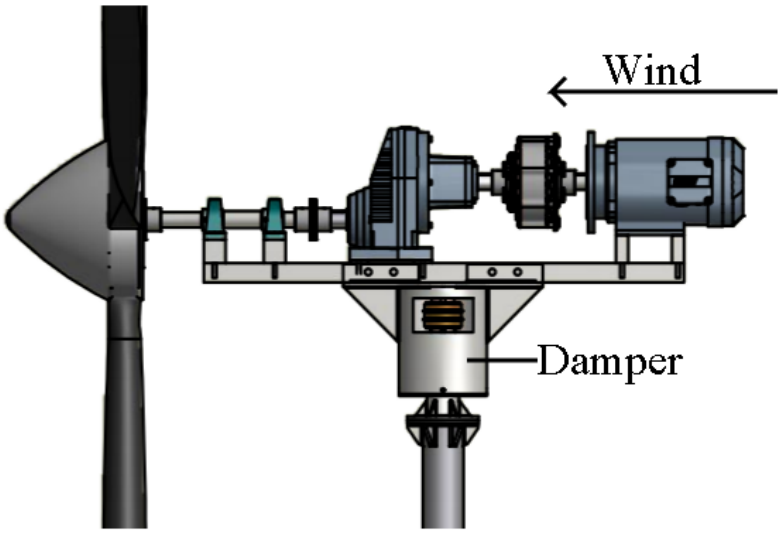

Figure 7.1. 2.2 kW downwind turbine drive train.

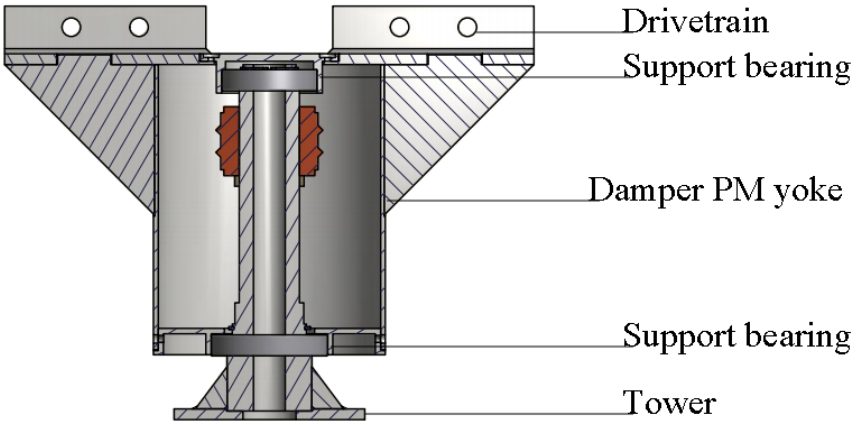

Figure 7.2. Yaw damper housing between drivetrain and tower.

The damper in this case is used to dampen the yaw movement of a small scale (2.2 kW) downwind turbine system as shown in Fig. 7.1. The turbine blades rotate when wind blows from the tail side instead of the nose side as in upwind turbines. There is no pitch control on the blades and the nacelle doesn't have a tail for alignment and support. The turbine system is thus vulnerable to yaw movement from gusts and sudden changes in wind direction. The yaw damper is fitted between the drivetrain and tower as shown in Fig. 7.2.

The damper is a single sided radial axis eddy current coupler as shown in Fig. 7.3. It consists of two yokes; one with a conductor and the other with permanent magnets. The modelling and torque calculation of the damper is similar to that of the double sided eddy current coupler but instead of a second pair of magnets, the conductor is attached to a yoke. This yoke is connected to the tower and the PM yoke is part of the wind turbine drivetrain. The flux from the magnets travel through the conductor, inducing eddy currents

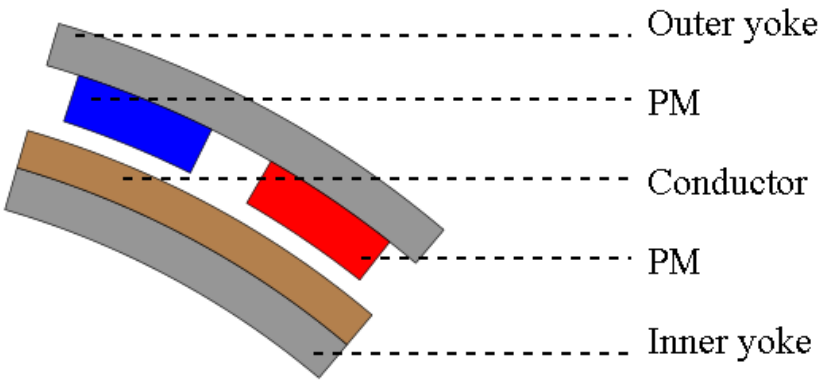

Figure 7.3. 2D model of the yaw damper.

Table 7.1. Eddy current damper dimensions

Outer diameter	105.5 mm
Magnet thickness	5 mm
Outer yoke thickness	4 mm
Inner yoke thickness	4 mm
Magnet pitch	8.18^o
Poles	30
Stack length	100 mm
Overhang	10 mm
Air gap	2 mm

in the conductor and the yoke. This results in a damping effect that is dependent on the speed of the yaw movement, ensuring a more stable yaw movement.

The same method of torque calculation discussed in Chapter 3 is used in this case. The conductor is divided into radial layers where the flux density is taken from the 2D FEA result, each layer undergoes a Fourier transformation and used in 3.2.5 and 3.2.6. However, this method doesn't account for the eddy currents and subsequent torque developed in the iron of the conductor yoke. This was regarded as a negligible amount and wasn't added to the torque calculation.

In Chapter 4 gradient and population based design optimisation methods were utilised to find an optimal coupler design. The gradient based method was the fastest and was used in this case to find the optimal damper parameters. The constraints and output results from the design process is shown in Table 7.1. The significant constraint was the outer diameter, in order for the damper to be able to fit inside a standard pipe diameter.

The damper is modelled in a 3D FEA package to verify the analytical results;

Figure 7.4. Outer PM and inner conductor yokes of the eddy current yaw damper.

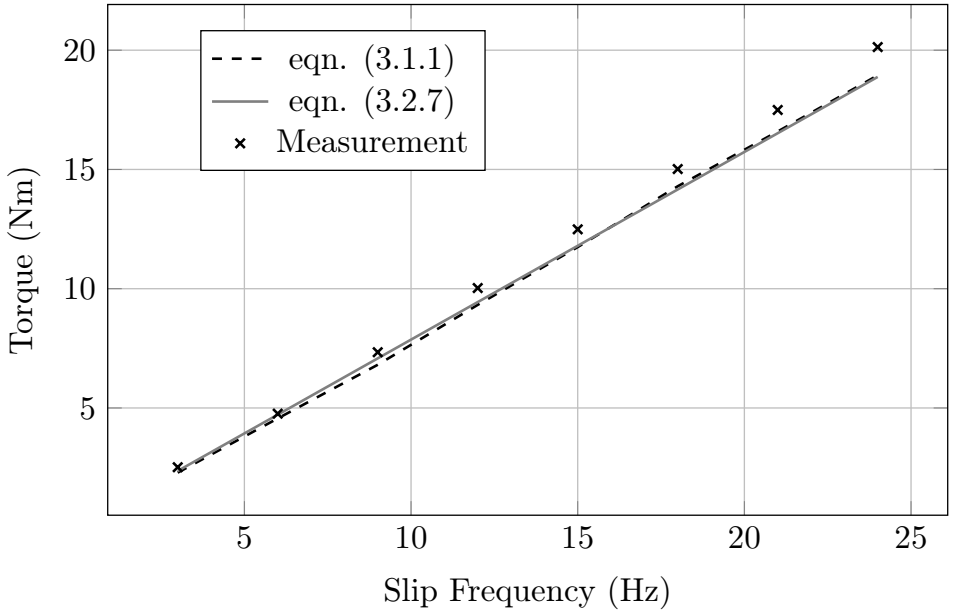

Figure 7.5. FEA 3.1.1, 3.2.7 and measured results of the yaw damper.

to see if the iron part of the yoke has a significant effect on the output torque and shown in Fig. 7.5. Torque measurements of the built damper and simulation results are shown in Fig. 7.5. The lab measurements and simulation results match with a small error margin. Showing that the design procedure works for single sided topologies as well. The built damper is shown in Fig. 7.4.

To conclude, a single sided radial axis eddy current damper was designed based on a method used to design double sided radial axis eddy current couplers. This method was used together with a design optimisation algorithm to find the optimal design to be built. Eddy currents in the yoke weren't taken into account in this process, and shows that it didn't have a significant effect on the output at such low slip speeds. The built coupler practical measurement values matches the simulated results.

7.2 A brief comparison between magnetic slip couplers

In Chapter 1 alternative slip coupler types are discussed and one of them is the Slip Permanent Magnet Coupler (SPMC) or multiphase coupler. This is a novel type coupler and it would be interesting to see how it compares to the eddy current coupler. In this section various aspects like design, manufacturing and performance of these two couplers are investigated, measured and compared. This is to provide deeper insight into the different attributes of these couplers.

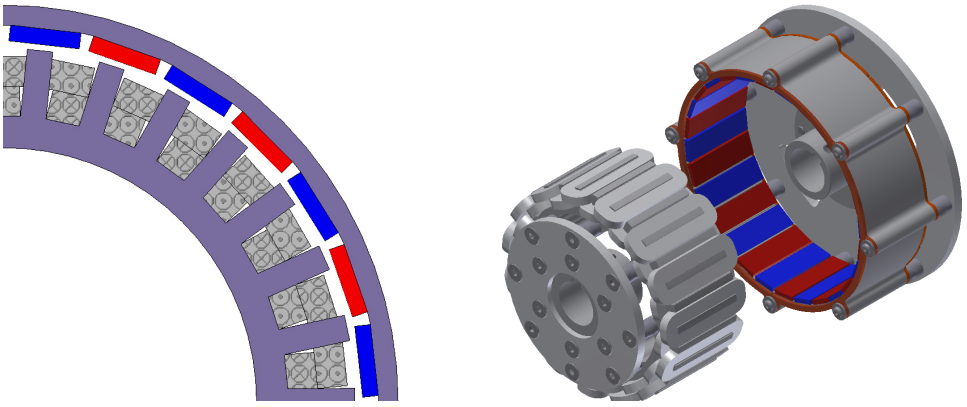

Cross section model. 3D model.

Figure 7.6. Radial axis slip permanent magnet torque coupler.

7.2.1 Design

The slip coupler of [9] follows a similar design process as the one in Chapter 3. Using a single static 2D FEA to obtain a torque result to be used in an optimisation environment. The modelling and design of this coupler is also computationally efficient and produces an accurate result. The SPMC is also a radial axis coupler and also utilises permanent magnets and a conductor material. The crucial design difference is that the SPMC has a single sided PM topology and it doesn't have a solid conductor but consists of short circuited coils on a spoke rotor, given in Fig. 7.6.

The design specifications of the SPMC are similar to that of the eddy current coupler specifications in Chapter 4. The most important of those are shown in Table 7.2, together with the design parameters of both couplers. From this table there are the following design drawbacks:
- The ECC is bigger in diameter than the SPMC.
- The ECC requires more magnet material.
- The SPMC is lighter in active mass.

7.2.2 Manufacturing

The SPMC is more difficult to manufacture with regards to the parts and assembling them. Due to the yoke containing a lot of steel near the air gap,

Table 7.2. Design parameters of the eddy current damper

	SPMC	ECC
Outer diameter	210 mm	276 mm
Axial length	65 mm	60 mm
Active mass	7 kg	8.66 kg
Magnet mass	1 kg	1.3 kg
Total mass	17 kg	17 kg

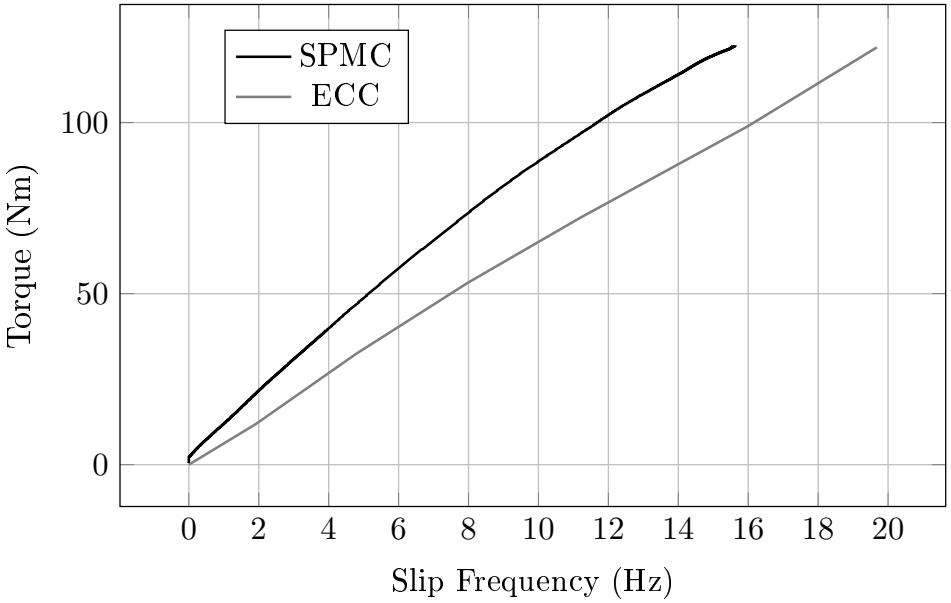

Figure 7.7. Measured results of the SPMC and the ECC.

the magnets on the outer rotor attract the inner rotor making it difficult to fit together. The short circuit windings on the inner yoke are difficult to assemble and to manufacture a good fill factor. Custom coils need to be made in order for maximum efficiency of the coupler and that increases the cost.

The eddy current coupler is a lot less difficult to assemble since one of the rotors is just made from conductor material, it isn't attracted by the PM rotor. However, assembling the double layer magnet rotor is a challenge because of the attraction forces between the yokes. This is still easier than the SPMC because the air gap is bigger.

7.2.3 Performance

With both couplers manufactured, assembled and tested, the performance of the couplers can be evaluated and compared. Two comparison tests are done similar to those of chapter 6, a torque test and a temperature test.

The torque at slip frequency of both couplers are measured and shown in Fig. 7.7. At first glance it is clear that the SPMC performes much better than the ECC. This is due to a low grade conductor used in the ECC (as noted in the previous chapter) and the performance will be better if the conductor rotor is changed. For low slip frequencies both couplers have a linear torque to slip frequency performance. However, at higher slip frequencies the ECC graph remains linear but the SPMC starts saturating and decreasing.

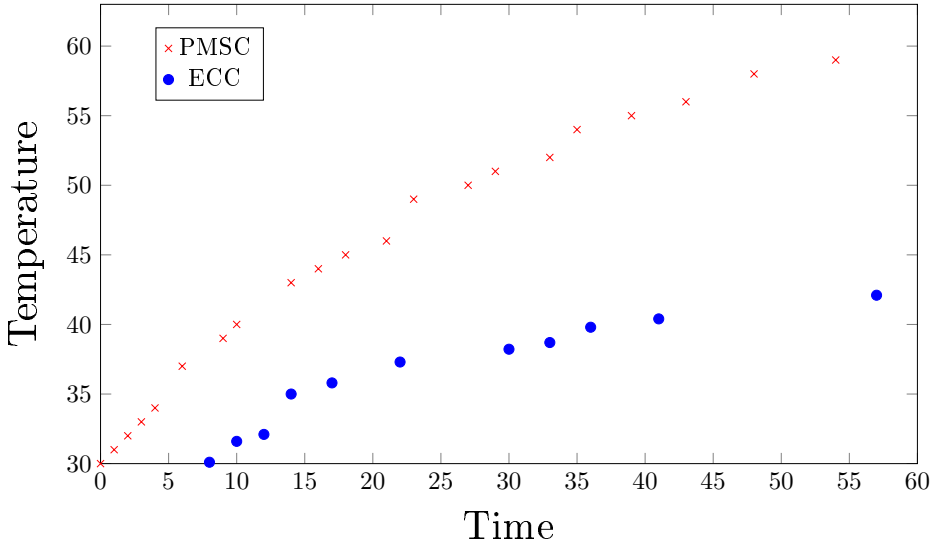

Figure 7.8. Temperature over a 60 minute sample period of the ECC (blue) and SPMC (red).

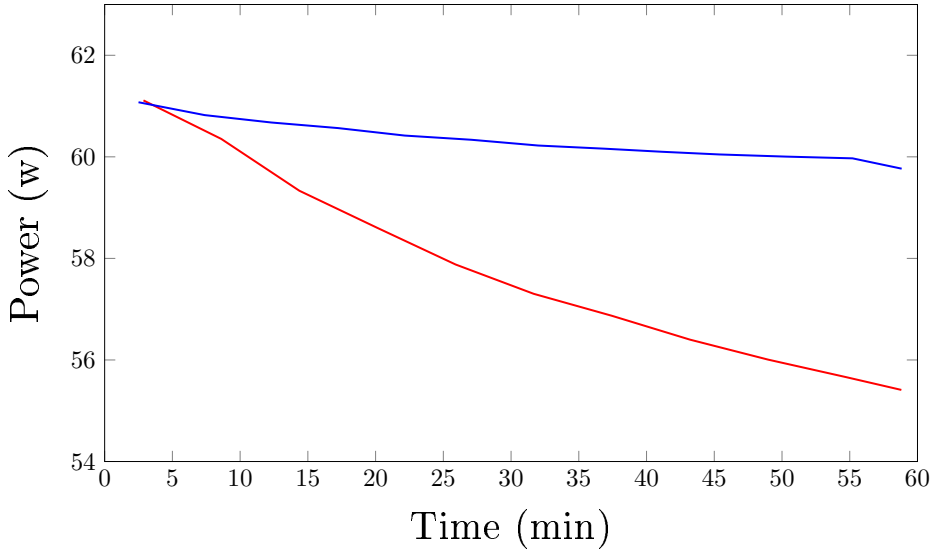

Figure 7.9. Power over a 60 minute sample period of the ECC (blue) and SPMC (red).

The second test is a 60 minute temperature measurement and shown in Fig. 7.8. The graph shows that the SPMC has a much higher operating temperature than the ECC that increase at a faster rate. Fig. 7.9 graph also shows the power loss of the coupler as the temperature increases.

To conclude, the comparison between the SPMC and the ECC yields interesting results. From a design perspective the SPMC looks to be a preferable choice due to its size and magnet weight, but manufacturing of the ECC is much easier. The torque-frequency performance of the SPMC was better than that of the ECC, but it wasn't able to maintain that performance at high slip

frequencies. The ECC also had a lower temperature and not as much losses as the SPMC.

At this stage it isn't possible to say which design is better for wind turbine applications, but it does show where both couplers can be improved. However, the ECC is a much better choice for protection due to its ability to transfer higher torque loads.

Chapter 8

Conclusion and recommendations

The work contained in this thesis document the process of finding an alternative method of designing radial axis eddy current couplers for use in wind drivetrains.

- The method includes the modelling of the coupler and using a hybrid 2D analytical/FEA method to determine the torque developed in the coupler. This method was evaluated under various dimension extremities to determine how rigorous and robust the method is when implemented with the design optimisation algorithms. Comparing the results with a transient 2D FEA, it proved to be a fast and accurate method calculate the torque.

- The 2D analytical method was combined with Russell's end effect factor to calculate the 3D torque, this is the 3D computationally efficient FEA (3D CE-FEA). The accuracy of the Russell factor hasn't been previously investigated in literature especially not for radial axis eddy current couplers. The results show that the end effect factor is an accurate way to obtain a 3D result from the 2D analytical FEA. However, when $\beta = l_{pm}/d_c$ is below 0.2 the 3D CE-FEA doesn't provide the correct torque and this method isn't suitable for pancake type couplers.

- The proposed CE-FEA method derived in Chapter 2 has been found to be accurate in obtaining a torque solution in conjunction with the design optimisation algorithms for the eddy current coupler. The performance of the optimised designs are validated with a commercial 3D FEA package.

- The CE-FEA was successfully implemented in a design optimisation environment and could be used to find optimal coupler parameters.

- Using the gradient based MMFD is significantly faster than the population

based NSGA-II in obtaining a optimal design solution. It takes the MMFD only 4% of the time the NSGA take to obtain an solution. However, the MMFD does require more guidance from the designer.

- For 2.2 kW applications (35 Nm torque), copper eddy current couplers are smaller and cheaper than the aluminium ones for more or less the same active mass. The copper coupler also uses 13 % less magnet material than aluminium couplers.

- A colour gradient method is proposed for the visualisation of genetic algorithm pareto front curves. This enables the designer to visualise what the effect of input variables are on the design objectives.

- A radial axis eddy current coupler is manufactured and assembled from the output dimensions of the design optimisation. The coupler performance was lower than that of the 3D FEA simulation results. This was due to a lower grade coupler that was used as the conductor material. Adjusting the simulations according to the conductor specifications yields accurate results.

- The same method was used in a case study to design a single sided radial axis eddy current yaw damper. The results from this case study revealed that an accurate single sided coupler can be designed using the same process as with the double sided coupler. The effects of the yoke eddy currents did not have an effect on the torque in this case.

- A permanent magnet slip coupler was briefly compared to the eddy current coupler. These couplers are to be used in the same applications. At first the SPMC had better torque-slip performance than the eddy current coupler. However, after both couplers operated at rated conditions for 60 minutes the SPMC performance decreased much more than the eddy current coupler. The ECC was able to distribute the heat better and faster and operated at a lower temperature than the SPMC.

8.1 Recommendations and future work

The following recommendations are presented based on the research findings:
- More laboratory tests should be conducted on both the eddy current coupler and the SPMC in terms of dynamic response and filter characteristics. This would verify if the couplers are able to filter out high frequencies.

- A thorough design optimisation should be conducted on the SPMC multiphase coupler to see if it is the optimal design. This optimal design can be

compared to an optimal ECC design for a comprehensive comparison.

- Conducting a FE thermal and structural analysis will provide insight into the minimum yoke and conductor sizes and can subsequently decrease the size or mass of the coupler.

- In this study the focus was mainly on small couplers and it would be beneficial to test this design procedure on larger couplers in the range of 120 Nm - 1500 Nm.

- The mechanical design of a variable speed eddy current coupler can be beneficial for systems that require the soft start of motors in a system. A variable speed coupler's conductor has the ability to move closer and further away from the magnetic flux sources.

- The use of Alnico permanent magnets in the design optimisation process instead NdFeB could lead to a more cost effective coupler.

Appendices

Appendix A

CAD Drawings

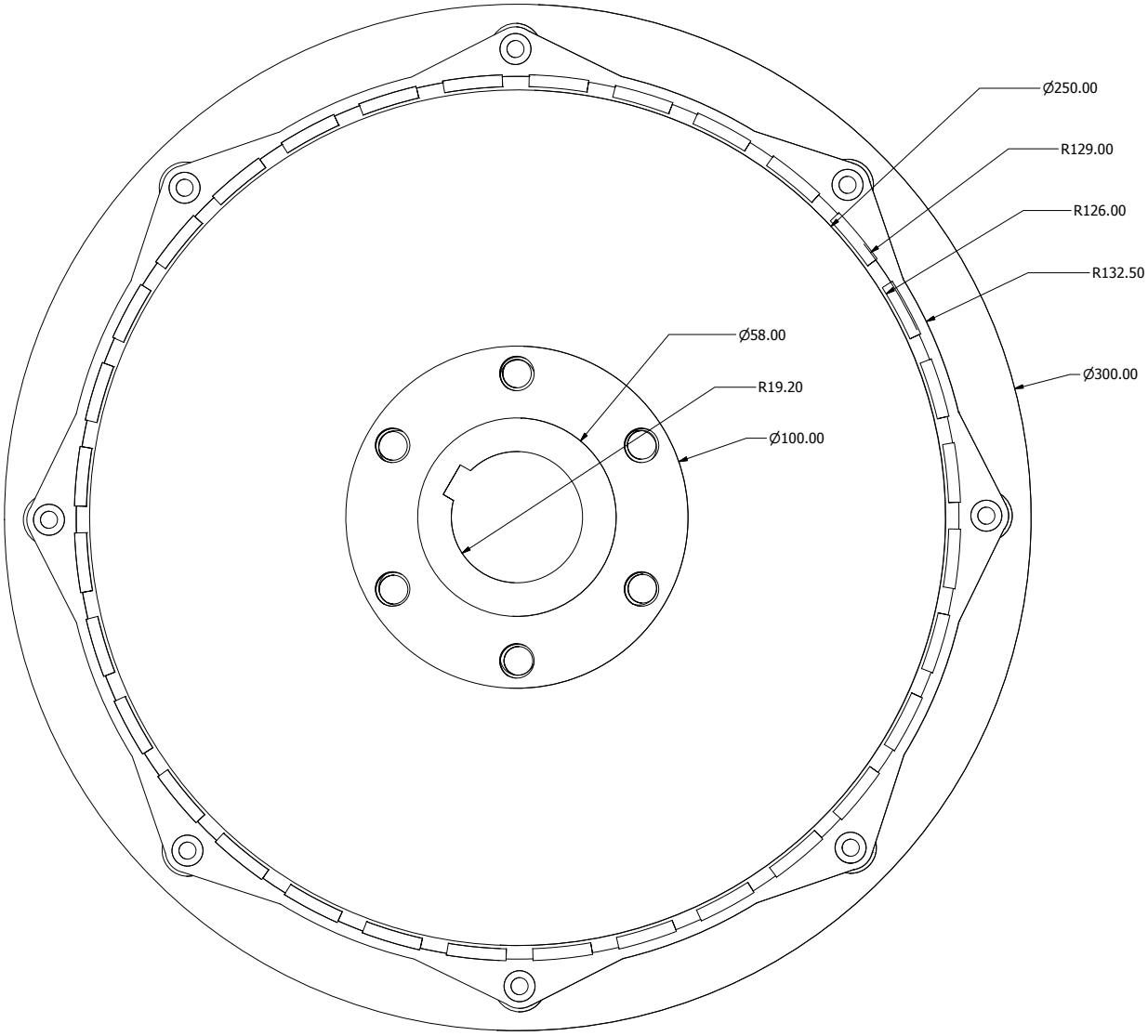

DRAWN Stephan Erasmus	2016/11/28	
CHECKED		TITLE: Double PM-rotor Radial Axis Eddy cuurent coupler
QA		
MFG		
APPROVED		
SIZE C	DWG NO	REV
SCALE	SHEET 1 OF 3	

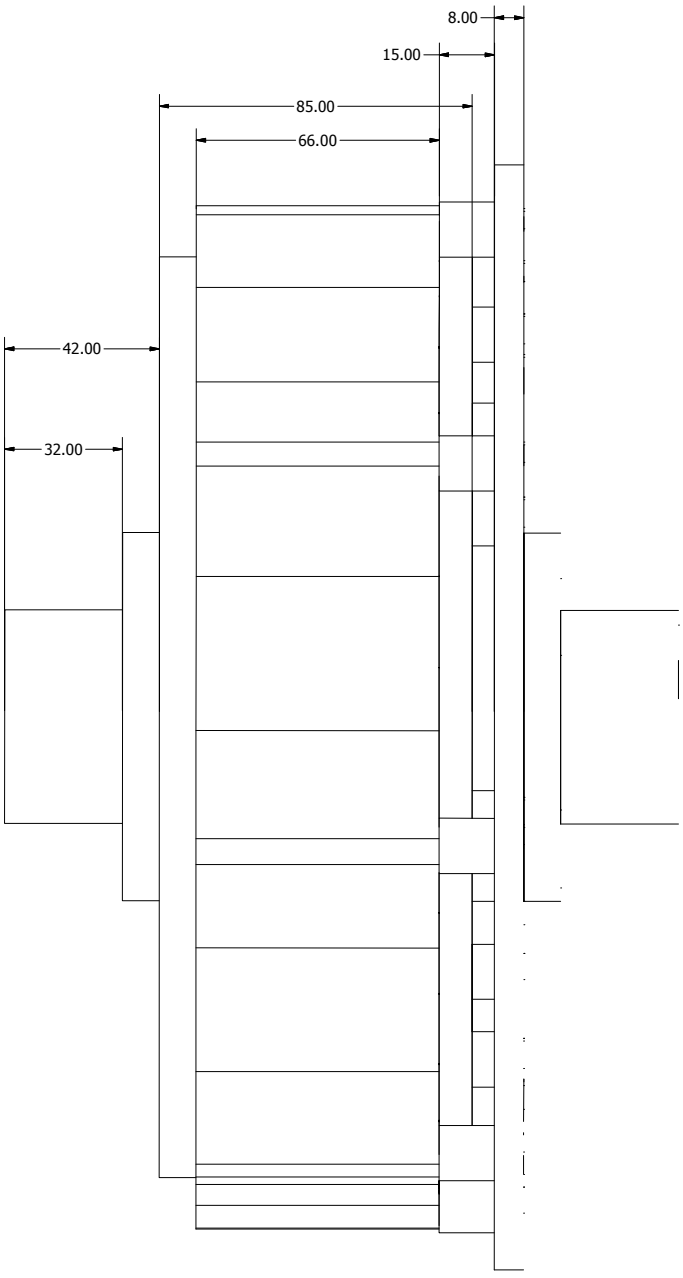

DRAWN Stephan Erasmus	2016/11/28	
CHECKED		TITLE
QA		Double PM-rotor Radial Axis Eddy cuurent coupler
MFG		
APPROVED		SIZE C / DWG NO / REV
		SCALE / SHEET 2 OF 3

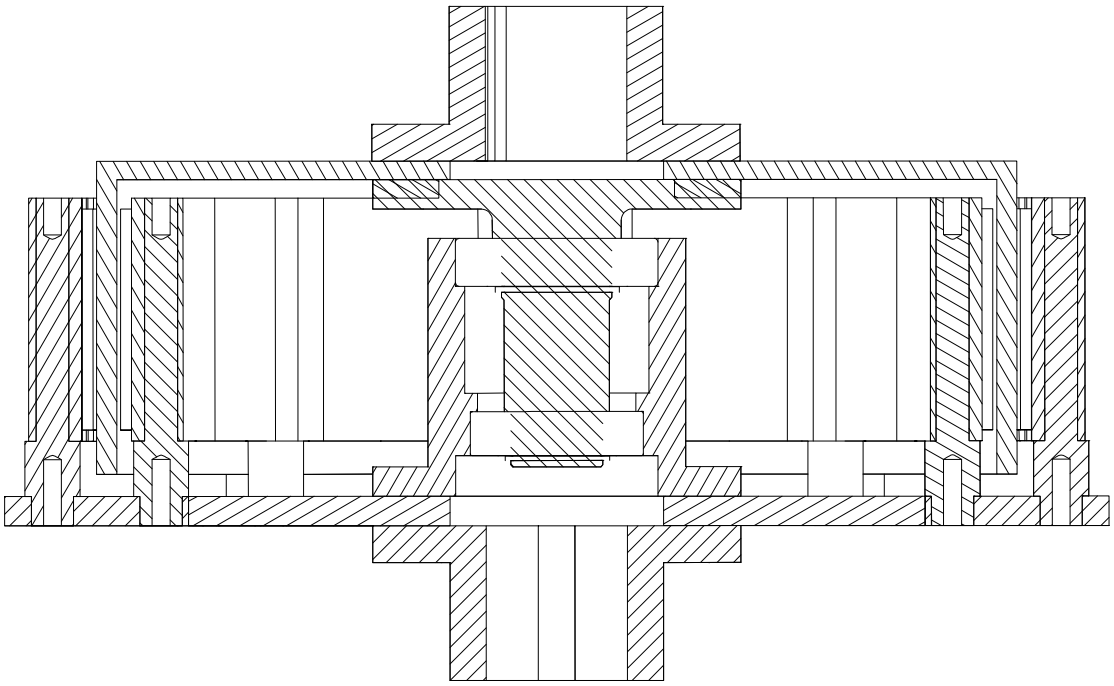

SECTION B-B
SCALE 1 : 1

DRAWN Stephan Erasmus	2016/11/28		
CHECKED		TITLE	
QA		Double PM-rotor Radial Axis Eddy cuurent coupler	
MFG			
APPROVED		SIZE C	DWG NO / REV
		SCALE	SHEET 3 OF 3

Bibliography

[1] Mohammadi, S. and Vaez-Zadeh, s.: Analytical Modeling and Analysis of Axial-Flux Interior Permanent-Magnet Couplers. *IEEE Transactions on Industrial Electronics*, vol. 61, no. 11, pp. 5940–5947, 2014.

[2] Mouton, Z. and Kamper, M.J.: Design of an eddy-current coupling for slip-synchronous permanent magnet wind generators. *Proceedings - 2012 20th International Conference on Electrical Machines, ICEM 2012*, pp. 633–639, 2012.

[3] Nagrial, M.H., Rizk, J. and Hellany, A.: Design of Synchronous Torque Couplers. *World Academy of Science, Engineering and Technology*, vol. 5, no. 7, pp. 426–431, 2011. ISSN 2010376X.

[4] Potgieter, J. and Kamper, M.: Optimum design and comparison of slip permanent magnet couplings with wind energy as case-study application. *IEEE Transactions on Industry Applications*, vol. 50, no. 5, pp. 3223–3234, 2014.
Available at: `http://ieeexplore.ieee.org/xpls/abs_all.jsp?arnumber=6739123`

[5] Hornreich, R. and Shtrikman, S.: Optimal design of synchronous torque couplers. *IEEE Transactions on Magnetics*, vol. 14, no. 5, pp. 800–802, 1978.

[6] Report, A.C.: Bibliography of Electric Couplings. *Power Apparatus and Systems, Part III. Transactions of the American Institute of Electrical Engineers*, vol. 72, no. January, pp. 202–203, 1953.

[7] Lubin, T., Mezani, S. and Rezzoug, A.: Simple analytical expressions for the force and torque of axial magnetic couplings. *IEEE Transactions on Energy Conversion*, vol. 27, no. 2, pp. 536–546, 2012. ISSN 08858969.

[8] Ravaud, R., Lemarquand, V. and Lemarquand, G.: Analytical design of permanent magnet radial couplings. *IEEE Transactions on Magnetics*, vol. 46, no. 11, pp. 3860–3865, 2010. ISSN 00189464.

[9] van Wyk, P.J. and Kamper, M.J.: Simplified analysis of nonoverlap short-circuited coil winding slip permanent magnet couplers. *IEEE Transactions on Industry Applications*, vol. 52, no. 6, 2016.

[10] Davies, E.: General theory of eddy-current couplings and brakes. *Proceedings of the Institution of Electrical Engineers*, vol. 113, no. 5, p. 825, 1966. ISSN 00203270.

[11] Gulec, M. and Aydin, M.: Modelling and analysis of a new axial flux permanent magnet biased eddy current brake. In: *2016 XXII International Conference on Electrical Machines (ICEM)*, pp. 459–465. Sept 2016.

[12] Potgieter, J. and Kamper, M.: Design of New Concept Direct Grid-Connected Wind Generator. *IEEE Transactions on Industry Appliccations*, vol. 48, no. 3, pp. 913–922, 2012.

[13] Ockuis, D., Erasmus, A.S. and J, K.M.: Small-Scale Geared Turbine System with Slip-Synchronous Technologys. *WindAC Africa*, 2016.

[14] Mohammadi, S., Mirsalim, M., Vaez-Zadeh, S. and Talebi, H.A.: Design analysis of a new axial-flux interior permanent-magnet coupler. *PEDSTC 2014 - 5th Annual International Power Electronics, Drive Systems and Technologies Conference*, , no. Pedstc, pp. 562–567, 2014.

[15] Dai, X., Liang, Q., Cao, J., Long, Y., Mo, J. and Wang, S.: Analytical Modeling of Axial-Flux Permanent Magnet Eddy Current Couplings With a Slotted Conductor Topology. vol. 52, no. 2, 2016.

[16] Lubin, T. and Rezzoug, A.: Steady-State and transient performance of axial-field eddy-current coupling. *IEEE Transactions on Industry Appliccations*, vol. 62, no. 4, pp. 2287–2296, 2015.
Available at: `http://eprints.aston.ac.uk/8191/`

[17] Canova, A. and Vusini, B.: Design of axial eddy-current couplers. *IEEE Transactions on Industry Applications*, vol. 39, no. 3, pp. 725–733, 2003. ISSN 00939994.

[18] Mohammadi, S. and Mirsalim, M.: Design optimization of double-sided permanent-magnet radial-flux eddy-current couplers. *Electric Power Systems Research*, vol. 108, pp. 282–292, 2014. ISSN 03787796.
Available at: `http://dx.doi.org/10.1016/j.epsr.2013.11.014`

[19] MagnaDriveCorporation.: Water/waste water-screw pump.

[20] Kamper, M.J., Potgieter, J.H.J., Stegmann, J.A. and Bouwer, P.: Comparison of air-cored and iron-cored non-overlap winding radial flux permanent magnet direct drive wind generators. *IEEE Energy Conversion Congress and Exposition: Energy Conversion Innovation for a Clean Energy Future, ECCE 2011, Proceedings*, pp. 1620–1627, 2011.

[21] Lesobre, A., Ahmedl, A.H.B. and Drecq, D.: An analytical dynamic model of eddy-current brakes. *IEMDC 2001 - IEEE International Electric Machines and Drives Conference*, pp. 122–125, 2001.

[22] Choi, J.Y., Shin, H.J., Park, Y.S. and Jang, S.M.: Torque analysis of axial flux PM type eddy current brake based on analytical field computations. *2011 International Conference on Electrical Machines and Systems, ICEMS 2011*, , no. I, 2011.

[23] Dai, X., Cao, J., Long, Y., Liang, Q., Mo, J. and Wang, S.: Analytical Modeling of an Eddy-current Adjustable-speed Coupling System with a Three-segment Halbach Magnet Array. *Electric Power Components and Systems*, vol. 43, no. 17, pp. 1891–1901, 2015. ISSN 1532-5008.
Available at: `http://www.tandfonline.com/doi/full/10.1080/15325008.2015.1070934`

[24] Fu, W.N. and Chen, Y.: A Convenient Algorithm for Circuit Parameters of Eddy-Current Field Based on Circuit-Field Coupling Formulation.

[25] Canova, A. and Vusini, B.: Analytical modeling of rotating eddy-current couplers. *IEEE Transactions on Magnetics*, vol. 41, no. 1 I, pp. 24–35, 2005. ISSN 00189464.

[26] Canova, A. and Vusini, B.: Analytical Modeling and Analysis of Axial-Flux Interior Permanent-magnet Couplings. *IEEE Transactions on Magnetics*, vol. 61, no. 11, pp. 5940–5947, 2014. ISSN 0278-0046.

[27] Wang, J., Lin, H., Fang, S. and Huang, Y.: A general analytical model of permanent magnet eddy current couplings. *IEEE Transactions on Magnetics*, vol. 50, no. 1, 2014. ISSN 00189464.

[28] Deb, N.S. and Kalyanmoy: Multi objective optimization using nondominated sorting in genetic algorithms. *Journal of Evolutionary Computing*, vol. 2, no. 3, pp. 221–248, 1994. ISSN 1098-6596. `arXiv:1011.1669v3`.

[29] Canova, a., Freschi, F., Gruosso, G. and Vusini, B.: Genetic optimisation of radial eddy current couplings. *COMPEL: The International Journal for Computation and Mathematics in Electrical and Electronic Engineering*, vol. 24, no. 3, pp. 767–783, 2005. ISSN 0332-1649.
Available at: `http://www.emeraldinsight.com/10.1108/03321640510598120`

[30] Canova, a., Freschi, F., Repetto, M. and Vusini, V.: Eddy Current Coupler Optimization. *Second International Conference on Power Electronics, Machines and Drives (PEMD 2004)*, vol. 1, pp. 436–441, 2004. ISSN 05379989.

[31] Sizov, G.Y., Zhang, P., Ionel, D.M., Demerdash, N.A.O. and Rosu, M.: Automated multi-objective design optimization of PM AC machines using computationally efficient FEA and differential evolution. *IEEE Transactions on Industry Applications*, vol. 49, no. 5, pp. 2086–2096, 2013. ISSN 00939994.

[32] Duan, Y. and Ionel, D.M.: A review of recent developments in electrical machine design optimization methods with a permanent-magnet synchronous motor benchmark study. *IEEE Transactions on Industry Applications*, vol. 49, no. 3, pp. 1268–1275, 2011. ISSN 00939994.

[33] Vanderplaats, G.: A robust feasible directions algorithm for design synthesis. *24th Structures, Structural Dynamics and Materials Conference. Lake Tahoe,NV,U.S.A.*., 1983.

[34] Tonoli, A.: Dynamic characteristics of eddy current dampers and couplers. *Journal of Sound and Vibration*, vol. 301, no. 3-5, pp. 576–591, 2007. ISSN 10958568.

[35] Mohammadi, S. and Mirsalim, M.: Nonlinear Modeling of Eddy-Current Couplers. *IEEE Transactions on energy conversion*, vol. 29, no. 1, pp. 224–231, 2014.

[36] Mohammadi, S. and Mirsalim, M.: Double-sided permanent-magnet radial-flux eddycurrent couplers: three-dimensional analytical modelling, static and transient study, and sensitivity analysis. *IET Electric Power Applications*, vol. 7, no. 9, pp. 665–679, November 2013. ISSN 1751-8660.

[37] Russell, R. and Norsworthy, K.: Eddy currents and wall losses in screened-rotor induction motors. *Proceedings of the IEE Part A: Power Engineering*, vol. 105, no. 20, p. 163, 1958. ISSN 03698882.

[38] Edwards, J.D., Jayawant, B.V., Dawson, W.R.C. and Wright, D.T.: Permanent-magnet Linear Eddy-current Brake with a Non-magnetic Reaction Plate. *IEEE Proc-Electr. Power Appl*, vol. c, 1999. ISSN 13502352.
Available at: `http://sro.sussex.ac.uk/22637/`

[39] Yamazaki, K.: Modification of 2D Nonlinear Time-Stepping Analysis by Limited 3D Analysis for Induction Machines. *IEEE Transactions on Industry Appliccations*, vol. 33, no. 2, pp. 1694–1697, 1997.

[40] Yamazaki, K., Kanou, Y., Fukushima, Y., Ohki, S., Nezu, A., Ikemi, T. and Mizokami, R.: Reduction of magnet eddy-current loss in interior permanent-magnet motors with concentrated windings. *IEEE Transactions on Industry Applications*, vol. 46, no. 6, pp. 2434–2441, 2010. ISSN 00939994.

[41] Erasmus, A.S. and Kamper, M.J.: Analysis for design optimisation of double pm-rotor radial flux eddy current couplers. In: *2015 IEEE Energy Conversion Congress and Exposition (ECCE)*, pp. 6503–6510. Sept 2015. ISSN 2329-3721.

[42] Lombaard, C. and Kamper, M.J.: Theoretical and finite element analysis of a double rotor radial flux permanent magnet eddy current coupling. In: *South African Power and Energy Conference*. 2015.

[43] Deb, K., Pratap, A., Agarwal, S. and Meyarivan, T.: A fast and elitist multiobjective genetic algorithm: NSGA-II. *IEEE Transactions on Evolutionary Computation*, vol. 6, no. 2, pp. 182–197, 2002. ISSN 1089778X.

[44] Stegmann, J.A. and Kamper, M.J.: Design aspects of double-sided rotor radial flux air-cored permanent-magnet wind generator. *IEEE Transactions on Industry Applications*, vol. 47, no. 2, pp. 767–778, 2011. ISSN 00939994.

[45] Zhang, P., Sizov, G., Ionel, D. and Demerdash, N.: Establishing the Relative Merits of Interior and Spoke-Type Permanent Magnet Machines with Ferrite or NdFeB Through Systematic Design Optimization. *IEEE Transactions on*

Industry Applications, vol. 9994, no. c, pp. 1–1, 2015. ISSN 0093-9994. Available at: `http://ieeexplore.ieee.org/lpdocs/epic03/wrapper.htm?arnumber=7017567`

[46] Lotov, A., Bushenkov, V.A. and Kamenev, G.K.: *Interactive decision maps: Approximation and visualization of Pareto frontier*, vol. 89. Springer Science & Business Media, 2013.

[47] C.J.J. Labuschagne, Prof. M.J. Kamper, A.E. and Britz, J.: Eddy current yaw damper. *South African Universities Power and Energy Conference*, 2017.